Summary

Huge parts of the world's oceans remain unexplored, and better knowledge about the state of the oceans is essential when making decisions related to the possibly harmful influence of human activities. Still, the harsh environment, huge size, and inaccessibility of the ocean make exploration difficult. Recently, robotic vehicles have become less expensive and more available and facilitate adaptive exploration of the oceans. However, the difficulty of getting a sufficient number of observations (samples) of such a large domain is still hampering effective deployments, and to improve efforts, the selection of informative sampling sites becomes crucial. In this thesis, we address the problem of how to optimally perform sampling using autonomous underwater vehicles (AUVs) in a dynamic and communication-constrained environment. The motivating application of this study is that of environmental monitoring of concentrations of particles, say, from a mining release site.

By combining underwater robotic sampling with ocean models, informative sampling sites can be selected, and the robot's path can be changed adaptively based on in situ measurements to optimally map the tailings distribution near a seafill. This thesis presents a stochastic spatio-temporal proxy model of dispersal dynamics that can be used for adaptive sampling with an autonomous underwater vehicle (AUV). The proxy model is built using training data from complex numerical ocean and particle transport models and consists of a spatio-temporal Gaussian process model based on an advection-diffusion stochastic partial differential equation. Two sampling strategies are presented, aiming to choose informative sampling sites based on the proxy model; an objective function favoring areas with high uncertainty and high expected tailings concentrations and a strategy aiming to detect the boundaries of excursion sets of high tailings concentrations. Most focus is on adaptive sampling using a single AUV. However, a strategy for multiple is also presented where weighted Voronoi partitions are used repeatedly to divide the survey area into regions to distribute the sampling-workload evenly between the vehicles. The sampling methods are tested through extensive simulation studies, and in actual conditions, in the fjord Frænfjorden where a seafill has been active for several years.

Preface

This thesis is submitted in partial fulfillment of the requirements for the degree of Philosophiae doctor (Ph.D.) at the Norwegian University of Science and Technology (NTNU). The presented work is the result of the doctoral studies carried out at the Department of Engineering Cybernetics (ITK), NTNU. The Ph.D. project was financed by the Norwegian Research Council (NRC) through the Centres of Excellence funding scheme and AMOS (Autonomous Marine Operations and Systems) program, grant numbers 267793 and 223254. My main supervisor has been Professor Tor Arne Johansen, with support from Professor Jo Eidsvik and Associate Professor Morten Omholt Alver.

Acknowledgements

I have met so many clever and interesting people during the last five years. First, I would like to thank my main supervisor Tor Arne. Thank you for giving me the opportunity to pursue a Ph.D., for always answering my emails, and for providing helpful feedback. Thank you, Jo and Morten, for being my co-supervisors, exciting discussions, and for always being interested in my work.

The field experiments in this thesis would have been impossible without the effort of others. Tore Mo-Bjørkelund, your help with implementation before and during AUV deployments has been invaluable. Also, a big thank you to my colleagues in the INDORSE project, Frédéric Py, Emlyn Davies, and Esten Ingar Grøtli, for providing help with the implementation and organizing of the experiments. Also, thanks to Finn Are Michelsen and Tor Nordam for providing ocean model data that has been essential for the work of this thesis. And, thank you, Karine Foss, for interesting discussions and cooperation.

On my first day at ITK, I found you in my office, Inger. I could not have asked for a better office mate. Thank you for being there and for sharing laughter, tears, anger, and joy. I know we will keep sharing.

The social environment in the office has meant the world to me. Thank you, Glenn, Håkon, Erik, Øystein, Marianna, and everybody else (you know who you are). Thanks for all the coffee breaks, the practical jokes, activity Thursdays, chess matches, and knitting meetups. It is what has kept me reasonably sane throughout this period.

The greatest thank you to my family. Gry, thanks for always opening your house, never saying no and always caring. Mamma and pappa, without you, I

surely would not be here. Thank you for always believing in me and for so many times putting me first.

Ole, thank you for reminding me of what really is important in life. I am extremely happy you sent the second message.

Contents

Chapter 1

Introduction

> The oceans make up around 70% of planet Earth, yet over 80% of the world's ocean remains unexplored.
>
> *NOAA - How much of the ocean have we explored? [56]*

Huge parts of the world's oceans remain unexplored. Better knowledge and understanding through exploration are essential to effectively manage, conserve, regulate, and use the oceans' resources. But the harsh environment and the inaccessibility of the sea make exploration difficult. Traditional sampling methods typically include sensors mounted on ships or buoys, but they are expensive and offer little flexibility. Recently, robotic vehicles have become less costly and more available and facilitate adaptive exploration of the oceans. However, the difficulty of getting sufficient observations (samples) of such a large domain is still present, and the selection of informative sampling sites becomes crucial. This thesis addresses the problem of how to optimally perform sampling in the ocean using autonomous underwater vehicles (AUVs).

In this chapter, the motivation and background for the thesis are introduced. An overview of the methodology and the research questions are presented, and the scope and contribution of the thesis are given.

1.1 Ocean Observation: History and Challenges

Human interest in the ocean goes way back, and as early as 4000 BC, Polynesian navigators traded over long distances in the Pacific [72]. In earlier times, observations of the ocean were characterized by systematic collection of data of winds, currents, waves, temperature, and other phenomena from the deck of sailing ships [76]. The first scientific expedition to explore the world's oceans and the seafloor was the Challenger Expedition (1872-1876). The expedition covered more than 100,000 km on the warship HMS Challenger, collecting surface and sub-surface observations, and among many other discoveries, they cataloged over 4,000 previ-

ously unknown species [67]. Since the Challenger expedition, numerous expeditions have collected data from the ocean. Some known examples are the *Fram* expedition in the Arctic ocean [53] and the NORPAC cruises in 1955, where scientists from Japan, Canada, and the United States combined their facilities and utilized more than twenty oceanographic vessels to explore the North Pacific Ocean [57]. In the early 1970s, floating and fixed buoys were introduced as a tool for ocean observation [51]. In 1978 NASA launched the first oceanographic satellite (Seasat), measuring sea-surface winds and temperatures, wave heights, atmospheric liquid water content, sea ice features, and ocean topography [9]. This resulted in an increased number of observations, with satellite data giving a high resolution in the spatial domain at the surface (but at a limited temporal scale) and buoy data showing high resolution on a temporal scale, but only at selected spatial locations. Even with numerous expeditions, and data from buoys and satellites, getting sufficient observations of the oceans is difficult. Lately, robotic platforms have become available and are used for ocean observation. Exploiting robotic platforms and especially AUVs can intensify ocean sampling, giving more data and better insight. Ocean processes are highly nonlinear and non-stationary. The current state of ocean observation is that the number of measurements we can collect is insufficient to describe the ocean well enough. "Lack of sufficient samples is the largest source of error in our understanding of the ocean" [76].

Today, multiple platforms can be used for ocean observation, and Figure 1.1 shows an observational pyramid for ocean observation. The sensors on the top of the pyramid (satellites) typically measure on a large time scale; they give few details on small-scale properties but are suitable for obtaining an overview and observing large-scale changes. Information from these platforms can be used by platforms further down in the pyramid, such as surface vessels, AUVs, and fixed platforms, to decide which area small-scale observation should focus on. Utilizing all possible platforms, from satellites on the top to AUVs, ROVs, and fixed platforms on the bottom will lead to a better understanding of the ocean.

Some important challenges related to the current state of ocean observation are listed below:

- **Complex interactions:** Ocean processes are complex, nonlinear, and highly dependent on time and space. This is due to the ocean's turbulent, heterogeneous, and episodic nature. Understanding and quantifying this influence is complex. An observation taken in one location at the current time might not be valid 10 minutes later, making it hard to have up-to-date knowledge.
- **Sparsely distributed data:** Getting a sufficient number of observations of the ocean is not possible, resulting in sparsely distributed observations.
- **Uncertain sensor observations:** Observations are taken using sensors that all have uncertainties related to the measured quantity. In addition, the sensors themselves might affect the environment resulting in misleading observations.
- **Harsh environment:** The ocean environment is harsh and puts requirements on the equipment used for observing. Pressure, corrosion, and biofouling might all affect, prompting a need for solid and robust equipment,

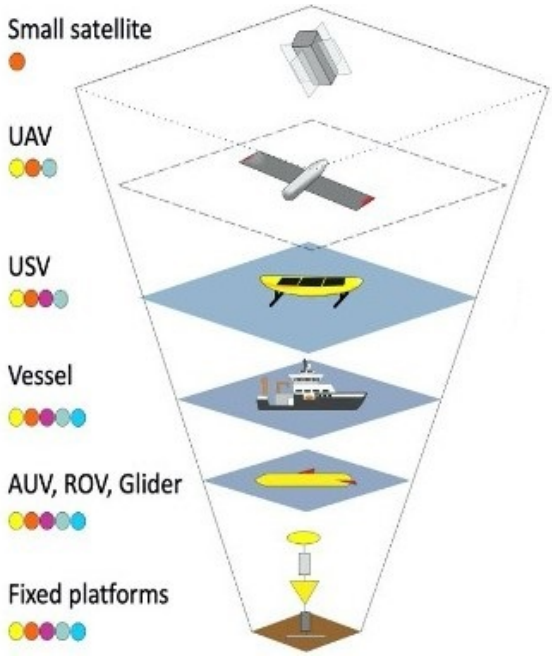

Figure 1.1: Observational Pyramid for ocean observation. The figure shows the hierarchy for observation of the ocean ranging from satellites on top (giving large-scale observations) to AUVs and fixed platforms on the bottom, giving more detailed observations in smaller areas. Figure borrowed from Tor Arne Johansen and Kanna Rajan.

which often makes the equipment expensive. The harsh environment also affects field experiments, as currents, large waves, and strong winds make it harder to install the equipment (and sometimes even impossible to install).

- **Underwater communication:** Underwater communication is complicated due to factors such as multi-path propagation, time variations of the channel, small available bandwidth, and strong signal attenuation, especially over long ranges. Compared to communication above the sea, underwater communication has low data rates because it uses acoustic waves instead of electromagnetic waves.

1.2 Autonomous Underwater Vehicles

This thesis focuses on using AUVs for ocean observation. The first AUV was called SPURV (Self Propelled Underwater Research Vehicle) and was brought to the scene in 1957 [82]. Since then, there has been a rapid development regarding AUVs with the development of new technology. Today, AUVs are used in many applications, e.g. offshore oil and gas [55], military applications [44] and for ocean exploration [76]. An AUV is a free-swimming craft under the control of an onboard computer

and can carry multiple payloads. Some standard sensors are; CTD (measuring conductivity, temperature, and pressure), fluorometers, turbidity sensors, turbulence sensors, and magnetometers. Types of AUVs differ in size, from lightweight AUVs to larger vehicles longer than 10 meters. Smaller vehicles make the logistics easy with a more straightforward launch and recovery and can typically operate for several hours. Larger AUVs have an advantage in sensor payload capacity and endurance and can often run for several days. When AUVs are used for ocean exploration, some typical operations are; mapping of bathymetry as in [28], water-column surveys as in [20], or even under-ice operations as in [49].

When AUVs are submerged, communication and navigation are limited due to the attenuation of radio waves. Radio navigation, e.g., GNSS signals, can only be used when the vehicles are at the surface. The location of a submerged AUV can be decided by either using acoustic communication (finding the relative position to subsea transponders or surface vessels) or based on dead-reckoning techniques, which estimates the current position based on previously known GPS positions (at the surface) and estimates of the AUV's movement. Dead-reckoning utilizes sensors such as IMU (inertial measurement units), providing measures of the acceleration and rotation, and Doppler Velocity Logs (DVLs), which give the speed relative to the seabed. In general, localization of AUVs is prone to errors making navigation uncertain. Hence, surfacing is often implemented as part of the AUV mission to avoid too large errors in the AUV position. A typical AUV mission has a preplanned path consisting of reference points which we call waypoints. Waypoints are locations specified by their latitude, longitude, and depth, and the AUV moves in a straight line between these waypoints. AUVs also can run adaptive missions in which waypoints are selected on-the-fly.

Some pros and cons of using AUVs for ocean observation are listed below in Table 1.1.

Table 1.1: Pros and cons of using AUVs for ocean exploration. Modified from [21].

Pros:	**Cons:**
• Small environmental footprint, low level of intrusion. • Able to travel in difficult, harsh, and remote areas. • Independent of ships (and people). • Modular payload capacity. • Autonomous with the ability to run adaptive missions.	• Limited navigation quality when submerged. • Limited power supply leading to limited operation duration. • Limited underwater communication. • Limited possibilities for launch and recovery during harsh weather. • Risk of losing vehicle (and data) during operations.

Figure 1.2: The robotic vehicle (L-AUV Harald) from OceanScan used in this thesis during the field tests in the Frænfjorden area. The length of the AUV is 240 cm, and it is equipped with multiple sensors like CTD, Dissolved Oxygen, and Fluorometer.

1.3 Adaptive Sampling

Ocean *sampling* can be seen as the action of sensing or measuring one or more physical properties in the ocean at a specific point in space and time. As discussed in section 1.1, getting a sufficient number of ocean samples is hard. To be able to collect the most informative observations effectively, an important question to ask is: *Where and when should we sample?*

This problem of selecting informative sampling locations is often referred to as experimental design (or sampling design) [38]. In sampling design, a model is used to represent the domain, and informative sampling sites are selected based on an optimization criterion. Many informative sampling methods build on the work found in [27, 37] which consider the problem of choosing positions for sensor placement using Gaussian Processes (GPs) [12] to model the environment. Other early works of adaptive sampling can be found in [29, 83].

The models used for selecting sampling sites should include as much information and knowledge about the environment as possible and use this as a basis for path planning. In oceanography, building such models is challenging because of the oceans' large-scale nonlinear processes and high spatio-temporal variability. Existing models using numerical methods continuously improve their accuracy [23, 26], but they still have errors due to simplifications, limitations in numerical implementation, and uncertain parameters, initial and boundary conditions. Hence, adaptive approaches that utilize prior information and incorporate knowledge from observed data are beneficial. Such methods, which execute path planning online during a mission, using information from real-time in-situ measurements, are called *adaptive sampling* methods. Building on the work by [27, 37], [42] explored

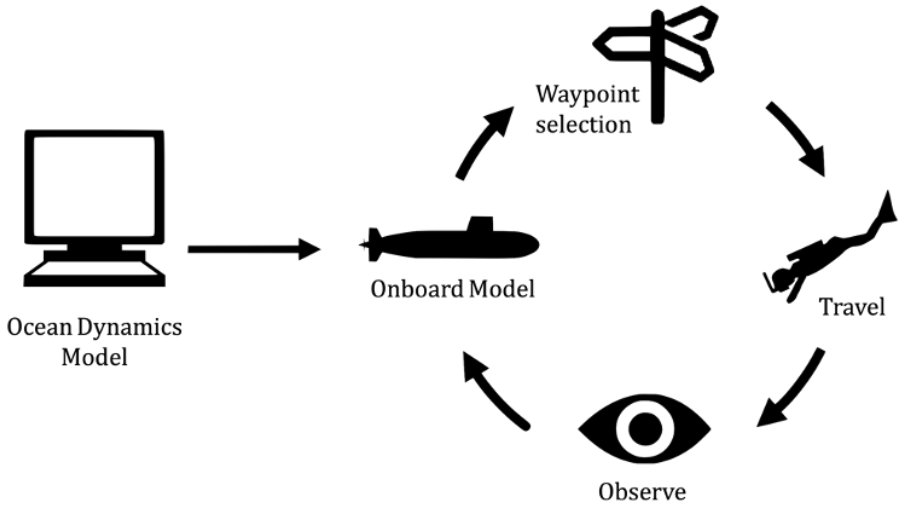

Figure 1.3: An overview of the adaptive sampling method. Data from ocean dynamics models are used to create an onboard surrogate model able to run on an AUV. Based on the current state given by the onboard model, waypoints are selected based on design choice criteria. The AUV then travels to the waypoint and collects measurements (observations). The observations are used to update the onboard model.

adaptive methods using multiple robots and incorporating new data using dynamic programming.

This thesis will describe concepts used in adaptive sampling for water-column ocean observation. Figure 1.3 gives an overview of the adaptive approach used in the thesis. The steps of the approach are listed in the textbox below:

Adaptive sampling method

1. A **model** of the environment is constructed using prior knowledge. The model includes prior knowledge from ocean models and is able to run onboard the AUV.
2. Path planning is executed using the onboard model, and a new **waypoint is selected** leading the AUV to informative sampling locations.
3. The AUV **travels** to the selected waypoint.
4. **Observations**(samples) are taken using sensors onboard the AUV.
5. The onboard model is **updated** incorporating newly observed data in the onboard model.
6. Step 2-5 is repeated until the mission is ended.

The benefits of adaptive sampling will depend on the situation. There are nu-

merous studies on the value of additional (sequential) sampling efforts in different contexts, say clinical trials in medical research [32] or geoscience data [17]. In our case, there would be limited to gain by adaptation if a priori information makes it possible to pre-script a high-value AUV plan before deployment. However, if there is high prior variability, the ability to adapt the initial plan one way or the other, based on onboard measurements, would bring added value by guiding the AUV to more relevant places.

1.4 Field Experiments: The Frænfjorden Area

Human population, industrial activities, and energy consumption continue to grow, which has a massive impact on nature and the environment [2]. Environmental monitoring refers to the tools and techniques designed to observe an environment, characterize its quality, and establish ecological parameters to accurately quantify an activity's impact on an environment [41]. This is important to manage and minimize the effects of human activities on the environment.

For organizations, this might be to ensure compliance with regulations or laws or to mitigate risks of harmful effects on the natural environment and protect the health of human beings. The primary motivation for this thesis is environmental monitoring of particles spreading near a seafill with the Frænfjorden area in mind. The field experiments in this thesis are all conducted in the inner parts of the fjord Frænfjorden in Elnesvågen. On the shore of this fjord, the factory Omya Hustadmarmor is located. The factory can be seen in Figure 1.5 and the location of the fjord is seen in the map in Figure 1.4. In this factory, a calcium carbonate processing plant has been operating for several decades. This processing of ore from mining causes fine-ground waste called tailings [39], which must be disposed of. The tailings are disposed of on the ocean floor, in a seafill close to the factory.

In Norway, there are several active and planned seafills, and they all have implications for the marine environment [50, 65]. The tailings typically consist of particulates and residual chemicals from processing, and this waste will smother the sea bed close to the sea fill. In addition, some of the waste may be transported by ocean currents away from the outlet, thus affecting a larger area of the sea bed and the water column. There is still a lack of knowledge about the transportation process of the waste. Models used to determine the transportation suffer from uncertainties due to errors in input data and weaknesses in the model formulation and configuration. Hence, development of enabling technology that performs efficient and targeted ocean sampling is needed. In addition to such hindcast model validation and correction, the information can be used in real-time to improve the ocean and particle transport models using data assimilation.

The outlets in Frænfjorden are located at approximately 20 m depth, and tailings are continuously discharged with a time-varying discharge rate. The discharge alters between two pipes, which we refer to as the eastern and the western pipe. Figure 1.4 shows the location of these pipes.

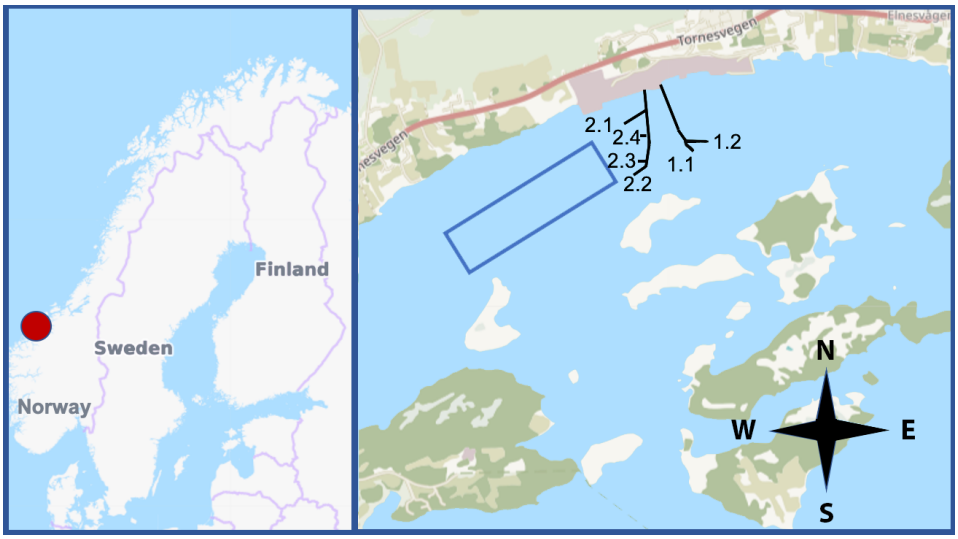

Figure 1.4: The location of Frænfjorden and the factory Omya Hustadmarmor AS. The black lines represent the pipes where mine tailings are let out, and the numbers represent possible outlets. The factory is marked in pink in the figure.

Figure 1.5: The factory Omya Hustadmarmor AS on the shore of Frænfjorden in Elnesvågen. Here a calcium carbonate processing plant has been in operation for several decades. Mine tailings from the factory are deposited on the seafloor in the inner parts of Frænfjorden.

1.5 Research Questions

The main focus of this thesis is the development of adaptive sampling methods using AUVs. The primary focus is on coastal waters, intending to estimate a dy-

namic field. In this thesis, the focus is on 2D models, but the methods can easily be applied to 3D models as well. The motivating application of this study is that of environmental monitoring of concentrations of particles from a mining release site such as Frænfjorden (see Section 1.4). With the described application in mind, the thesis aims to answer the following questions:

Research Questions

- **How can we create an ocean dynamics model that is computationally efficient, easy to update, and able to run onboard an AUV?**
  The goal of the environmental monitoring is to obtain a good field estimate of the spreading of particles. The model needs to be computationally efficient, giving a good estimate of the environmental status at all times and being able to incorporate new information from AUV observations in real-time.

- **How can prior information be utilized?**
  To perform optimal choices, all prior knowledge (e.g., from ocean models or expert knowledge) should be included in the decision-making. How can this information be incorporated into the onboard models? What kind of information should be included? And how can this information be utilized in the best possible way?

- **What is the optimal way of taking samples using one or multiple AUVs?**
  When the goal is obtaining the best possible field estimate, where and when should samples be taken? What sites are most informative? How can this be described mathematically and translated to AUV behavior?

This thesis contains theoretical analysis, simulation studies, and field experiments that will all be used to give answers to the above questions.

1.6 Publications and Contributions

The main contributions of this thesis are related to the development and analysis of adaptive sampling methods using AUVs in the coastal ocean, including validation and testing of the methods in the field. The thesis is based on papers published (or submitted) in peer-review international journals and conferences. The main contributions are summed up below:

Main contributions

- **Spatio-temporal GP model:** The thesis suggests a surrogate spatio-temporal model describing ocean dynamics. The model can incorporate prior information from ocean models, such as predictions of ocean currents and particle concentrations. It uses Gaussian processes and can implement knowledge from in-situ observation in real-time. The spatio-temporal model is presented in part I of the thesis.
- **Objective function for waypoint selection:** An objective function for waypoint selection during adaptive sampling is suggested. The objective function aims to balance the exploration/exploitation when sampling. On the one side, the objective function focuses on areas with elevated model variance; on the other side, it focuses on areas with high concentrations (e.g., detecting hotspots). The objective function is described in Chapter 6.
- **Voronoi strategy for adaptive sampling using multiple vehicles:** The thesis discusses using multiple vehicles for adaptive sampling. An approach is suggested using weighted Voronoi partitions to divide the sampling area into suitable areas for each AUV. The method is presented in Chapter 8.
- **Simulation studies:** All methods described in the thesis are tested through extensive simulation studies. The simulation studies give essential insights into the sampling methods, showing pros and cons, and are helpful for further development. Simulation studies are presented in part II of the thesis.
- **Field experiments:** As a proof-of-concept, several field experiments have been executed during the thesis work. Results from the field studies are presented in part III of the thesis.

This thesis is based on the following list of papers published in peer-review international journals and conferences:

- **Paper A:** G.E. Berget, T.O. Fossum, T.A. Johansen, J. Eidsvik, K. Rajan. Adaptive Sampling of Ocean Processes Using an AUV with a Gaussian Proxy Model. *11th IFAC conference on control applications in marine systems, robotics and vehicles (CAMS)*, 2018. [4]

  Contribution: The paper introduces the stochastic spatial onboard model used in this thesis which is presented in Chapter 3. Data from numerical ocean models (the ocean models are presented in Chapter 2) are used to build a prior belief for the onboard model. The paper also introduces an objective function for waypoint selection and path planning. Details on the proposed objective function are presented in Chapter 6.

- **Paper B:** G. E. Berget, J. Eidsvik, M. Alver, F. Py, E. I. Grøtli, and T. A. Johansen. Adaptive underwater robotic sampling of dispersal dynamics in

the coastal ocean. *The 19th International Symposium on Robotics Research (ISRR)*, 2019. [5]

Contribution: In this paper, the spatial model from [4] is tested onboard an AUV during field experiments in Frænfjorden. The paper presents results from these field trials and adds details on the robotic platform, the embedded system, and the implementation. Chapter 10 presents results from the field experiments and includes the field trials presented in this paper.

- **Paper C:** G.E. Berget, J.Eidsvik, M.O. Alver, T.A. Johansen. Dynamic Stochastic Modeling for Adaptive Sampling of Environmental Variables Using an AUV. *Autonomous Robots*. 2022 (conditionally accepted)

  Contribution: Experiences from the two previous papers showed the need for a temporal model. This paper introduces a stochastic spatio-temporal model that can be used for waypoint selection. The model details are presented in Chapter 4. In the paper, a simulation study compares the proposed adaptive sampling method to simpler strategies (one of them being the sampling method proposed in [4]).

- **Paper D:** K.H. Foss, G.E. Berget, J. Eidsvik. Using an autonomous underwater vehicle with onboard stochastic advection-diffusion models to map excursion sets of environmental variables. *Environmetrics.*, Volume 33, Issue 1, February, paper e2702, 2022. [18]

  Contribution: In this paper, a similar spatio-temporal model as in is used, but with another goal and focus. The goal is to monitor the excursion set (ES) of high concentrations. Closed-form expressions for the expected misclassification probabilities of the ES enable real-time operation on board the autonomous vehicle, and this is used to guide the spatio-temporal sampling. Simulation studies show that the suggested strategies outperform other approaches that either (i) simplify the models for spatio-temporal variation or (ii) simplify the design criterion. A field test shows how autonomous underwater sampling helps refine an initial stochastic advection-diffusion model. These experiments further show that the vehicle can adapt to focus on regions with intermediate concentrations where it is natural to improve the ES prediction.

- **Paper E:** G.E. Berget, J.Eidsvik, M.O. Alver, T.A. Johansen. Multi-Robot Adaptive Sampling for Dynamic Field Estimation in Communication-Constrained Environments. 2022 *IEEE Journal of Oceanic Engineering*. (submitted)

  Contribution: In this paper multiple AUVs are introduced (see Chapter 8. A multi-robot adaptive sampling method is suggested for use in communication-

constrained environments such as the ocean. Weighted Voronoi partitions are used repeatedly to divide the survey area into regions with the aim of distributing the sampling-workload evenly between the vehicles. In each partition, adaptive sampling is performed using the spatio-temporal Gaussian Process model from previous work running onboard the vehicles to represent the field to be estimated. Data is shared when vehicles are within communication range to obtain an improved field estimate. Simulation studies are conducted, estimating both a static and dynamic field. The results show that repartitioning of the sampling regions during a mission improves mission efficiency compared to methods that use static regions throughout the full mission.

1.7 Outline

The thesis is divided into four parts. The first part describes the surrogate (onboard) model used for the adaptive sampling. The second part digs into the adaptive sampling method, which utilizes the model described in the first part. In the third part, results from the field experiments in Frænfjorden are shown, and details on the implementation on the robotic platform are given. The third and final part concludes and discusses future research directions.

Part I: Modeling

The first part consists of three chapters and describes the details of the onboard model. Chapter 2 introduces the numerical ocean models used to build the onboard model. Chapter 3 discusses the GP spatial model used in the thesis and introduces field estimation and excursion sets. The last chapter of this part (Chapter 4) explains the temporal part of the model so that we, in the end, have a spatio-temporal onboard model describing the ocean dynamics.

Part II: Adaptive Sampling

The second part explains more details on the adaptive sampling methods in this thesis. Chapter 6 gives details about waypoint selection and describes the objective function used to select informative sampling sites. Chapter 7 considers another criterion for adaptive sampling, optimizing waypoints for finding excursion sets. Lastly, adaptive sampling for multiple AUVs is considered in Chapter 8.

Part III: Field Experiments

Field experiments in Frænfjorden are presented in part III. More details on the robotic platform and the implementation of the methods are given in Chapter 9, and results from three field trials are described in Chapter 10.

Part IV: Conclusion

Finally, Chapter 11 sums up the work in the thesis, concludes, and describes future research directions.

Part I

Modeling

Chapter 2

Ocean Modeling

All models are wrong.

George Box

The famous statistician George Box said in 1976: "All models are wrong." He later modified this statement and added, "but some are useful" [10]. This quote fits well concerning the models used in this thesis, where data from numerical oceanographic models are used to build a prior belief of the state of the ocean before deploying the AUV. This chapter briefly introduces ocean modeling and explains why ocean models are insufficient to accurately describe the ocean dynamics, hence prompting the need for ocean observations. The chapter also presents the two numerical models SINMOD (ocean dynamics model) and DREAM (particle transportation model), used to describe the dynamics in the Frænfjorden area.

2.1 Introduction to Ocean Modeling

Ocean models describe the state of the ocean at a given time, providing information on temperature, salinity, currents, density, and pressure. The models are based on a set of thermodynamic and hydrodynamic equations, commonly called the primitive equations, and these are solved using numerical techniques. Running these models is a computer-intensive task since it involves solving a large set of equations. Thus, we get a trade-off between the resolution of the model and the available computer resources. Because of these limitations, a high-resolution model can only be computed for small areas. A common technique is nesting, where the model is run at a large scale producing boundary conditions for smaller scale models with higher resolution.

Input to ocean models typically includes tides, sea-level pressure, wind, heat exchange, bathymetry, precipitation and freshwater runoff. Errors in these input data and weaknesses in the model formulation and configuration can affect the output data quality. Due to nonlinear ocean dynamics, such deviations can propagate to more significant deviations in model predictions compared to actual conditions. This might lead to predictions of eddies at the wrong location or time even though

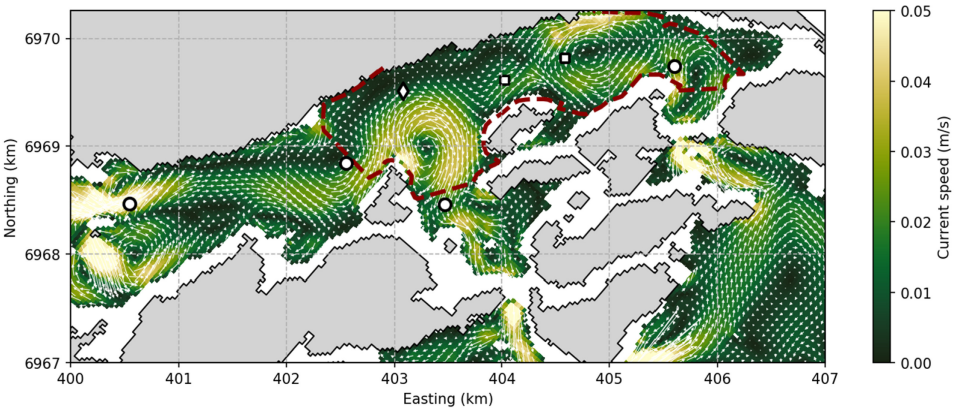

Figure 2.1: Monthly mean current for November 2013, at 20 m depth. The dashed red line shows the area of the seafill, while the white squares indicate possible discharge points. The white arrows show the current direction, and the color represents the current speed. Figure from [54].

the overall eddy activity may fit well with actual conditions. Therefore, for applications of ocean models that require close correspondence between model estimates and actual conditions at the simulated time and area, additional data from observations are beneficial (e.g., through sampling with AUVs).

2.2 SINMOD - Ocean dynamics model

SINMOD is a numerical ocean model system that connects and simulates physical and biological processes in the ocean [74]. The model has been developed at SINTEF since 1987 and has been applied to large portions of the Norwegian coast, including fjords, the Norwegian Sea, and the Barents Sea. The model is based on the Navier-Stokes equations [77] and uses a nesting technique where high resolution models obtain their boundary conditions from larger model domains with lower resolution. SINMOD is established in configurations with horizontal resolutions ranging from 20 km to 32 m, and the model setup for 32 m horizontal resolution use boundary conditions provided by a 160 m resolution. The 160 m setup, in turn, uses boundary conditions from an 800 m setup, which is nested in a 4 km setup, and finally is nested in a 20 km setup. Input to the model includes atmospheric forcing, freshwater runoff, and boundary conditions (temperature, salinity ,surface elevation, currents).

Figure 2.1 is an example output from the SINMOD model, showing the monthly mean current for November 2013 in the Frænfjorden area at 20 meters depth. The figure is from [54].

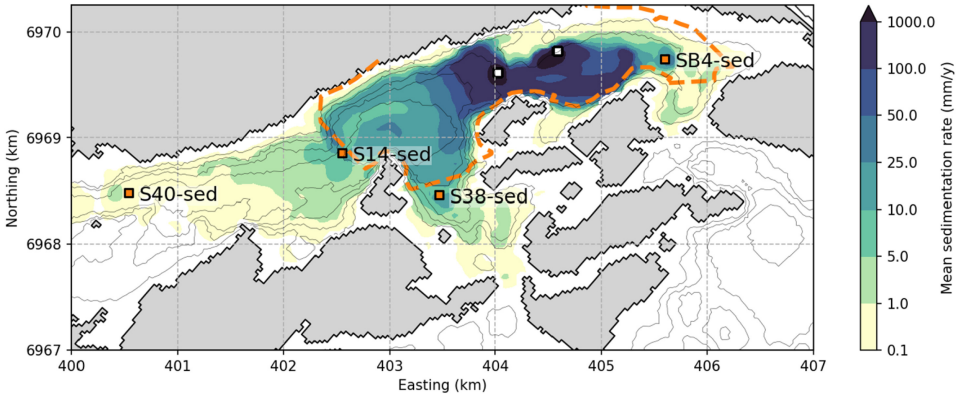

Figure 2.2: Mean sedimentation rate calculated from a six-month simulated discharge period (June–November 2013). The dashed red line shows the area of the seafill, and the white squares indicate the discharge points. Figure taken from [54].

2.3 DREAM - Particle transportation model

DREAM is a Lagrangian particle transport model [62] which can be used to simulate the behavior and fate of marine pollutants, including particulate discharges from drilling operations [69, 70]. It provides time series of concentrations of released materials in the water column and deposition of these materials onto the sea floor. Input to the DREAM model includes hydrodynamic data delivered by SINMOD and information about the release (amount, rate, densities, grain size distribution). DREAM is often used as a decision support tool for managing operational discharges to the marine environment.

Example output from the DREAM model from the Frænfjorden area can be seen in Figure 2.2. The figure shows the mean sedimentation rate calculated from a six-month simulated discharge period from June - November 2013. In this period, two discharges were in operation, shown as white squares in the figure. The figure is taken from [54].

2.4 Frænfjorden setup

In this thesis, SINMOD and DREAM have been used to represent the Frænfjorden area. A detailed data set from April 2013 is used for all the simulation studies. SINMOD uses various input data. The bathymetry data is based on DBM Sør-Norge, supplemented by OLEX data recorded by SINTEF Materials and Chemistry. The atmospheric input data is produced using the Weather Research and Forecasting (WRF) (`https://www.mmm.ucar.edu/weather-research-and-forecasting-model`) model simulated with boundary values from the ERA - Interim reanalysis [15], and climatological data for freshwater runoff is used. Ocean dynamics data from SINMOD are provided in NetCDF format for input to the DREAM model for particle spreading. These data files cover the necessary area for the DREAM model with a sampling time of 20 minutes for current and wind. In addition, information

about the release regarding the amount, size, and detailed location is provided by the factory Hustadmarmor AS. A detailed description of the model setup can be found in [54].

For this thesis's work, three datasets from the same models (SINMOD and DREAM) have been used. Information about these data sets can be seen in Table 2.1. This thesis uses the dataset from April 2013 for all simulation studies. In addition, model runnings were done before and during all field expeditions.

Table 2.1: Overview of the different datasets used in this thesis. All datasets are made using the particle transportation model (DREAM) and the ocean current model (SINMOD). The resolution shows both the horizontal resolution and the time resolution. The usage describes what the datasets have been used for in the work of this thesis.

Time Period	DREAM resolution	SINMOD resolution	Usage
April 1st - April 30th (2013)	16 m | 20 min	32 m | 20 min	All simulation studies
October 16th - 19th (2018)	32 m | 20 min	32 m | 20 min	Fieldwork October 2018
December 17th and 18th (2020)	32 m |20 min	32 m | 20 min	Fieldwork December 2020

2.5 Ocean models as prior information

A prerequisite for effective mission adaptation is accurate information about the spatial and temporal conditions. The models described earlier in this chapter give a good picture of the ocean's status at a given time. Unfortunately, this model requires a lot of computer power and storage and cannot run in real-time onboard an AUV. Instead, data from SINMOD and DREAM is used to build a surrogate or emulator model which can be run onboard the AUV [25]. The onboard model will be described in more detail in Chapters 3 and 4. Figure 2.3 shows the relation between the onboard model, DREAM, and SINMOD. Ocean dynamics data from SINMOD is used as input to DREAM, particle concentration data from DREAM is used as input for the onboard spatial model described in Chapter 3, and current data from SINMOD is used as input to the onboard temporal model described in Chapter 4. The temporal and the spatial model are combined to obtain a full onboard model describing ocean dynamics in both time and space.

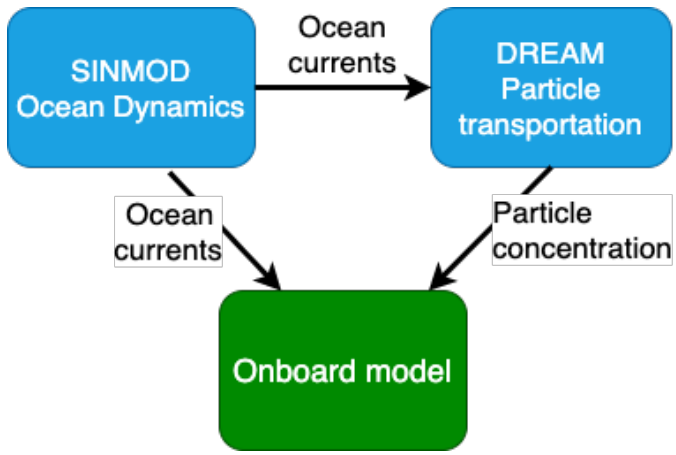

Figure 2.3: The relation between SINMOD, DREAM, and the onboard surrogate model. Ocean dynamics data from SINMOD is used as input to DREAM, particle concentration data from DREAM is used as input for the onboard spatial model described in Chapter 3, and current data from SINMOD is used as input to the onboard temporal model described in Chapter 4.

Chapter 3

Spatial Model

> Everything is related to everything else, but near things are more related than distant things [78]
>
> Waldo Tobler

The quote by Tobler is referred to as the "first law of geography" and is considered the foundation of the fundamental concepts of spatial dependence and spatial autocorrelation. Moreover, imagine; If you are looking for gold, where do you start looking? You likely end up somewhere close to where gold has been previously found because this is where you are most likely to find gold, and it is something humans have learned from experience and intuition. This concept can also be seen in the case of the spreading of particles underwater. We expect to observe more particles near the outlet than further apart. Moreover, if we observe many particles in one area, it is more likely that the neighboring areas also contain high concentrations. In other words, spatial occurrences tend to decay with distance, and we want to integrate this fact into our models for adaptive sampling.

In addition to spatial dependencies, the models need to represent uncertainties. Uncertainty measures are crucial in an adaptive sampling setting because very few parts of the process are 100% correct; The measurements are uncertain due to uncertainties in the sensors and the measurement localization due to AUV navigation limitations. The real-world ocean dynamics may, in principle, be deterministic, but since our information is incomplete at each observation stage, our understanding is affected by uncertainty. Hence, there are two main properties we want the spatial model to be able to represent; Spatial dependencies and uncertainties.

We have stated that a reasonable estimate of the underlying field is essential to perform informative adaptive sampling. So-called field estimation is the estimation of how a particular variable (in our case, the particle concentration in water) varies in space and time, i.e., an estimate of its spatio-temporal distribution based on observed or sampled data. This chapter presents the onboard model's spatial part, which will act as our best guess of the field's status and include measures of uncertainty.

3.1 Why use Gaussian processes?

The numerical high fidelity models presented in Chapter 2 are computationally intensive, and the current versions of AUVs cannot run such models onboard in real-time. Instead, a surrogate or proxy model is commonly used to represent the state of the ocean at all times. This model is often referred to as the *onboard* model in this thesis. In the literature, different types of such models are proposed; [79] suggest using neural networks, and [71] use linear combinations of static basis functions. However, most adaptive sampling methods utilize GPs [12], which are widely used to create non-parametric and computationally efficient models. They are popular not only for adaptive sampling but used in various applications like neuroimaging [31], machine learning [66] and sensor placement [38]. Combining GPs with robotic vehicles is amongst others explored in [84] where an AUV is used to track an upwelling front, and in [13] who use an AUV to collect samples for ex-situ analysis, selecting the sampling locations based on previous missions and maximizing a utility function. [43] explore a method of multiple vehicles using a mixture of GP models. Some reasons for the GPs' popularity (and the reasons why GPs are used in this thesis) are listed below:

- **Efficient computation and updating:** Compared to the numerical models described in Chapter 2, GPs are computationally efficient, and it is easy to update the model belief with new knowledge from observations. Still, the computational time increases as the size of the modeled domain increases.
- **Easy incorporation of prior information:** As we will describe in detail in this chapter, GPs can be fully expressed by their mean and a covariance matrix. Hence, this alleviates model fitting to the first- and second-order moments of the relevant process [14].
- **Represent uncertainties:** GPs can provide measures of predictive uncertainty (e.g., variance or entropy [mutual information] criterion), which can be used to quantify information gain as an uncertainty reduction.

3.2 Notation

In this thesis, we restrict attention to the case of 2D spatial models. However, all theory applies and can easily be expanded to 3D. The random variable describing the quantity of interest is X. It may depend on both time, t, and space, $\boldsymbol{s}$, and is then denoted $X(t, \boldsymbol{s})$. In the general case, the time and spatial variables are continuous, but they are discretized at some point. The spatial component is two-dimensional and given in the Cartesian coordinates east and north. That is, $\boldsymbol{s} = (s_e, s_n)$. If the temporal component is fixed, it may be introduced as a subscript: $X_t(\boldsymbol{s})$, meaning that X_t is a spatial variable. This notation is often used in the discrete time case to emphasize that the time variable may not vary arbitrarily and is, in that sense, fixed. When the spatial component is fixed, $\boldsymbol{s} = \boldsymbol{s}_i$, regular notations, $X(t, \boldsymbol{s}_i)$ or $X_t(\boldsymbol{s}_i)$, are used.

3.3 Gaussian processes

A GP is defined as a collection of random variables with a multivariate normal probability density function (also called multivariate Gaussian probability function). This way, analytical solutions are found easily since all finite subsets of the domain will also follow a multivariate Gaussian distribution. In the application of this thesis, a GP is used to characterize the particle concentration at given points in space, discretized down to a regular 2D grid. We let $\mathcal{D} \subset \mathbb{R}^2$ be some finite 2-dimensional grid, with n_E grid points in eastern direction and n_N grid points in northern direction. Resulting in a total grid size of $n = n_E \times n_N$. The variable of interest is the particle concentration represented by, $X_t(\boldsymbol{s}); \boldsymbol{s} \in \mathcal{D} \subset \mathbb{R}^2$. When this field is modelled by a GP, we have that $\boldsymbol{X}_t = (X_t(\boldsymbol{s}_1), X_t(\boldsymbol{s}_2), \ldots, X_t(\boldsymbol{s}_n))^T$, for any configuration $(\boldsymbol{s}_1, \boldsymbol{s}_2, \ldots, \boldsymbol{s}_n) \in \mathcal{D}$, $i = 1, 2, \ldots, n$ are jointly Gaussian with the density function

$$f_{\boldsymbol{X}_t}(\boldsymbol{x}) = \frac{1}{(2\pi)^{\frac{n}{2}} |\boldsymbol{\Sigma}_t|^{\frac{1}{2}}} \exp\left(-\frac{1}{2}(\boldsymbol{x} - \boldsymbol{\mu}_t)^T \boldsymbol{\Sigma}_t^{-1} (\boldsymbol{x} - \boldsymbol{\mu}_t)\right). \tag{3.1}$$

Hence, the estimated field $\boldsymbol{X}_t$ is fully represented by the mean vector $\boldsymbol{\mu}_t$ of size n and the correlation matrix $\boldsymbol{\Sigma}_t$ of size $n \times n$, giving

$$\boldsymbol{X}_t \sim N_n(\boldsymbol{\mu}_t, \boldsymbol{\Sigma}_t). \tag{3.2}$$

3.4 Initial State

When using GPs in a spatio-temporal setting, the model is updated as new observations are obtained and as time passes. A spatial GP models the initial state estimate. At the beginning of an adaptive sampling mission, we have $t = 0$, and the initial state is given by

$$\boldsymbol{X}_0 = (X_0(\boldsymbol{s}_1), X_0(\boldsymbol{s}_2), \ldots, X_0(\boldsymbol{s}_n))^T, \tag{3.3}$$
$$\boldsymbol{X}_0 \sim N_n(\boldsymbol{\mu}_0, \boldsymbol{\Sigma}_0). \tag{3.4}$$

Hence, the mean $\boldsymbol{\mu_0}$ and the covariance $\boldsymbol{\Sigma}_0$ needs to be determined. The mean $\boldsymbol{\mu_0}$ can be interpreted as the best estimate of the particle concentration at time $t = 0$. In this thesis, prior information from the numerical ocean models presented in Chapter 2 is used to determine the model mean values, which is further explained in chapter 5.

The initial state covariance matrix $\boldsymbol{\Sigma}_0$ describes two important properties of the state: It describes the noise of the system, i.e., the variance of the value in each grid cell. Further, the matrix takes into account the spatial correlation between the variables. As discussed earlier in this chapter, the fundamental concept of modeling spatial correlation needs to fulfill two main properties: i) that correlation decays with distance and ii) that the covariance matrix is positive definite. To achieve this, it is common to use generic functions to define $\boldsymbol{\Sigma_0}$ [66]. In the setting of GPs, we speak of kernels [66] while we in statistics often speak of correlation functions

or variograms. The covariance matrix is given by

$$\boldsymbol{\Sigma_0} = \begin{bmatrix} \Sigma_{11} & \Sigma_{12} & \dots & \Sigma_{1n} \\ \Sigma_{21} & \Sigma_{22} & \dots & \Sigma_{2n} \\ \vdots & \vdots & \ddots & \vdots \\ \Sigma_{n1} & \Sigma_{n2} & \dots & \Sigma_{nn} \end{bmatrix}, \tag{3.5}$$

where $\Sigma_{ij} = \sigma_i \sigma_j R_{ij}$ and R_{ij} is the correlation function. Hence, the diagonal of the covariance matrix contains the variances σ_i^2, and the off-diagonal elements describe the covariance between the locations. It is common to assume isotropic correlation, where the correlation only depends on the Euclidean distance between variables on the grid [17]. Isotropic correlation is used throughout this thesis.

3.5 Updating

Additional information can be added to a GP field estimate through conditioning, and GPs are used in a Bayesian setting. Let us now assume we have a measurement vector of size m at time t represented by the random variable

$$\boldsymbol{Y}_t = \boldsymbol{G}_t \boldsymbol{X}_t + \boldsymbol{\epsilon}_t, \tag{3.6}$$

where $\boldsymbol{G}_t$ is a $m \times n$ matrix specifying the sampling design at time step t. The matrix rows have one-entries on the vector position of the measured values, and the rest is zero. Each measurement error ϵ_t is independent and Gaussian distributed with zero mean and standard deviation given by τ. Hence, we have $\boldsymbol{\epsilon} \sim N(\boldsymbol{0}, \tau^2 \boldsymbol{I}_m)$, where $\boldsymbol{I}_m$ is the $m \times m$ identity matrix. We have that

$$\boldsymbol{Y}_t | \boldsymbol{X}_t \sim N(\boldsymbol{G}_t \boldsymbol{X}_t, \tau^2 \boldsymbol{I}_m). \tag{3.7}$$

Now, assuming that ϵ_t and $\boldsymbol{X}_t$ are independent, and since linear combinations of Gaussian distributed random variables also are Gaussian distributed, we have, This is called the likelihood in the Bayesian framework, but we will refer to it as the data model. We have the following properties for the distribution of $\boldsymbol{Y}_t$

$$E[\boldsymbol{Y}_t] = \boldsymbol{G}_t \boldsymbol{\mu}_t, \tag{3.8}$$

$$\mathrm{Cov}(\boldsymbol{Y}_t) = \tau^2 \boldsymbol{I}_m + \boldsymbol{G}_t \boldsymbol{\Sigma}_t \boldsymbol{G}_t^T. \tag{3.9}$$

The next step is to update or model for the whole system when measured values are added. Hence, we need the distribution of $\boldsymbol{X}_t | \boldsymbol{Y}_t$, which is called the posterior distribution. If we let the realization of $\boldsymbol{Y}_t$ be $\boldsymbol{y}_t$, we have

$$\boldsymbol{X}_t | \boldsymbol{Y}_t \sim N_n(\boldsymbol{\mu}_{t|\boldsymbol{y}_t}, \boldsymbol{\Sigma}_{t|\boldsymbol{y}_t}), \tag{3.10}$$

$$\boldsymbol{\mu}_{t|\boldsymbol{y}_t} = \boldsymbol{\mu}_t + \boldsymbol{\Sigma}_t \boldsymbol{G}_t^T (\tau^2 \boldsymbol{I}_m + \boldsymbol{G}_t \boldsymbol{\Sigma}_t \boldsymbol{G}_t^T)^{-1} (\boldsymbol{y}_t - \boldsymbol{G}_t \boldsymbol{\mu}_t), \tag{3.11}$$

$$\boldsymbol{\Sigma}_{t|\boldsymbol{y}_t} = \boldsymbol{\Sigma}_t - \boldsymbol{\Sigma}_t \boldsymbol{G}_t^T (\tau^2 \boldsymbol{I}_m + \boldsymbol{G}_t \boldsymbol{\Sigma}_t \boldsymbol{G}_t^T)^{-1} \boldsymbol{G}_t \boldsymbol{\Sigma}_t^T. \tag{3.12}$$

3.5.1 Example: GP update

In this section, a short example illustrating GP updating is given. The prior state is shown in figures 3.1a and 3.1b. A measurement of the value 9 with uncertainty $\tau = 0.5$ in the gird cell (20,6) is then used to update the GP. The posterior result can be seen in figures 3.1c and 3.1d. The example shows that the state mean at the measured grid cell increases and becomes quite close to the measured value. Due to the selected kernel, the update also affects the neighboring grid cells. The same tendency is seen in the updating of the variance.

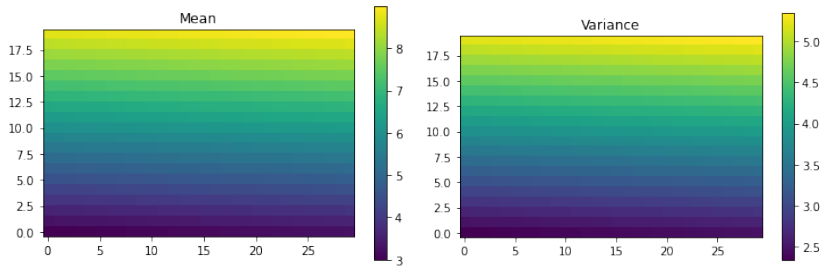

(a) Prior mean

(b) Prior variance

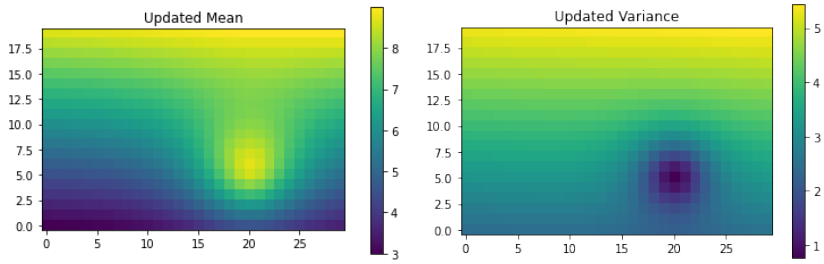

(c) Posterior mean

(d) Posterior variance

Figure 3.1: The figure shows one GP update. The prior state is shown in figures 3.1a and 3.1b. A measurement of the value 9 in the grid cell (20,6) is then used to update GP. The posterior result can be seen in figures 3.1c and 3.1d.

As we see from the figure, the model mean at the sampling location is changed and is now close to the observed value. For the variance, we observe a decrease at the grid cell of the observed value. Because of the kernel, the surrounding grid cells are also affected by the update.

3.6 Excursion Sets and Probabilites

ESs indicate where the variables of interest are above some critical limit. Identifying ESs is essential in several environmental applications [1, 24]. Let l be the critical limit of the variable. A random ES over the domain $\mathcal{D}_s$ at time t is here defined as

$$\mathrm{ES}_t = \{\boldsymbol{s}_i \in \mathcal{D}_s : \boldsymbol{X}_t(\boldsymbol{s}_i) > l\}. \tag{3.13}$$

In this context, t is a particular time of interest, where one, in our case, can take some action to mitigate the concentration level by, for instance, reducing the mining deposition rates. This reference time will typically be the latest monitoring time. Note that expression (3.13) defines just one of several kinds of ESs [7, 8]. Excursion sets are usually represented by zeros and ones. In our case, the random excursion set is represented as an N-sized vector with values given by

$$\mathrm{ES}(\boldsymbol{s}_i) = \begin{cases} 1 & \boldsymbol{X}(\boldsymbol{s}_i) > l, \\ 0 & \text{otherwise.} \end{cases} \tag{3.14}$$

This thesis uses the excursion probability (EP) to define the random ESs. EPs define the probability of the random variable being above the critical limit l. In our case, where the random variable is multivariate Gaussian, the EP at time t is defined as

$$\begin{aligned} \mathrm{EP}_t(\boldsymbol{s}_i) &= P(\boldsymbol{X}_t(\boldsymbol{s}_i) > l) \\ &= 1 - \Phi\left(\frac{l - E[\boldsymbol{X}_t(\boldsymbol{s}_i)]}{\sqrt{\mathrm{Var}(\boldsymbol{X}_t(\boldsymbol{s}_i))}}\right) \end{aligned} \tag{3.15}$$

where $\Phi(\dot{})$ is the Gaussian cumulative distribution function. The ESs are then predicted by using a cut off value $EP_{cut} = 0.5$.

3.6.1 Example: Excursion sets

We now show a simple example to illustrate the use of excursion sets. Figure 3.2 shows excursion sets for different values of the critical limit l given the Gaussian field in figure 3.2a. The yellow color represents the excursion sets. As seen from the figures, a greater value of l leads to smaller excursion sets, as there are fewer grid cells with values exceeding the critical limit.

3.7 Limitations and considerations

Some assumptions need to be taken when using GPs to create an onboard ocean model. The kernel used for spatial dependencies assumes an isotropic relationship; it is assumed that the correlation does not depend on direction. However, ocean dynamics are turbulent, and the direction of currents due to episodic events such as tides and due to the bathymetry, makes ocean dynamics both non-isotropic and non-stationary in real-life. Even though GPs are computationally efficient for the purpose used in this thesis, having even larger data sets would give rise to problems. The computational demand of the updating equations is $O(n^2)$ or $O(m^3)$, but since we here operate with $m << n$ the term $O(n^2)$ will dominate. Hence, considering larger areas and/or expanding the model to 3D can become problematic. Many approaches use sparse GPs as a solution to this problem. Some examples can be found in [80] and [46]. Another option is using Gauss-Markov models as in [40] to describe the GP.

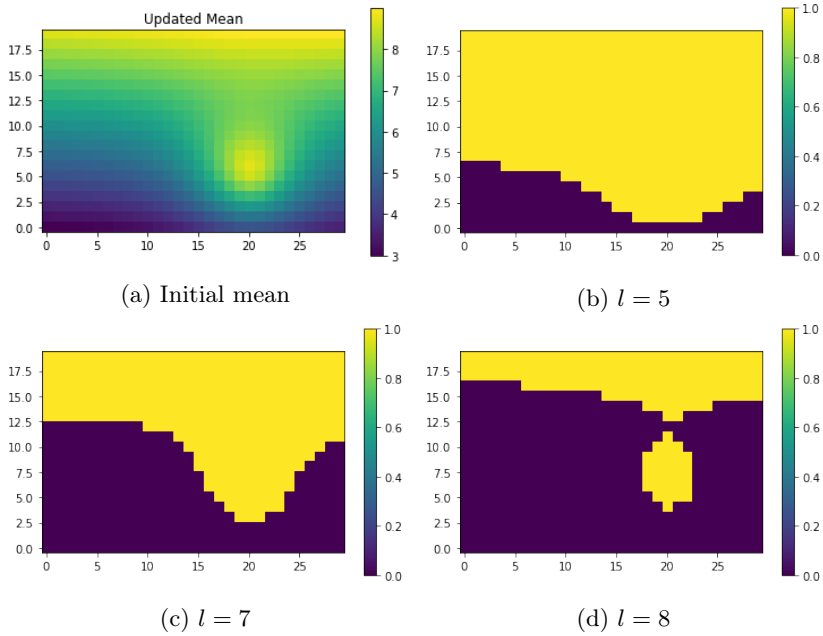

(a) Initial mean

(b) $l = 5$

(c) $l = 7$

(d) $l = 8$

Figure 3.2: Excursion sets for different values of the critical limit l given the Gaussian field in figure 3.2a. The yellow color represents the excursion sets.

Chapter 4

Spatio-temporal Model

> The ocean's currents are a turbulent emotion which man has yet to come to terms with.
>
> Anthony T. Hincks

In the previous chapter, the spatial part of the onboard model was presented. However, modeling the spatial correlations is not enough to give a good picture of the particle transportation near a seafill. Ocean dynamics are fundamentally turbulent, nonlinear and nonstationary. Hecnce, being able to incorporate knowledge about currents and changes with time is important. This chapter introduces time as a variable and spatio-temporal GPs are considered. A linear temporal model is built using an advection-diffusion stochastic partial differential equation (SPDE). It is shown how the linear SPDE model together with the Gaussian measurement model from the previous chapter can be written as a state-space model and a Kalman filter can be used to update the model.

4.1 Advection-Diffusion model

The spatio-temporal process of transport of a medium in a fluid can be expressed by the advection-diffusion SPDE [73]:

$$\frac{\partial X(t,\boldsymbol{s})}{\partial t} = \lambda X(t,\boldsymbol{s}) - \boldsymbol{c}(t,\boldsymbol{s})^T \nabla X(t,\boldsymbol{s}) + \nabla \boldsymbol{D} \nabla X(t,\boldsymbol{s}) + B(t,\boldsymbol{s}) + \epsilon(t,\boldsymbol{s}), \quad (4.1)$$

with $\boldsymbol{c}(t,\boldsymbol{s}) = (c_e(t,\boldsymbol{s}), c_n(t,\boldsymbol{s}))^T$ being the drift vector field for advection, $\boldsymbol{D}$ the diffusion matrix, $\epsilon(t,\boldsymbol{s})$ a noise term, ∇ the gradient operator $\left(\frac{\partial}{\partial s_e}, \frac{\partial}{\partial s_n}\right)$ and $\lambda \in [-1, 0]$ a damping constant controlling the autoregressive relationship between state vectors [68]. The damping constant relates to the concentration reduction over time, which in our case could describe the decay in concentration due to sinking. The noise term $\epsilon(t,\boldsymbol{s})$ is assumed to be a zero-mean Gaussian noise term that is uncorrelated in the temporal domain but spatially correlated. The source

term $B(t, \boldsymbol{s})$ describes external factors, e.g. boundary conditions. In this thesis, we assume horizontal isotropic diffusion leading to a constant diffusion parameter D.

To find a linear approximation of the SPDE, equation (4.1) is discretized using an upwind differencing scheme. We define the length of a time step as dt, and we define a spatial grid D_s with resolution ds_e in the east direction and ds_n in the north direction. Forward differences are used in time, giving

$$\frac{\partial}{\partial t}X(t, \boldsymbol{s}) \approx \frac{X(t + dt, \boldsymbol{s}) - X(t, \boldsymbol{s})}{dt}. \tag{4.2}$$

For the first derivative in space we alternate between forward and backward differences, based on the direction of the drift vector $\boldsymbol{c}_t$. In eastward direction we have

$$\frac{\partial}{\partial s_e}X(t, \boldsymbol{s}) \approx \frac{X(t, \boldsymbol{s} - (ds_e, 0)^T) - X(t, \boldsymbol{s})}{ds_e}, \quad \text{for} \quad c_e^t \geq 0 \tag{4.3}$$

$$\frac{\partial}{\partial s_e}X(t, \boldsymbol{s}) \approx \frac{X(t, \boldsymbol{s} + (ds_e, 0)^T) - X(t, \boldsymbol{s})}{ds_e}, \quad \text{for} \quad c_e^t < 0, \tag{4.4}$$

and in the northward direction

$$\frac{\partial}{\partial s_n}X(t, \boldsymbol{s}) \approx \frac{X(t, \boldsymbol{s} - (0, ds_n)^T) - X(t, \boldsymbol{s})}{ds_n}, \quad \text{for} \quad c_n^t \geq 0 \tag{4.5}$$

$$\frac{\partial}{\partial s_n}X(t, \boldsymbol{s}) \approx \frac{X(t, \boldsymbol{s} + (0, ds_n)^T) - X(t, \boldsymbol{s})}{ds_n}, \quad \text{for} \quad c_n^t < 0. \tag{4.6}$$

The second derivatives are discretized as follows,

$$\frac{\partial^2}{\partial s_e^2}X(t, \boldsymbol{s}) \approx \frac{X(t, \boldsymbol{s} + (ds_e, 0)^T) - 2X(t, \boldsymbol{s}) + X(t, \boldsymbol{s} - (ds_e, 0)^T)}{ds_e^2} \tag{4.7}$$

$$\frac{\partial^2}{\partial s_n^2}X(t, \boldsymbol{s}) \approx \frac{X(t, \boldsymbol{s} + (0, ds_n)^T) - 2X(t, \boldsymbol{s}) + X(t, \boldsymbol{s} - (0, ds_n)^T)}{ds_n^2}. \tag{4.8}$$

4.1.1 Boundary conditions

When solving the SPDE, boundary conditions are required. Given a rectangular grid, information about the edges of the rectangle must be given. There exists a variety of BCs depending on the physical property of the boundary. In this thesis, only Dirichlet BCs and Neumann BCs are considered. Dirichlet can be seen as a constant source along the boundaries and knowledge about the state values on the boundary is used. Another type of BCs is Neumann BCs which is defined by

$$\frac{\partial}{\partial s_e}X(t, \boldsymbol{s}) = 0, \tag{4.9}$$

for the locations s on the boundary. This The BC terms are all collected in the B vector in equation (4.1).

4.2 State-space representation

By scaling the time discretisation, a change in time can be denoted $t+1$ instead of $t+dt$. We have $\{t = t_0 + j \times dt; j = 0, 1, 2 \dots\}$. When inserting all the discretized terms into equation (4.1), the upwind scheme can be written as a linear process on the form

$$\boldsymbol{X}_t = \boldsymbol{A}_t \boldsymbol{X}_{t-1} + \boldsymbol{B}_t + \boldsymbol{\epsilon}_t, \quad \boldsymbol{\epsilon}_t \sim N(0, \boldsymbol{W}_t), \quad t = 1, \dots, T, \tag{4.10}$$

where $\boldsymbol{X}_t$ is the size $n \times 1$ vector of particle concentrations at time step t for all spatial locations, $\boldsymbol{A}_t$ is the $n \times n$ state transition matrix including information about advection, diffusion and damping, $\boldsymbol{B}_t$ is a matrix adding external information, in our case boundary conditions, and $\boldsymbol{W}_t$ is a positive definite variance-covariance matrix for the noise term $\boldsymbol{\epsilon}_t$. The initial distribution is specified as $\boldsymbol{X}_0 \sim N(\boldsymbol{\mu}_0, \boldsymbol{\Sigma}_0)$.

The state of particle concentrations is assumed to develop in space and time according to equation (4.10). The aim of data assimilation is to combine information from observations with this *prior* process knowledge to obtain an optimal sequential posterior or filtering estimate of the state at the current time.

Updating the distribution of $\boldsymbol{X}_t$ is done in two steps; the forecasting step and the filtering step. During forecasting the process model in equation (4.10) is taken into account and we get the distribution

$$\boldsymbol{\mu}_{t|t-1} = \boldsymbol{A}\boldsymbol{\mu}_{t-1|t-1} + \boldsymbol{B}_t \tag{4.11}$$

$$\boldsymbol{\Sigma}_{t|t-1} = \boldsymbol{A}\boldsymbol{\Sigma}_{t-1|t-1}\boldsymbol{A}^T + \boldsymbol{W_t}. \tag{4.12}$$

Further, we have the data model as in equation (3.9):

$$\boldsymbol{Y}_t | \boldsymbol{Y}_{1:t-1} \sim N(\boldsymbol{G}_t \boldsymbol{\mu}_{t|t-1}, \boldsymbol{Q}_t), \tag{4.13}$$

$$\boldsymbol{Q}_t = \tau^2 \boldsymbol{I}_m + \boldsymbol{G}_t \boldsymbol{\Sigma}_{t|t-1} \boldsymbol{G}_t^T \tag{4.14}$$

Lastly, the updating step is presented. Here, the added information from measurements is incorporated, and the forecasting distribution is obtained as

$$\boldsymbol{\mu}_{t|t} = \boldsymbol{\mu}_{t|t-1} + \boldsymbol{\Sigma}_{t|t-1}\boldsymbol{G}_t^T \boldsymbol{W}_t^{-1}(\boldsymbol{y}_t - \boldsymbol{G}_t \boldsymbol{\mu}_{t|t-1}), \tag{4.15}$$

$$\boldsymbol{\Sigma}_{t|t} = \boldsymbol{\Sigma}_{t|t-1} - \boldsymbol{\Sigma}_{t|t-1}\boldsymbol{G}_t^T \boldsymbol{Q}_t^{-1} \boldsymbol{G}_t \boldsymbol{\Sigma}_{t|t-1}^T. \tag{4.16}$$

This can be recognized as the spatial Kalman filter. Letting $\boldsymbol{Z}_t = (\boldsymbol{Y}_1, \dots, \boldsymbol{Y}_t)$ represent all observations and prior information up to time t, the filtering distribution is $\boldsymbol{X}_t | \boldsymbol{Z}_t \sim N(\boldsymbol{\mu}_{t|t}, \boldsymbol{\Sigma}_{t|t})$ with mean $\boldsymbol{\mu}_{t|t}$ and variance-covariance $\boldsymbol{\Sigma}_{t|t}$ defined by

$$\boldsymbol{\Sigma}_{t|t-1} = \boldsymbol{A}_t \boldsymbol{\Sigma}_{t-1|t-1} \boldsymbol{A}_t^T + \boldsymbol{W}_t \tag{4.17}$$

$$\boldsymbol{Q}_t = \boldsymbol{G}_t \boldsymbol{\Sigma}_{t|t-1} \boldsymbol{G}_t^T + \tau^2 \boldsymbol{I} \tag{4.18}$$

$$\boldsymbol{K}_t = \boldsymbol{\Sigma}_{t|t-1} \boldsymbol{G}_t^T \boldsymbol{Q}_t^{-1} \tag{4.19}$$

$$\boldsymbol{\mu}_{t|t-1} = \boldsymbol{A}_t \boldsymbol{\mu}_{t-1|t-1} + \boldsymbol{B}_t \tag{4.20}$$

$$\boldsymbol{\mu}_{t|t} = \boldsymbol{\mu}_{t|t-1} + \boldsymbol{K}_t(\boldsymbol{Y}_t - \boldsymbol{G}_t \boldsymbol{\mu}_{t|t-1}) \tag{4.21}$$

$$\boldsymbol{\Sigma}_{t|t} = \boldsymbol{R}_t - \boldsymbol{K}_t \boldsymbol{Q}_t \boldsymbol{\Sigma}_{t|t-1}^T. \tag{4.22}$$

Starting with the initial mean $\boldsymbol{\mu_0}$ and covariance matrix $\boldsymbol{\Sigma_0}$, the updating can be done sequentially as time passes.

4.3 List of Symbols

The spatio-temporal model presented in this chapter is used througout this thesis. This last section gives a summary of the model by providing a list of symbols used for the onboard proxy model.

List of Symbols

$\boldsymbol{X}$	Particle concentration
$\boldsymbol{\mu}$	Model mean
$\boldsymbol{\Sigma}$	Model covariance
σ^2	Model variance
R	Correlation function
$\boldsymbol{Y}$	Measurement vector
$\boldsymbol{\epsilon}$	Measurement error
τ^2	Measurement variance
$\boldsymbol{G}$	Measurement design matrix
n	Grid size
m	Number of measurements
t	Time
$\boldsymbol{s}$	Location
D	Diffusion
$\boldsymbol{c}$	Advection field
$\boldsymbol{A}$	Transition matrix
$\boldsymbol{B}$	Matrix containing information on boundaries
$\boldsymbol{W}$	Temporal covariance
$\boldsymbol{K}$	Kalman gain

Chapter 5

Parameter Specification

> Learn from the experts; you will not live long enough to figure it all out by yourself.
>
> Brian Tracy

In this chapter, we show how to utilize prior information from the ocean models described in chapter 2 to learn the spatio-temporal GP model from chapters 3 and 4. Brian Tracy said: "Learn from the experts; you will not live long enough to figure it all out by yourself." In our case, the expert knowledge comes from the numerical ocean and particle transport models. This chapter aims to specify the parameters of the initial state model and SPDE process model to describe the conditions surrounding the seafill in Frænfjorden.

Similar approaches, also utilizing prior knowledge to learn GP models, can be found in [13] who use an AUV to collect samples for ex-situ analysis, selecting the sampling locations based on previous mission data and maximizing a utility function, and in Ma et al. [45], who create a model of a spatio-temporal environment by learning and refining the hyperparameters of a GP kernel using prior ocean model data.

The parameter specification presented in this chapter is based on the work in **Paper C**. However, the approach throughout all the papers has been quite similar, with only minor variations.

5.1 Initial state

The initial state is defined by the mean and covariance $\boldsymbol{\mu}_0$ and $\boldsymbol{\Sigma}_0$. To specify the mean, forecast data from the particle transportation model DREAM is used. The prior mean $\boldsymbol{\mu}_0 = [\mu_{0,1}, \ldots, \mu_{0,n}]$ is set to be the DREAM prediction of the state at the start time of a mission. In the case of environmental sampling, it should be noted that measurements taken in a field with biological phenomena such as hotspots, i.e., a field with a couple of areas of high-value measurements, typically follow a log-normal distribution [30]. This is typically the case for particle

concentration in the Frænfjorden area. Hence, the log(concentration + 1) is used to specify the initial state.

Since ocean processes are affected by currents, wind patterns, bathymetry, and freshwater runoff, we will have elevated variability in some locations. Thus, we choose a non-stationary prior model [33] where the variance in each location is specified empirically from the training data available by DREAM. Saying, we have D realizations of training data; the empirical variance is given by,

$$\sigma_i^2 = \frac{1}{D-1}\sum_{d=1}^{D}(y_{i,d} - \mu_i)^2. \tag{5.1}$$

Here, $\mu_i = \frac{1}{D}\sum_{d=1}^{D} y_{i,d}$ is the empirical mean concentration in location $\boldsymbol{s}_i$ over all D realizations of training data. As, also stated in chapter 3, the prior covariance matrix $\mathbf{\Sigma_0}$ is given by

$$\mathbf{\Sigma_0} = \begin{bmatrix} \Sigma_{11} & \Sigma_{12} & \dots & \Sigma_{1n} \\ \Sigma_{21} & \Sigma_{22} & \dots & \Sigma_{2n} \\ \vdots & \vdots & \ddots & \vdots \\ \Sigma_{n1} & \Sigma_{n2} & \dots & \Sigma_{nn} \end{bmatrix}, \tag{5.2}$$

where $\Sigma_{ij} = \sigma_i \sigma_j R_{ij}$ and R_{ij} represents the spatial correlation. The diagonal of the covariance matrix in equation (5.2) contains the location-wise variances σ_i^2, and the off-diagonal elements describe the covariance between the locations.

A suitable correlation function R must be selected to find the initial covariance $\mathbf{\Sigma}_0$. To fulfill the two main properties for modeling spatial correlation (the decay with distance and the fact that covariance matrices must be positive definite), generic functions are used to define the initial covariance. Table 5.1 show three common correlation functions; The exponential, the Matern (3/2) and the Gaussian correlation function. Here, $h_{ij} = |s_i - s_j|$ is the Euclidean distance between two locations s_i and s_j.

Name	Function
Exponential	$\exp(-\phi h)$
Matern (3/2)	$(1+\phi)\exp(-\phi h)$
Gaussian	$\exp(-\phi h^2)$

Table 5.1: Three common correlation functions. Here, $h_{ij} = |s_i - s_j|$ is the Euclidean distance between two locations s_i and s_j, and ϕ is a parameter describing the correlation length of the functions.

Correlation functions are related to a concept called variograms, most used in spatial statistics [48]. The relation can be seen from the definition of the variogram given by [12]

$$\begin{aligned}\gamma(\boldsymbol{s}_i - \boldsymbol{s}_j) =& \frac{1}{2}\mathrm{Var}(X_t(\boldsymbol{s}_i) - X_t(\boldsymbol{s}_j)) \\ =& \frac{1}{2}(\mathrm{Var}(X_t(\boldsymbol{s}_i)) + \mathrm{Var}(X_t(\boldsymbol{s}_j)) - 2\mathrm{Cov}(X_t(\boldsymbol{s}_i), X_t(\boldsymbol{s}_j))).\end{aligned} \tag{5.3}$$

Rewriting this and inserting the isotropic correlation function R and an initial constant variance σ_0^2 we get

$$\gamma(h) = \sigma_0^2(1 - R(h)). \tag{5.4}$$

When choosing an appropriate correlation function, variogram analysis is often used. The appropriate function is then chosen by matching the shape of the curve of the experimental variogram to the shape of the curve of the mathematical variogram function. Figure 5.1 shows the fitting of empirical variogram data from DREAM. Three variograms were fitted to the training data. All of them fit the empirical variogram well, but the Matern variogram [47] was chosen because it has a smoothness that fits the DREAM data well. The spatial variance term and the spatial correlation length describe the effective variability and dependence structure of the particle concentration field. Here, a variance of 0.6 and a spatial correlation length of about 500 m results are supported by the physical ocean model data. The advection-diffusion parameters are set from the physical assumptions going into the ocean model. From visual inspection, this GP model appears to give reasonable simulations of the field but with more patchy randomness than what is seen in the ocean model. As commonly seen in physical model data, the variogram computed from the ocean models data starts to fluctuate after a while, which can be related to physical principles in many cases. We decided not to fit a variogram to these features to avoid overfitting the data. Notably, the GP model is a statistical proxy model that can be run onboard but is potentially missing some large-scale oceanographic features. The ocean model is a numerical description with much skill but potentially getting systematic bias due to misspecified inputs growing with time. They both have their merits.

5.2 SPDE parameters

In addition to the initial state, the parameters in the SPDE need to be specified. We specify the advection and diffusion parameters in equation (4.1) together with the BCs represented by $\boldsymbol{B}_t$ using prior knowledge about the ocean dynamics in the selected survey area. Forecasts of the currents from SINMOD are used to set the velocity field $\boldsymbol{c}_t$ from physical assumptions, which is further used to build the transition matrix $\boldsymbol{A}_t$ as described in Chapter 4. We specify a small damping value $\lambda = -0.0010$ and diffusion constant $D = 0.1$ m^2/s. The covariance matrix $\boldsymbol{W}_t$ is set to have the same correlation structure as the covariance matrix for the initial state $\boldsymbol{\Sigma_0}$, giving $\boldsymbol{W}_t = V\boldsymbol{\Sigma}_0$, where $V < 1$ is a scaling parameter for the dynamic variance compared with the larger initial variance. Considering this in relation to

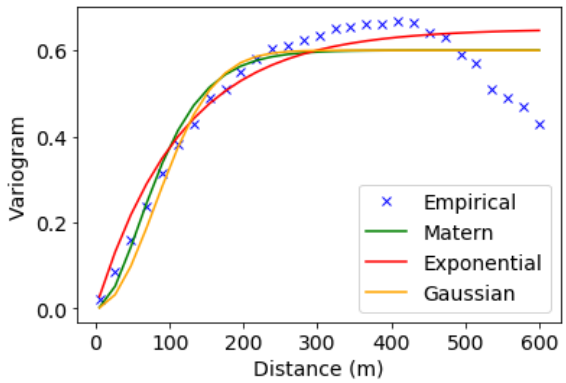

Figure 5.1: Fitted variogram to empirical data. The Matern(3/2) was chosen with a correlation length of about 500m and variance of 0.6.

the original continuous time SPDE, the discretization in time would also impact this variance, but in our work, we use a fixed time discretization equal to the one used onboard.

The boundary conditions (BCs) for the SPDE must also be considered, and there are several approaches for setting the BCs. For the boundary conditions (BCs) in the SPDE, we use Dirichlet BCs on the two sides from which the currents flow. This can be considered a constant forcing along these sides and is chosen because of the constant flow of particles entering the area. We assume an open ocean with no change at the boundaries on the remaining sides of the survey area and therefore use Neumann BCs. All BC terms are added to the $\boldsymbol{B}_t$ vector on the right-hand side of equation (4.1). The sides where Dirichlet BCs are used can change during a mission if the current changes direction. In the Frænfjorden area, changes in direction frequently occur as the tides change. Figure 5.2 show an example output from SINMOD. In this example, Dirichlet BCs is used on the eastern and northern side.

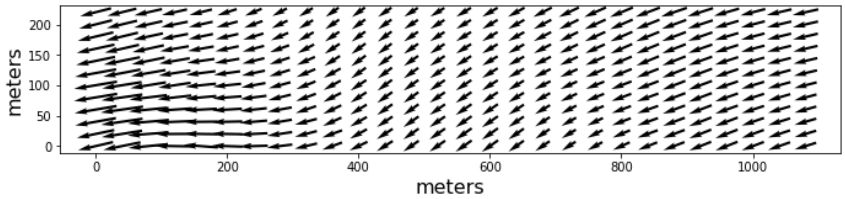

Figure 5.2: An example output of ocean current data from SINMOD. The data is used to set the advection field $\boldsymbol{c}$. The currents also decide how the boundary conditions are defined. In this example, Dirichlet BCs is used on the eastern and northern side. Furthermore, Neumann BCs are used on the southern and western side.

5.3 Closing remarks

This part of the thesis has defined the onboard model and builds the foundation for the following parts of the thesis. The onboard model is based on GPs and an advection-diffusion SPDE to create a spatio-temporal model for describing the dynamic transportation of particles underwater. Parameters are specified based on ocean model data from Frænfjorden.

Part II

Adaptive Sampling

Chapter 6

Objective function

> It's not hard to make decisions once you know what your values are.
>
> Roy E. Disney

The onboard model from the previous part can be seen as the best estimate of the current state of the ocean, and is a useful tool for choosing informative sampling locations. The question now is: "Where and when should we sample?" Sophisticated sampling strategies are needed to exploit the benefits that robotic platforms have regarding autonomy and high mobility. To obtain the most scientifically relevant measurements effectively, adaptive approaches need to be developed. In contrast to static/pre-scripted schemes, adaptive/data-driven strategies can react to measured conditions, having access to both prior and in situ information. The selection of sampling location can now depend on past observations and the developed onboard spatio-temporal model.

Roy E. Disney said: "It's not hard to make decisions once you know what your values are." And this is the main question for this chapter. We need to determine what values we want to base our decisions on. In the adaptive sampling process, we need to decide where to travel. This chapter suggests an objective function that aims to guide the AUV to informative sampling locations. The function is first described in **Paper A**, and is further used in **Papers B, C and E**. Two simulation studies are presented in this chapter; a static study from **Paper A** and a dynamic study from **Paper C**.

6.1 Objective function

An objective function is suggested to obtain an informative path for the AUV. The function is created based on three criteria:

1. Locations with high variance are preferred
2. Locations with high predicted concentration are preferred

3. Locations leading to a suitable travel length within the next time interval for the AUV are preferred.

The first criterion is chosen because sampling in areas with a high model variance will reduce the total variance, hence creating a more accurate model. This criterion also ensures that the AUV travels to unexplored areas. The second criterion makes the method adaptive. When studying the simulation results of the particle transport from the complex model, it is clear that the variability is highest where there is a high concentration of particles. Hence, the criterion is inspired by this observation and assumes that locations with high predicted concentration will be rich with information. The last criterion comes from the travel length limitations of the AUV. When choosing the next sample location, it is also essential that the AUV does not travel too far, assuring that the risk of the vehicle drifting outside the survey area is kept low.

The suggested objective function is then created by having a term for the first two criteria. At time step t for location s_i, the objective function is given by

$$f_t(\boldsymbol{s}_i) = \theta_1 \sigma^2_{i,t|t} + \theta_2 \mu_{i,t|t}, \tag{6.1}$$

where the constant parameters $\boldsymbol{\theta} = [\theta_1, \theta_2]$ define the weighting for each criterion. Deciding the weighting of criteria 1 and 2 depends on design choices. When the goal is to obtain a good map of the overall region, then criterion 1 should be dominating. However, if hotspots are the main focus, criterion 2 should dominate. In our case, the parameters $\boldsymbol{\theta}$ are tuned in simulation to obtain a good balance between the two criteria.

The chosen sampling location $\boldsymbol{s}^\star_t$ at time step t is determined as the location that maximizes the objective function $f_t(\boldsymbol{s}_i)$ for $\boldsymbol{s}_i \in [\boldsymbol{s}_1, \ldots, \boldsymbol{s}_n]$. Given the previous sampling location $\boldsymbol{s}^\star_{t-1}$, we choose the next sampling location as

$$\begin{aligned} \boldsymbol{s}^\star_t = \arg\max_{\boldsymbol{s}_i} \quad & f_t(\boldsymbol{s}_i) \\ \text{s.t.} \quad & |\boldsymbol{s}^\star_{t-1} - \boldsymbol{s}_i| \geq d_{\min} \\ & |\boldsymbol{s}^\star_{t-1} - \boldsymbol{s}_i| \leq d_{\max}. \end{aligned} \tag{6.2}$$

The constraints on the objective function ensure that the third criterion in the objective function is adhered to by choosing $d_{\min}$ and $d_{\max}$ such that a suitable travel length is obtained. $|\boldsymbol{s}^\star_{t-1} - \boldsymbol{s}_i|$ is the Euclidean distance between the previous sampling location and $\boldsymbol{s}_i$. Equation (6.2) is solved using brute-force enumeration; the value of the objective function (equation (6.1)) is found for all the grid cells within the region defined by the constraints in equation (6.2). The next sampling waypoint $\boldsymbol{s}^\star_t$ is chosen as the grid cell with the highest objective value. In this paper, ocean currents are included in the spatio-temporal proxy model, but they are not considered in the AUV navigation plans for selecting sampling locations. Rather, the AUV is set to surface often to avoid risk and reduce navigation uncertainty, as described in the experimental section. In a larger-scale mission, it would certainly be beneficial to include more of the ocean currents in the sampling strategy. Making the AUV fly with the currents may increase endurance and reduce travel time between waypoints. This topic is amongst others explored in [58] and should be considered in future work.

6.2 Summary of the suggested approach

We now provide an overview of the suggested approach. At the beginning of the deployment, the GP model is initialized. The following steps are executed:

- Kernel hyperparameters are estimated using prediction and hindcast data from the particle transportation model DREAM.
- The initial GP state defined by $\boldsymbol{\mu}_0$ and $\boldsymbol{\Sigma_0}$ are found.
- Ocean current prediction data from SINMOD is used to define the advection fields $\boldsymbol{c}_t$, which is used together with the diffusion constant D to define transition matrices $\boldsymbol{A}_t$.
- Particle transportation data from DREAM defines the boundaries that are incorporated in the vector $\boldsymbol{B}_t$.

The sampling method starts out either with the initial GP model or with the latest updated GP model.The AUV performs adaptive sampling choosing the next waypoint using the objective function. The onboard model of the AUV is then updated; the field is moved with the currents, and new information from observations is added. Updating is executed whenever a waypoint is reached, using data from observations taken along the AUV transect in the assimilation. An overview of the adaptive sampling method is given in Algorithm 1.

Algorithm 1 Adaptive Sampling method

```
Initialize GP model (Chapter 5)
while running do
    Select new waypoint using (6.1)
    Travel to new waypoint and collect observations
    if waypoint is reached then
        Update GP model with observations using (4.22)
    end if
end while
```

6.3 Simulation Study: Static example

The first simulation study considers a static example. In this example, the transition matrix $\boldsymbol{A}_t$ from equation (4.22) is an identity matrix so that $\boldsymbol{X}_{t+1} = \boldsymbol{X}_t$. Hence, the field is not moved with the currents and observations through sampling is the only thing affecting the updated field.

Data from DREAM was used to train the GP, and to create the prior mean $\boldsymbol{\mu}_0$ and covariance $\boldsymbol{\Sigma}_0$ as descried in Chapter 5. For simplicity, only a small area around the seafill was considered (2560 m $\times$ 1280 m) and the area was divided into a regular grid with grid cells of size 32 m $\times$ 32 m. Also, in this initial simulation only one depth layer was considered at $\approx$ 15 m depth, but this could be expanded to 3 dimension considering multiple snapshots in different depth layers. Figure 6.1 shows the bathymetry of the fjord and the selected area as a red rectangle. From the training data it was observed that the distribution of particles in the location of

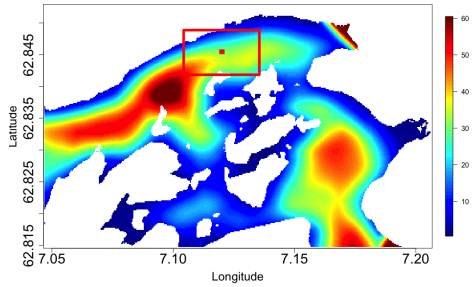

Figure 6.1: Plot of the bathymetry of Frænfjorden. The red rectangle shows the selected area, and the red dot indicates the location of the seafill.

the seafill was rapidly changing and had very little correlation with the neighboring sites. Thus, this location was disregarded in our model. When plotting the results, this was handled by setting the variance to 0 in the location, and using the true value from the test data as the mean.

The spatial model and the sampling method was implemented using the language R [63], and test data from DREAM (April 2nd) was used as sensor readings for the AUV. Hence, for this simulation we consider the test data from DREAM to be the true distribution at all time. The time steps was discretized into intervals of 5 minutes. A total of 54 updates were simulated, which corresponds to monitoring the outlets for 4.5 hours (270 minutes).

The results of the simulation study is shown in Figure 6.2, showing results at four different time steps. The particle concentration is measured in $\mu g/L$ (log(concentration) is not used in this study), and the color bar shows the intensity at each location. The x-and y-axis shows the distance in metres from the seafill. The first column of plots shows to the true values from DREAM. The predicted particle concentration is shown in the second column, and the third column shows the prediction variance together with the path of the AUV showing the 10 most recent sampling locations as small white dots and the current position of the AUV as a large white dot.

Comparing the predicted particle concentration with the truth from the test data it can be seen that the sampling method generally gives a smooth prediction that coincides quite well with our "true" distribution. Still, many of the finer details are overlooked, and more samples are needed to model these details.

Considering the path of the AUV together with the prediction variance, it can be seen that the variance is decreased near the recently sampled locations. The increase in variance proportional to the prior variance can also be clearly seen in the prediction variance plots.

The objective function controls the AUV path in an intuitive way, leading it to unexplored areas on the one hand, and in most cases assuring a reasonable travel speed for the AUV between sampling locations. The travel distance of the AUV lies between 100-300 metres for most time steps, which is a suitable distance given the time step length and the AUV speed. Still, the method sometimes results in

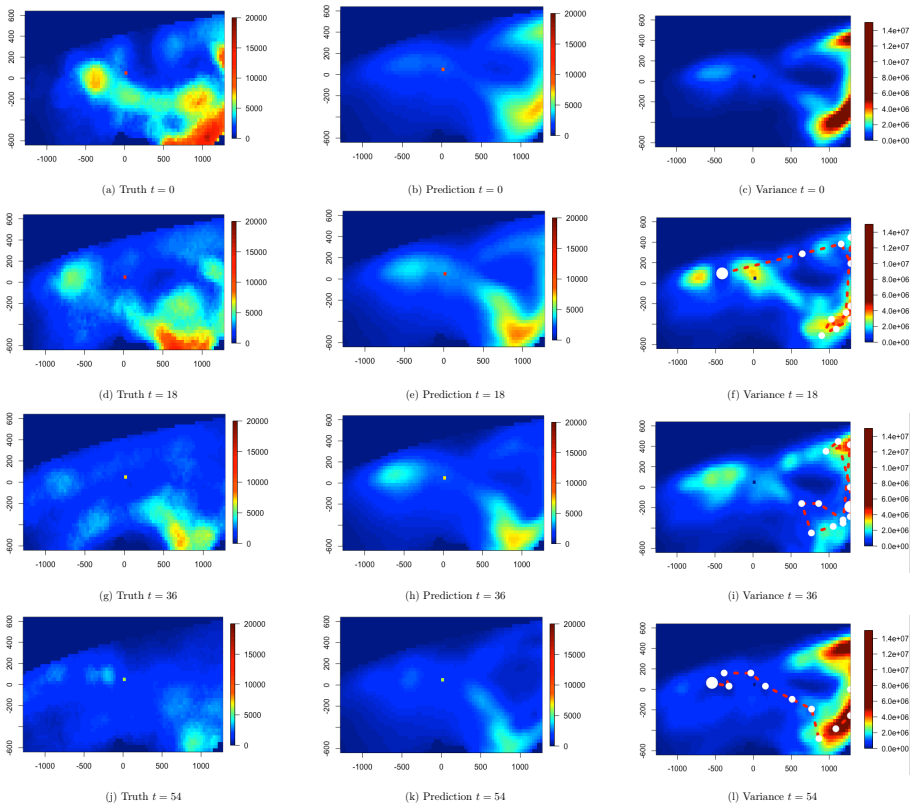

Figure 6.2: Results of the simulation study at four different time steps $t = 0, 18, 36, 54$ corresponding to [0,90,180, 270] minutes. The particle concentration is measured in $\mu g/L$, and the color bar shows the intensity at each location. The x- and y-axis shows the distance in metres from the seafill. The first column of plots corresponds to the true values (a),(d),(g) and (j). The predicted mean particle concentration is shown in the second column (b), (e), (h) and (k), and the third column corresponds to the prediction variance (c), (f), (i) and(l). The path of the AUV is plotted as a red line, the small white dots shows the 10 most recent sampling locations and the large dot indicates the current position of the AUV.

the AUV taking too large steps, a clear example can be seen in (f). A possible improvement could be obtained by better tuning of the parameters $\boldsymbol{\theta}$, but this would only help to a certain degree. Perhaps a better idea for future work would be to add constraints to the travel length of the AUV when doing path planning.

Another issue with the model, is that it does not seem to keep up with the rapid dynamics of the ocean process. Since the model relies on the observations from the AUV to capture the change in the particle concentration, the prediction results far from recently sampled locations will be inaccurate. When the dynamics of the particle transportation are fast, we will get a delay in the updating of the model. As an example, the prediction results in the upper left area can be considered. At

t=18, the prediction in this area shows a smaller concentration than the true value. Then at t=36, the predicted concentration has increased in this area, but in the true model the particles have moved resulting in a low density. Finally, at t=54 the predicted and the true value is quite similar. This example shows the delay in the predicted values. And this clearly shows the need for a temporal model onboard the AUV, which is explored in the following simulation study.

6.4 Simulation Study: Dynamic example

We now present a simulation study including the whole spatio-temporal model presnted in chapters 4 and 6. This model is compared with four simpler strategies. We vary both the process model and the sampling strategy. The temporal model based on the advection-diffusion SPDE is compared to a stationary process model where the next time step is equal to the previous time step, as in the previous simulation study. Different sampling strategies are tested using the sampling strategy based on the suggested objective function, a predefined sampling strategy following a lawnmower pattern and a method that uses only the SPDE model with no sampling. For the strategy using the objective function we choose the travel distance restrictions $d_{\min} = 180$ meters and $d_{\max} = 220$ meters and set the time between each sample to be 5 minutes. This gives a suitable travel speed for the AUV, and a constant time step simplifies the updating of the temporal model. When using the lawnmower pattern, the distance between each sampling location is set to 200 meters and the same time step of 5 minutes is used. An overview of the different strategies can be seen in Table 6.1.

Ocean model data from two consecutive days, 1st and 2nd of April 2013, is used in the simulation study. The data from 1st of April is used to train the SPDE parameters as described in Chapter 5. Data from 2nd of April is used as the test data meaning that the predicted field on the 2nd of April is our ground truth and the field where observations (samples) are drawn from. We use realizations of the GP prior as the initial belief and run 100 replicate runs with the presented sampling methods in Table 6.1. We set the measurement error standard deviation $\tau = 0.5$ log(ppb). We simulate for a total of 6 hours aiming to map the field on 2nd of April from 15:00 to 21:00.

6.4.1 Results and discussion

In this section we present results from the simulation study and discuss the performance of the methods.

Performance measures

To evaluate the different methods, three performance measures are studied. The mean absolute error (MAE) is computed as the mean of the absolute error between the predicted concentration $\boldsymbol{\mu}_{t|t}$ and the true field from DREAM (2nd of April) for all the grid cells and time steps. The mean standard deviation (MSD) is computed similarly, but then focusing on the standard deviation in the proxy model in all grid cells at all time steps. Lastly, we compute the mean objective value (see equation

Table 6.1: Overview of the 5 methods used for comparison in the simulation study.

Method	Process model	Sampling Strategy
SPDE-Obj	SPDE	Objective
SPDE-Lawn	SPDE	Lawnmower
SPDE	SPDE	No sampling
Obj	Stationary	Objective
Lawn	Stationary	Lawnmower

(6.1)) (MO) in all grid cells at every time step. Table 6.2 shows these performance measures computed as the mean over the total time steps. Figure 6.3 shows how the mean objective value (MO) (see equation (6.1)) evolves through time, plotting the mean value for every time step.

Considering the MAE values in Table 6.2, we see that SPDE-Obj has the best performance in this case. The inclusion of a non-stationary process model increases the performance of the method, as this is the case using both the Obj sampling strategy and the Lawn sampling strategy. The objective function also increases the performance of the method compared to the pre-planned lawnmower strategy. Considering the MSD and MO measures, the SPDE method stands out with significantly higher values compared to the other methods. This is due to the method doing no sampling at all, and hence there is no way for this method to decrease the proxy models´ variance, both affecting the standard deviation and the objective values.

The effect of increasing variance with no sampling, can also be seen in Figure 6.3. Again, the SPDE method stands out with steadily increasing values while the other methods stabilize at a mean objective value between 200 and 300. For both lawnmower methods (SPDE-Lawn and Lawn) periodical fluctuations in the objective function can be observed. This occurs when the sampling is done close to the east end of the survey area where the assimilation with new data affects a smaller part of the modeled field compared to adding information in the center. Generally, the Obj and SPDE-Obj methods have a lower overall mean objective function compared with the other methods, indicating an intelligent sampling design.

Sampling design and field predictions

Figure 6.4 shows the AUV path and waypoints for the different sampling strategies plotted on top of the standard deviation at every hour of the simulation study. The same lawnmower pattern is used for both SPDE-Lawn and Lawn and can be seen in the first column of the figure. The path chosen by the Obj and the SPDE-Obj

Table 6.2: Performance measures for the five methods. The table shows the mean absolute error (MAE), the mean standard deviation (MSD) and the mean objective function value (MO).

Method	MAE	MSD	MO
SPDE-Obj	0.76	2.38	209.3
SPDE-Lawn	0.87	2.67	272.8
SPDE	1.11	4.70	848.1
Obj	0.85	2.52	230.2
Lawn	0.99	2.67	280.5

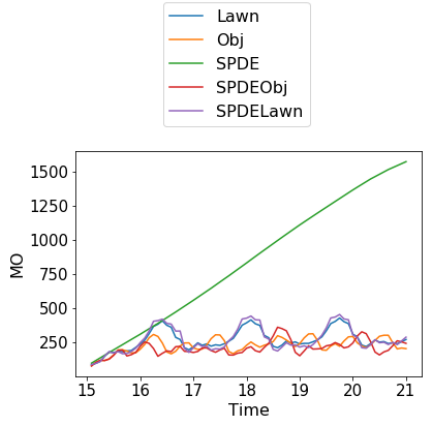

Figure 6.3: The mean objective value (MO) (see equation (6.1) computed over all the grid cells for each of the methods.

method can be seen in respectively the second and third column. All of the methods cover the area quite well, but both Obj and SPDE-Obj focus on the eastern area. This region is closer to the outlet and the true mine tailings distribution (seen in the first column of Figure 6.6) shows elevated concentrations in this area. Hence, more frequent sampling here is expected because of the proposed objective function (see equation (6.1)).

Figure 6.5 gives insight on how the GP methods behave, showing the distribution in one single grid cell over time using SPDE-Obj. The blue line shows the method´s mean value, the green line is the true value and the two red dotted lines are the 95% confidence interval. The point we are considering is located 340 meters east and 200 meters north in the survey area. When sampling and assimilation is

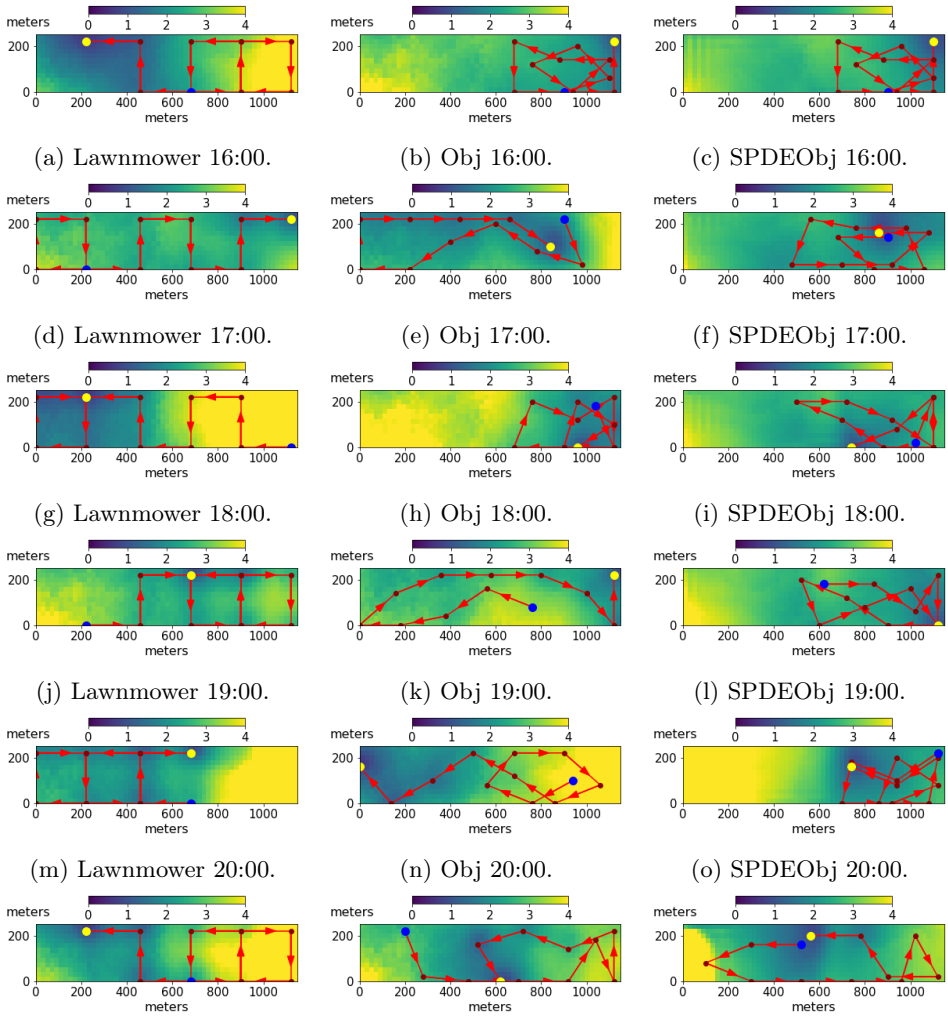

(a) Lawnmower 16:00. (b) Obj 16:00. (c) SPDEObj 16:00.

(d) Lawnmower 17:00. (e) Obj 17:00. (f) SPDEObj 17:00.

(g) Lawnmower 18:00. (h) Obj 18:00. (i) SPDEObj 18:00.

(j) Lawnmower 19:00. (k) Obj 19:00. (l) SPDEObj 19:00.

(m) Lawnmower 20:00. (n) Obj 20:00. (o) SPDEObj 20:00.

(p) Lawnmower 21:00. (q) Obj 21:00. (r) SPDEObj 21:00.

Figure 6.4: Hourly plot of the model standard deviation at the given time together with the path for the different sampling strategies up until that time. The blue dot shows the starting point of the path and the yellow is the sampling location at the current time. The arrow indicates the direction of the AUV.

done close to this point we see a reduction in the confidence interval and the mean value tends to be corrected towards the true value.

In Figure 6.6 we focus on the two methods Obj and SPDE-Obj. The updated model mean for every hour is plotted in column 2 and 3, and the true field (the field where the observations are drawn from) can be seen in the first column. Comparing the methods with the true field, they both capture the trend quite well. This figure illustrates an important difference between the two methods; the

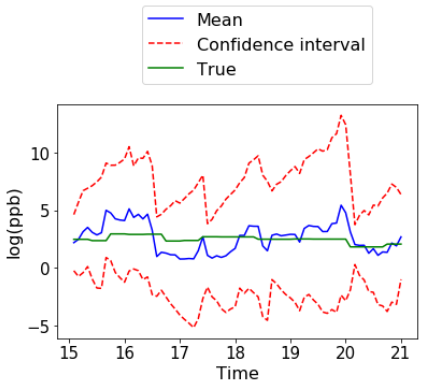

Figure 6.5: The distribution in one single grid cell using the SPDE-Obj method. Showing mean (blue line) and 95% confidence interval (red dotted lines) together with the true value (green line).

Obj method, because of its stationary process model, keeps the structure from the GP prior in the beginning throughout the whole mission, relying on observations to change its predicted field. This is not the case with SPDE-Obj which has a non-stationary process model that moves the field with the currents. Although data from two different days are used as training and test data, both datasets are from the same ocean models. This may cause the comparison with ground-truth to be optimistic. Still, based on the simulation results, it is reasonable to assume that SPDE-Obj is able to map the field quite well. Studies from simulations not included in this paper have shown that the performance of the SPDE-Obj compared with simpler strategies is improved with increasing survey area, showing the utility of an adaptive method for a large area survey.

Adaptive vs. pre-planned designs

We now give an example comparing an the adaptive approach (SPDEObj) with a pre-planned method (SPDELawn) (see Figure 6.7). The example shows the predicted results at the end of a mission run of total 5 hours. The true field is seen in Figure 6.7a. Figures 6.7b and 6.7c show the model mean and variance for the adaptive approach, and figures 6.7d and 6.7e present the model state for the pre-planned approach. The AUV path describing the sampling design for one hour before the end time is shown in the variance plots.

In the example, the adaptive approach gives a better estimate of the true field than the pre-planned method. From the true field, we observe increased concentrations on the eastern side. The adaptive approach captures this information, and because of elevated values in the area, continues to investigate the eastern side. The pre-planned lawnmower approach, on the other hand, is set to sample in the western area at the time, and the samples taken are not as informative. Adaptive approaches excel when conditions are not as expected. In such cases, the flexibility of an adaptive approach is beneficial since the sampling design is automatically

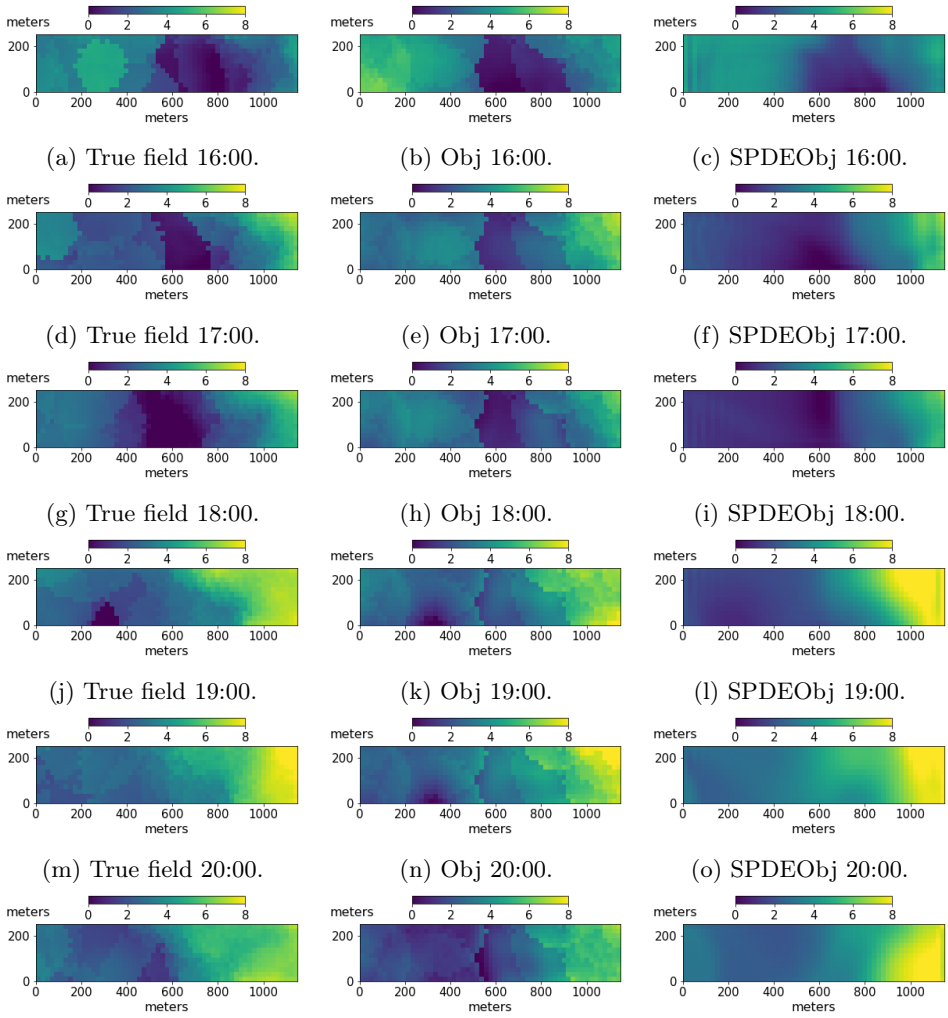

(a) True field 16:00. (b) Obj 16:00. (c) SPDEObj 16:00.

(d) True field 17:00. (e) Obj 17:00. (f) SPDEObj 17:00.

(g) True field 18:00. (h) Obj 18:00. (i) SPDEObj 18:00.

(j) True field 19:00. (k) Obj 19:00. (l) SPDEObj 19:00.

(m) True field 20:00. (n) Obj 20:00. (o) SPDEObj 20:00.

(p) True field 21:00. (q) Obj 21:00. (r) SPDEObj 21:00.

Figure 6.6: Hourly plot of the "true" value together with the model mean value for the Obj and SPDE-Obj method.

adjusted. A pre-planned approach will always stick to the pre-scripted sampling design.

6.5 Closing remarks

Two simulation studies are presented in this chapter. Both utilizes the suggested objective function for waypoint selection. The static simulation study reconstructs the true field quite well. Still, the temporal variability of the particle transporting was faster than the AUV could keep up with, indicating that more samples or

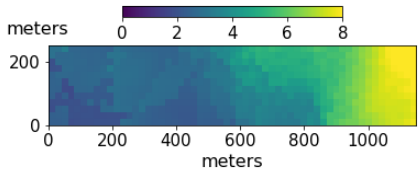

(a) True field after 5 hours of sampling.

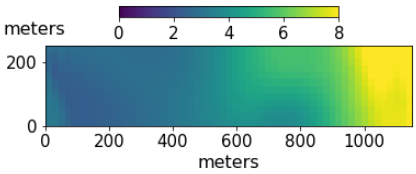

(b) Predicted model mean using the adaptive approach SPDEObj.

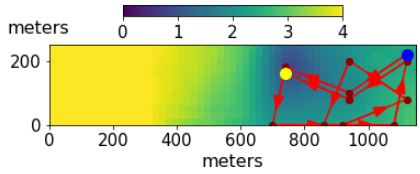

(c) Model variance of the adaptive approach SPDEObj. The AUV path one hour before the current state are shown in red.

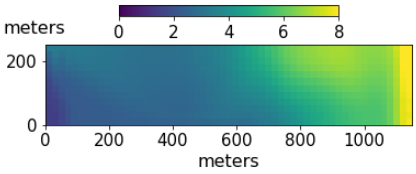

(d) Predicted model mean using the pre-planned approach SPDELawn.

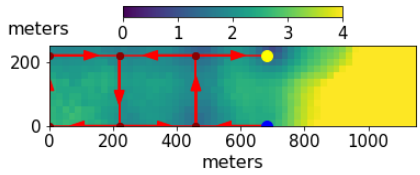

(e) Model variance of the pre-plannned approach SPDEObj.The AUV path one hour before the current state are shown in red.

Figure 6.7: Example run comparing a pre-planned approach with an adaptive approach. The true field after five hours of sampling can be seen in Figure 6.7a. Figures 6.7b and 6.7c show the model mean and variance for the adaptive approach, and figures 6.7d and 6.7e present the model state for the pre-planned approach. The AUV path showing the sampling design for one hour before the current time is shown in the variance plots.

a better temporal model is required. The second simulation study includes the temporal model. In this example, the method is compared with simpler models and sampling strategies. It can be seen that the SPDE process model gives improved prediction results in a dynamic environment, and the sampling strategy using the suggested objective function performs better than the sampling strategy using a simpler pre-planned lawnmower design. Although the model simulations are done only for the Frænfjorden case, the methods can be generalized for other cases as well. The method can both explore an area and focus on hot spot areas, and the balance between exploration/exploitation can be tuned using the parameters in the objection function. Hence, the method will apply to various other sampling cases.

Chapter 7

Excursion sets

When mine tailings are deposited in a fjord, the contamination must be monitored to predict reasonably that the environmental damage is below a critical level. In the previous chapter, the sampling strategy focused on obtaining the best possible field estimate of particle concentration near a seafill. In this chapter, the goal is changed from field estimation to deciding which areas are below and which areas are above a critical limit.

The monitoring of contaminants must build on a criterion, and we here focus on mapping spatial regions where the concentration is above a specified critical threshold at the end-time of the considered monitoring interval. This chapter is based on the results in **Paper D**. The resulting spatial subdomain with concentrations above the threshold limit is called an excursion set (ES). The design criterion for effective monitoring minimizes the expected mis-classification probabilities associated with the ES. There has recently been interest in studying ESs for environmental applications: [1, 24] explore extreme precipitation. [7] show an application with air pollution exceeding the limits set by the European Union. [75] use ESs to study temperature changes.

Within these modeling assumptions, we develop closed-form solutions for the expected reduction in mis-classification probabilities and use these to construct adaptive sampling designs that run in real-time on the AUV. The contribution extends related work on expected Bernoulli variance reduction [11, 22], presenting an approach applicable to spatio-temporal domains. In doing so, we combine spatio-temporal GPs, ESs, and AUV technology elements for an environmental application. Results are compared with state-of-the-art design approaches, as well as with simplified statistical models. Field experiments demonstrate the applicability of the methods for real-world environmental sensing.

7.1 Excursion Set

Let l be the critical limit of the system. A random ES over the domain $\mathcal{D}_s$ at time t' is here defined as

$$\mathrm{ES}_{t'} = \{\boldsymbol{s}_i \in \mathcal{D}_s : X_{t'}(\boldsymbol{s}_i) > l\}. \tag{7.1}$$

In this context, t' is a particular time of interest, where one in our case can possibly take some action to mitigate the concentration level by for instance reducing the mining deposition rates. This reference time will typically be the latest monitoring time $t' = t_n$. Note that expression (7.1) defines just one of several kinds of ESs [7, 8].

Just before time $t \leq t'$, assume data $\mathcal{Y}_{1:t-1}$ is available. The marginal EPs associated with the ES in equation (3.13) are

$$\mathrm{EP}_{t'}(\boldsymbol{s}_i) = P(X_{t'}(\boldsymbol{s}_i) > l \,|\, \mathcal{Y}_{1:t-1}), \quad \boldsymbol{s}_i \in \mathcal{D}_s. \tag{7.2}$$

From these EPs, the mean mis-classification probability (MMP) is defined by

$$\mathrm{MMP}_{t'} = \frac{1}{N}\sum_{i=1}^{N} \min\{1 - P(X_{t'}(\boldsymbol{s}_i) > l \,|\, \mathcal{Y}_{1:t-1}), P(X_{t'}(\boldsymbol{s}_i) > l \,|\, \mathcal{Y}_{1:t-1})\}. \tag{7.3}$$

This MMP is dominated by the probabilities that are near 0.5.

At time t, the design question relates to the augmentation of data $\mathcal{Y}_{1:t-1}$ with a random sample $\boldsymbol{Y}_t^d$ according to design d which is highlighted in the notation. This design must be among the possible designs $\mathcal{D}_t \subset \mathcal{D}_s$ at that time. In this chapter, the term design. However, it should be noted that this is comparable to the selection of sampling waypoint $\boldsymbol{s}^\star$ from the previous chapter. There are several strategies for selecting the design. For the optimal design choice at time t, one must in principle consider all possible positions and measurement values for steps $t+1, \ldots, t_n$. This becomes an intractable optimization problem involving a sequence of interrelated minimizations and integrals. Instead, we present heuristic methods considering only the current time step.

We focus here on a myopic strategy that is statistically optimal according to the expected MMP (EMMP) when assuming that one conducts no more measurements after time t. The optimal design is then

$$\begin{aligned} d_t^* &= \mathrm{argmin}_{d\in\mathcal{D}_t}\mathrm{EMMP}_{t'}^d, \\ \mathrm{EMMP}_{t'}^d &= \int_{\boldsymbol{y}_t^d} \frac{1}{N}\sum_{i=1}^{N} \min\{1 - p_{i,t'}^d, p_{i,t'}^d\} p(\boldsymbol{y}_t^d|\mathcal{Y}_{1:t-1}) d\boldsymbol{y}_t^d, \\ p_{i,t'}^d &= P(X_{t'}(\boldsymbol{s}_i) > l \,|\, \mathcal{Y}_{1:t-1}, \boldsymbol{y}_t^d), \end{aligned} \tag{7.4}$$

where $p(\boldsymbol{y}_t^d|\mathcal{Y}_{1:t-1})$ is the probability density function (pdf) of $\boldsymbol{Y}_t^d$, conditioned on the previous samples $\mathcal{Y}_{1:t-1}$.

In the spatio-temporal sampling scheme, the choice of design is done conditional on all data up to time $t-1$, and the probabilities can be computed for a future time t', while the expectation is over data at time t. The choice d determines the 1 and 0 structure of the design matrix $\boldsymbol{G}_t = \boldsymbol{G}_t^d$, where the design is again highlighted in the superscript. Of course, the available data $\mathcal{Y}_{1:t-1}$ were also gathered according to a chosen design, but this is ignored in the notation. The only effect of this design is via the conditioning in the probabilistic model and the current position which determines the design set $\mathcal{D}_t$.

7.1.1 Closed form expressions for EMMP

From the data assimilation expressions (equation (4.22)), we have the predictive Gaussian distribution for $X_{t'}(\boldsymbol{s}_i)$. Moreover, just before time t, the predictive distribution for the next observation is $\boldsymbol{Y}_t^d|\mathcal{Y}_{1:t-1} \sim N(\boldsymbol{G}_t^d\boldsymbol{\mu}_{t\,|\,t-1}, \boldsymbol{Q}_t^d)$. The superscript d notation is included again to emphasize the dependence on the design.

To facilitate the EMMP calculations in equation (7.4), we introduce variables

$$U_i^d = \frac{l - \mu_{t'|t}^d(i)}{\sqrt{\boldsymbol{\Sigma}_{t'\,|\,t}^d(i,i)}}, \quad i = 1, \ldots, n. \tag{7.5}$$

Here, $\mu_{t'|t}^d(i)$ is the ith component of the predictive mean and $\Sigma_{t'|t}^d(i,i)$ the ith diagonal element of the predictive covariance matrix, after the assimilation of $\mathcal{Y}_{1:t-1}$ and the new sample $\boldsymbol{Y}_t^d$. The random variable U_i^d is linearly related to $\boldsymbol{Y}_t^d$ via $\mu_{t'|t}^d(i)$, and it is hence Gaussian distributed. One can regard this as a transformed variable of the unknown data outcome at time t for the given design d. Because of its direct link to the probabilities in equation (7.4), the expression for EMMP is equivalent to n univariate integrals [6, 11], one for each of U_i^d, $i = 1, \ldots, n$.

In mathematical terms, the relations in equation (4.22) mean that we have

$$\begin{aligned}
\mathrm{E}[U_i^d \,|\, \mathcal{Y}_{1:t-1}] = \mu_{u_i^d} &= \frac{l - \mathrm{E}[\mu_{t'\,|\,t}^d(i) \,|\, \mathcal{Y}_{1:t-1}]}{\sqrt{\Sigma_{t'\,|\,t}^d(i,i)}} = \frac{l - \mu_{t'\,|\,t-1}(i)}{\sqrt{\Sigma_{t'\,|\,t}^d(i,i)}}, \\
\mathrm{Var}(U_i^d \,|\, \mathcal{Y}_{1:t-1}) = \sigma_{u_i^d}^2 &= \frac{1}{\Sigma_{t'\,|\,t}^d(i,i)} \mathrm{Var}(\mu_{t'\,|\,t}^d(i) \,|\, \mathcal{Y}_{1:t-1}) \\
&= \frac{1}{\Sigma_{t'\,|\,t}^d(i,i)} \boldsymbol{A}^{t'-t}(i,)\boldsymbol{K}_t^d\boldsymbol{Q}_t^d(\boldsymbol{A}^{t'-t}(i,)\boldsymbol{K}_t^d)^T,
\end{aligned} \tag{7.6}$$

where $(i,)$ indicates row i of the matrix. We let $p(u_i^d)$ denote the Gaussian pdf with mean and variance defined in equation (7.6). The EMMP in equation (7.4) is then given by

$$\mathrm{EMMP}_{t'}^d = \frac{1}{n}\sum_{i=1}^{n} \int_{u_i^d} \min\left\{\Phi(u_i^d), 1 - \Phi(u_i^d)\right\} p(u_i^d) du_i^d = \frac{1}{n}\sum_{i=1}^{n} \mathrm{EMP}_{i,t'}^d, \tag{7.7}$$

where $\mathrm{EMP}_{i,t'}^d$ is the expected mis-classification probability in position $\boldsymbol{s}_i$. Moreover, $\Phi(u_i^d) = P(Z \leq u_i^d) = \int_{-\infty}^{u_i^d} p(z)dz$ represents the cumulative distribution function (cdf) of a standard normal variable Z. By symmetry $1 - \Phi(u_i) = \Phi(-u_i)$, and since Φ is monotonically increasing, the integral over u_i can be split in two parts;

$$\mathrm{EMP}_i^d = \int_{-\infty}^{0} \Phi(u_i^d)p(u_i^d)du_i^d + \int_{0}^{\infty} \Phi(-u_i^d)p(u_i^d)du_i^d. \tag{7.8}$$

Defining Z and U_i^d to be independent, so that $p(z)p(u_i^d)$ is their joint density function, we get

$$\int_{-\infty}^{0} \Phi(u_i^d)p(u_i^d)du_i^d = \int_{-\infty}^{0}\int_{-\infty}^{u_i^d} p(z)p(u_i^d)dzdu_i^d = P(Z < U_i^d, U_i^d < 0). \tag{7.9}$$

By the same argument for the second integral in equation (7.8), we have

$$\begin{aligned} \text{EMP}_i^d &= P(Z < U_i^d, U_i^d < 0) + P(Z < -U_i^d, U_i^d > 0) \\ &= P(Z - U_i^d < 0, U_i^d < 0) + P(Z + U_i^d < 0, -U_i^d < 0). \end{aligned} \tag{7.10}$$

The bivariate distributions of Z and U_i^d are used next. For the first term

$$\begin{bmatrix} Z - U_i^d \\ U_i^d \end{bmatrix} = N_2(\boldsymbol{\mu}_i^{\dagger d}, \boldsymbol{\Sigma}_i^{\dagger d}), \quad \boldsymbol{\mu}_i^{\dagger d} = \begin{bmatrix} -\mu_{u_i^d} \\ \mu_{u_i^d} \end{bmatrix}, \quad \boldsymbol{\Sigma}_i^{\dagger d} = \begin{bmatrix} \sigma^2_{u_i^d} + 1 & -\sigma^2_{u_i^d} \\ -\sigma^2_{u_i^d} & \sigma^2_{u_i^d} \end{bmatrix}, \tag{7.11}$$

and a similar expression holds for the second term in equation (7.10). We then get

$$\text{EMP}_i^d = \Phi_2\left(\boldsymbol{\mu}_i^{\dagger d}, \boldsymbol{\Sigma}_i^{\dagger d}\right) + \Phi_2\left(-\boldsymbol{\mu}_i^{\dagger d}, \boldsymbol{\Sigma}_i^{\dagger d}\right), \tag{7.12}$$

where Φ_2 is the bivariate cdf evaluated at $\mathbf{0} = (0, 0)^T$.

7.2 Simulation study

7.2.1 Case description

In this simulation study we mimic a situation with large discharge from location marked 1.2 in Figure 1.4. The outlets of mine tailings happen at depth 20 m. A 2-dimensional regular rectangular spatial grid is formed at this depth for the inner part of the fjord. The domain has $n_e = 44$ grid nodes in the east-west direction and $n_n = 22$ nodes in the north-south direction, so $n = 968$. There are approximately 20 m between each grid node in both directions. In simulations, we use 1 minute time steps in a 30 minute interval of interest, just before low tide.

Table 7.1: Description of the different sampling design strategies. Bottom two rows differ in terms of modeling.

Case	Description
SPDE: EMMP_{t_n}	Minimizing EMMP within local waypoint graph designs and at future time t_n.
SPDE: EMMP_t	Minimizing EMMP within local waypoint graph designs and at current time t.
SPDE: Hybrid	Blend of random transects and SPDE: EMMP_t at time t.
SPDE: Random	Choose randomly within local waypoint graph designs at each time t.
SPDE: EP_t 0.5	Choose local waypoint graph designs with EP closest to 0.5 at current time t.
SPDE: Pre-diag	Sample selected pre-scripted diagonal transects design, with no adaptation.
SPDE: Pre-lawn	Sample along a lawn-mower pre-scripted design, with no adaptation.
AR(1): EMMP_{t_n}	Same as SPDE: EMMP_{t_n}, but with a spatial AR(1) model.
Spatial: EMMP	Same as SPDE: EMMP_t, but with only spatial variability and no time dynamics.

To gain insight in the statistical properties of methods, we use 1000 replicate realizations of the fitted SPDE model, and go through with the presented sampling

strategies (Table 7.1) for each replicate run. We set the measurement error standard deviation to $\tau = 0.316$ log(ppb). At every time step, $m = 1$ data sample is followed by model updating. The ES at time step $t_n = 30$ is of main interest. The critical concentration limit is set to $l = 8.5$ log(ppb), but note that this limit will vary from the operational objective.

7.2.2 Performance measures

The main design criterion is the EMMP, and it is natural to compare results based on the realized MMP. After each replicate run with its sampling path and data $\mathcal{Y}_{1:t_n}$, we hence compute $\frac{1}{n}\sum_{i=1}^{n} \min\{1 - P(X_{t_n}(\boldsymbol{s}_i) > l \,|\, \mathcal{Y}_{1:t_n}), P(X_{tn}(\boldsymbol{s}_i) > l \,|\, \mathcal{Y}_{1:t_n})\}$. Further, actual mis-classification rates for the predictions can be calculated based on the final predictions and the true ES at time t_n. A probability cutoff of 0.5 is used for EP_{t_n}, and the average mis-classification rate for a replicate run is then $\frac{1}{n}\sum_{i=1}^{n} I\left(I(\mathrm{EP}_{t_n}(\boldsymbol{s}_i) \geq 0.5) \neq \mathrm{ES}_{t_n}(\boldsymbol{s}_i)\right)$, where $\mathrm{ES}_{t_n}(\boldsymbol{s}_i)$ is the actual indicator variable of the ES for location $\boldsymbol{s}_i$ at time t_n.

We also compare how well the concentration prediction at time step t_n matches the actual concentration at that time. This is done via the mean squared error (MSE), averaged over all sites and for the 1000 replicates.

The various strategies demand different amounts of calculations. In a real-world operation, the AUV stops to do calculations for a short while at a waypoint, but this time should not be significant compared with the time used between waypoints. We study the approximate computation times for obtaining one sampling path with each strategy using a MacBook Pro 2015 laptop with i5 core. This is not an unrealistic comparison with the computing resources on board the AUV, where the embedded system is operating on a NVIDIA Jetson TX1 single board computer.

7.2.3 Results

We first compare the strategies based on using only the next time step ($t' = t$) and that of always predicting to the end point ($t' = t_n$). We denote results of these two by {SPDE: EMMP_t} and {SPDE: EMMP_{t_n}}, respectively. The second approach which is using the SPDE model all the way to n is more realistic, but the approach is still only myopic in the strategic selection, and there might not be significant gains in the results.

Figure 7.1 displays example sampling paths made by these two different adaptive strategies (t_n middle, t bottom) for two replicates (left, right). The paths are sketched on the final step EPs, which are conditional on all the sampled data in that run. The true ES_{t_n} is also shown (top). In the leftmost replicate, neither {SPDE: EMMP_{t_n}} nor {SPDE: EMMP_t} strategies are able to map all parts of the ES, but they both map the western part well. In the rightmost display they cover a larger part of the domain and predict the true ES more accurately. Display (d) shows that the end strategy maps the northern part well, but misses the south-eastern part. It is the other way around for the strategy only predicting one step (Display (f)).

Results of course vary over replicates. Table 7.2 shows that the mis-classification and MSE measures are about the same for the two methods when we average over

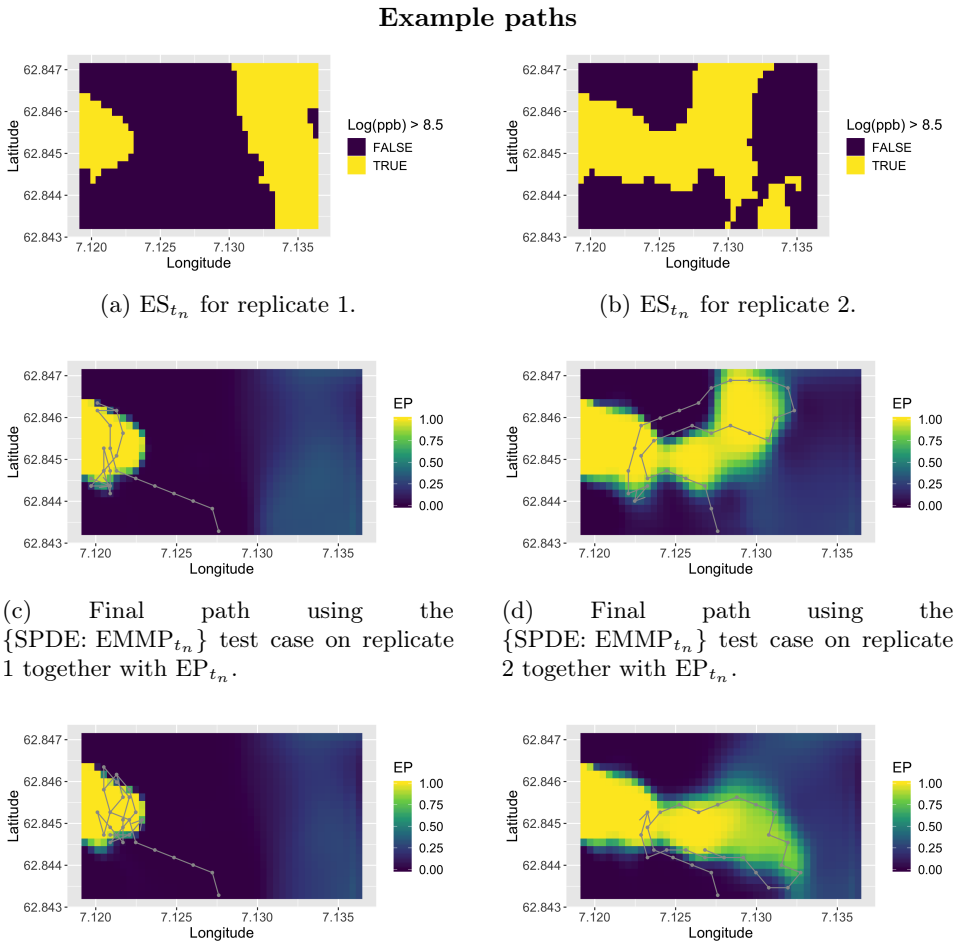

(a) ES_{t_n} for replicate 1.

(b) ES_{t_n} for replicate 2.

(c) Final path using the {SPDE: EMMP_{t_n}} test case on replicate 1 together with EP_{t_n}.

(d) Final path using the {SPDE: EMMP_{t_n}} test case on replicate 2 together with EP_{t_n}.

(e) Final path using the {SPDE: EMMP_t} test case on replicate 1 together with EP_{t_n}.

(f) Final path using the {SPDE: EMMP_t} test case on replicate 2 together with EP_{t_n}.

Figure 7.1: Final simulated AUV paths for two replicates and the two test cases {SPDE: EMMP_{t_n}} and {SPDE: EMMP_t}. The paths are displayed together with the final EPs. The true ES at time step t_n is in the top row.

the 1000 replicates. The slight improvement of using {SPDE: EMMP_{t_n}} seems insignificant, especially so considering the ten-fold increase in computer time when doing the forward prediction in equation (4.22). It hence seems reasonable to use just time t in this kind of adaptive strategies.

Table 7.2: Comparison of different sampling design strategies. Bottom row shows results of the AR(1) and spatial model, all others use the SPDE model.

Test case	Mean MMP	Mean mis-class.rate	Mean MSE	Comp time
SPDE: EMMP_{t_n}	0.104	0.103	0.273	40s
SPDE: EMMP_t	0.103	0.105	0.276	3s
SPDE: Hybrid	0.097	0.099	0.224	4s
SPDE: Random	0.131	0.131	0.316	0.1s
SPDE: EP_t 0.5	0.115	0.119	0.331	2s
SPDE: Pre-diag	0.095	0.097	0.165	-
SPDE: Pre-lawn	0.118	0.119	0.232	-
AR(1): EMMP_{t_n}	0.132	0.135	0.482	8s
Spatial: EMMP	0.112	0.140	0.486	1.5s

As indicated in Figure 7.1, the strategies are sometimes missing parts of the ES when the ES is divided into two or more separate regions. The one step ahead strategies prioritize designs with high immediate reward, in the form of reduced EMMP. With the hybrid strategy the AUV can more easily move across such low-reward domains. Table 7.2 shows that this strategy has somewhat reduced mis-classification rates, at the cost of slightly larger computing time. Because the hybrid strategy tends to explore more of the domain, the MSE gets smaller.

We next compare results with that of simpler strategies choosing the next design at random or via the local waypoint with EP closest to 0.5. Paths for the same replicates are shown in Figure 7.2. The AUV movements are clearly different, but the {SPDE: EP_t 0.5} strategy tries to explore the domain in a similar fashion to the myopic EMMP strategy, without really succeeding to the same extent because there is no expected reduction involved in its computations. Replicate results summarized in Table 7.2 show that the MMPs and MSE are clearly larger for both these strategies.

Now consider the two designs using pre-scripted plans (Figure 7.3). Table 7.2 shows that the lawn-mower design {SPDE: Pre-lawn} gives larger mis-classification rates than strategies {SPDE: EMMP_{t_n}} and {SPDE: EMMP_t}, while using the diagonal design {SPDE: Pre-diag} gives lower mis-classification rates, on par or even better than the adaptive strategies. Guided by preliminary runs, this path is chosen to explore as much of the interesting domain as possible within the time restrictions. Since the ES is often divided into separate parts, which are rarely discovered using the myopic EMMP strategy, the {SPDE: Pre-diag} design has an advantage. The big areas are usually discovered, though some details might

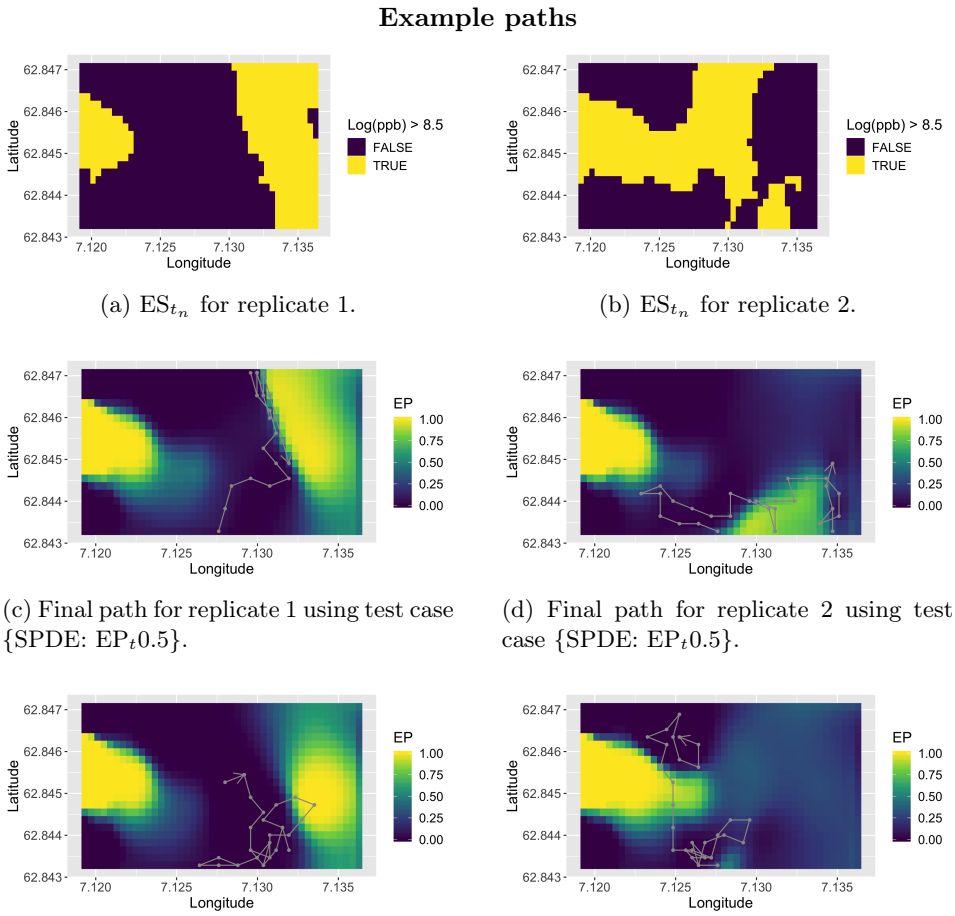

(a) ES_{t_n} for replicate 1.

(b) ES_{t_n} for replicate 2.

(c) Final path for replicate 1 using test case {SPDE: $\mathrm{EP}_t 0.5$}.

(d) Final path for replicate 2 using test case {SPDE: $\mathrm{EP}_t 0.5$}.

(e) Final path for replicate 1 using test case {SPDE: Random}.

(f) Final path for replicate 2 using test case {SPDE: Random}.

Figure 7.2: Final simulated paths for two sampled replicates and the two test cases {SPDE: EP_t 0.5} and {SPDE: Random}. The paths are displayed together with the final EPs. The true ES at time step t_n is in the top row.

be missing, and hence the MSE is small both for {SPDE: Pre-diag} and {SPDE: Pre-lawn}. The EMMP criterion is developed to reduce the probability of mis-classification with respect to ESs, and prediction of concentration at positions where it is certain to be above or below the critical limit of the ES does not help classification. Thus, it is expected that strategies with paths covering more of the domain result in smaller MSEs.

Table 7.2 further shows results of using the EMMP strategies on mis-specified models (AR(1) and spatial model with no temporal dynamical model). The mis-classification rates are clearly larger here, and so are the MSEs, meaning that the strategies now get stuck in regions in space and time that are not really of main interest.

We further tested the strategies under different inputs, in particular the advection strength. When drift speed is low, both {SPDE: Pre-diag} and {SPDE: Hybrid} have a mis-classification rate of 10.7 %. For high advection, the {SPDE: Hybrid} strategy has average mis-classification rate of 9.4 %, which is lower than the 9.6 % of the {SPDE: Pre-diag}. Recall that this pre-scripted path is designed to move across the areas with much prior uncertainty with respect to the reference model. When the advection field is changed, these positions no longer capture the same degree of information. More sensitivity studies are conducted in [19].

7.3 Closing remarks

In this chapter, a second adaptive sampling strategy based on reducing the mis-classification probabilities of the excursions sets of high and low concentration levels has been explored. Simulation results show that a hybrid strategy using a myopic approach combined with a random detour is performing better than naive strategies. Also, the careful spatio-temporal modeling provides more accurate results than simpler spatial or autoregressive models.

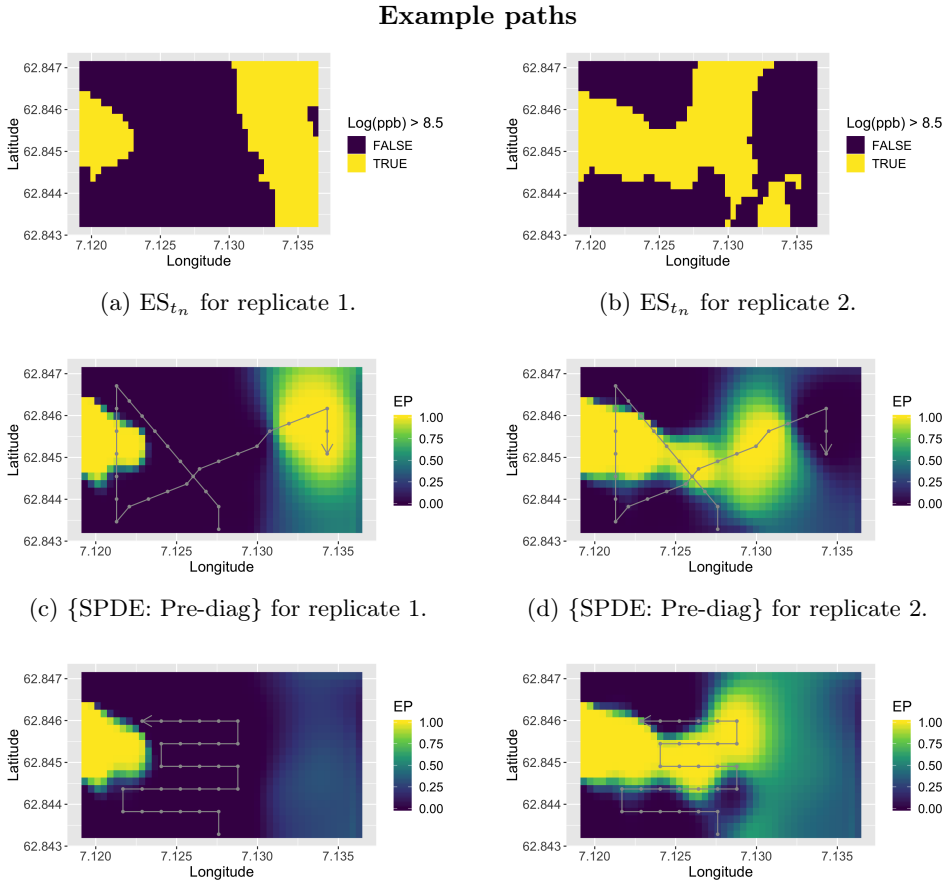

(a) ES_{t_n} for replicate 1.

(b) ES_{t_n} for replicate 2.

(c) {SPDE: Pre-diag} for replicate 1.

(d) {SPDE: Pre-diag} for replicate 2.

(e) {SPDE: Pre-lawn} for replicate 1.

(f) {SPDE: Pre-lawn} for replicate 2.

Figure 7.3: Final simulated paths of {SPDE: Pre-diagonals} and {SPDE: Pre-lawn} for two replicates. The paths are displayed together with the final EPs. The true ES at time step n is in the top row.

Chapter 8

Multiple AUVs

> If you want to do a few small things right, do them yourself. If you want to do great things and make a big impact, learn to delegate.
>
> John C. Maxwell

Until now, the focus has been on adaptive sampling methods using a single AUV. In this chapter, which is based on **paper E**, multiple AUVs are introduced. By utilizing more than one vehicle, it is possible to collect more samples, the field estimation can be done more efficiently, and a larger area can be covered. John C. Maxwell said, "If you want to do a few small things right, do them yourself. If you want to do great things and make a big impact, learn to delegate." Although this quote is about leadership, parallels can be drawn to ocean sampling features. By using multiple vehicles, increased areas can be covered. Furthermore, similar to delegating workforces as a leader, where coordination and clear communication are essential, the same applies to using multiple vehicles efficiently.

According to [52], three main issues underline a multi-robot sampling problem such as this:

1. How can the sampling area be divided efficiently?
2. How can the density distribution be estimated through efficient data fusion when robots collect measurements in parallel?
3. How can the computation and communication burden be distributed efficiently amongst the many robots used?

This chapter suggests solutions to these questions for a multi-robot field estimation problem in communication-constrained environments such as the ocean.

When multiple vehicles are involved in mapping the field of interest, they often operate in some kind of formation [3]. This is explored in [36] which uses a fleet of AUVs where one vehicle is designated as a virtual leader to track the desired predefined path while providing other vehicles with a moving reference. [59] use two AUVs to collaboratively monitor the temperature field (thermocline) to capture the

presence of internal waves where one AUV autonomously trailed the leader AUV. These lead-and-follow behaviors seem especially useful when tracking fronts and for gradient estimation. However, when doing field estimation, exploration of the total area is essential, and we want the AUVs to cover a larger area. Thus, a better idea might be partitioning the sampling area into multiple regions so that each AUV has an assigned region. Another benefit of partitioning is the possibility of computational efficiency. When each AUV has a designated operational area, a smaller model representing only this area can run onboard instead of a complete model. Also, the risk of collision between vehicles is minimal since all vehicles have designated areas.

We aim to divide the sampling area to distribute the sampling-workload of each vehicle evenly. Typically, some regions will be more informative than others, and an objective function is used to evaluate this informativeness at all times during a mission. We use a method based on weighted Voronoi partitions to repeatedly divide the survey area into regions using the objective function as an information criterion. Each AUV is responsible for its own region and performs adaptive sampling within this area. In other words, we focus on a decentralized approach and thus avoid having "a single critical point of failure"; If one vehicle fails, the mission would still be running, and samples would be collected by the remaining vehicles. The use of Voronoi partitions and repartitioning is previously explored in both [35] and [16]. [35] perform repeated weighted Voronoi partitioning based on entropy as the information criterion. The repartitioning is done between all AUVs during a surfacing event. [16] propose a load-balancing algorithm and performs repartitioning when robots are within communication range. In this work, we build on elements from both of these papers. Instead of entropy, we use an objective function incorporating variances and hot-spots as the basis for re-weighted Voronoi partitions. We do the repartitioning only when vehicles are within communication range to avoid waiting time at the surface. When two or more vehicles are within communication range, acoustic communication can be used to trigger a surfacing event. The vehicles share their models and update their onboard field estimates at the surface, given the knowledge retrieved from the other AUV(s). Each AUV runs an onboard spatio-temporal GP model representing the environmental field. In this work, we experiment with different sizes for this proxy model. A full onboard model representing the entire environmental field is the most informative but requires more computing resources than smaller models.

The main novel contributions of this chapter are:

- Propose a repartitioning method based on weighted Voronoi partitions to obtain an even sampling workload for **dynamic** field estimation.
- Formalize how data fusion can be done when sharing GP model data.
- Provide simulation studies showing how the method performs with varying numbers of AUVs and depending on the size of the onboard model.

8.1 Partitioning and sharing

Having defined the individual onboard model for each AUV in the previous chapters, we now connect multiple vehicles. Assume we have k AUVs that all run an

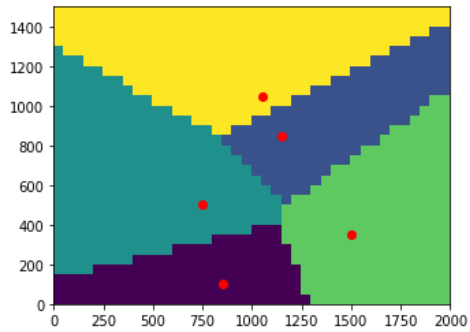

Figure 8.1: Example of Voronoi partitions. The domain $\mathcal{D}$ is divided into 5 regions decided by the seeds shown as red dots. Each region contains all the points which are closer to the region´s seed than to any other seed.

onboard proxy model. The survey area is divided into k regions, and each AUV is designated to its one region. We next describe the details on the partitioning into regions, how the AUVs communicate and share model data. At the start of the mission, an initial partitioning is found via the start location of the AUVs. As the mission proceeds, the regions are repartitioned to even out the sampling workload of the vehicles as the models are updated with observations and through sharing.

8.1.1 Initial partitioning

To divide the survey area into regions, we use Voronoi diagrams. Voronoi partitions are a commonly used approach to separate a space into nonoverlapping regions based on the "nearness" concept [81]. The use of Voronoi partitions is motivated by the speed and range constraints of the AUV. When using the location of the AUVs as the seeds, Voronoi partitions divide the domain into regions so that all the points in one region are closer to the AUV in that region than to any other AUV.

Given our survey area $\mathcal{D}$ and k points in the set of seeds $\mathcal{S} = \{\boldsymbol{s}_1, \ldots, \boldsymbol{s}_k\}$, the Voronoi partition $\mathcal{D}_i$ associated with the point $\boldsymbol{s}_i \in \mathcal{S}$ is defined as

$$\mathcal{D}_i = \{\boldsymbol{s} \in \mathcal{D}; ||\boldsymbol{s} - \boldsymbol{s}_i|| \leq ||\boldsymbol{s} - \boldsymbol{s}_j|| \forall \boldsymbol{s}_j \neq \boldsymbol{s}_i \in \mathcal{S}\}. \tag{8.1}$$

In other words, the partition $\mathcal{D}_i$ contains all the points which are closer to the seed $\boldsymbol{s}_i$ than to any other seed $\boldsymbol{s}_j \in \mathcal{S}$. Figure 8.1 shows an example of Voronoi partitions. Each region $\mathcal{D}_i$ gives a hard constraint on where AUV r_i is allowed to navigate and sample. To find the initial regions, the starting positions of the AUVs $\boldsymbol{s}_r = \{\boldsymbol{s}_{r_1}, \ldots, \boldsymbol{s}_{r_k}\}$ are used as seeds. It is assumed that all the AUVs know the starting positions of each other, and hence know the configuration of the initial Voronoi partitions for the whole survey area $\mathcal{D}$. Figure 8.1 shows an example of an initial partitioning for $k = 5$. The red dots in the display represent the starting positions of the AUVs, and the different regions are represented in different colors.

We extend the notation to clarify that each AUV r_i runs an onboard proxy model as described in Section 2. State variable $\boldsymbol{X}_t^i$ represents the concentration for AUV r_i, where we at time t have $\boldsymbol{X}_t^i|\boldsymbol{Z}_t^i \sim N(\boldsymbol{\mu}_t^i, \boldsymbol{\Sigma}_t^i)$. Here, observation set $\boldsymbol{Z}_t^i = (\boldsymbol{Y}_1^i, \ldots, \boldsymbol{Y}_t^i)$ entails all data gathered or shared with AUV r_i up until time t. When initial partitioning is done, the AUVs initialize the GP model associated with their region; which is all the grid cells in the region $\mathcal{D}_i$ together with the grid cells in a certain radius r_{dist} outside the region (see Figure 8.2a). We denote the set of grid cells in the model of r_i as $\mathcal{D}_{i,r_{\text{dist}}}$. This extra set of grid cells outside the AUVs designated region is added because we consider a dynamic problem and have a temporal model with flow of particles coming from the outside of the regions. In the simulation study we experiment with different values for r_{dist}. An illustration of the boundaries for two AUVs is provided in Figure 8.2.

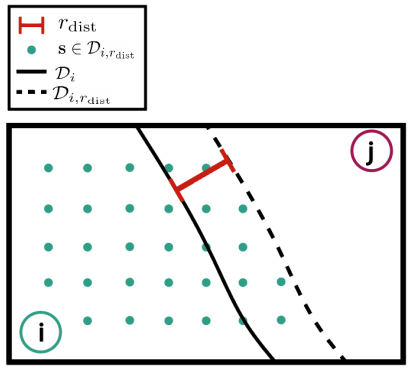

(a) Illustration of the grid cells represented by the onboard model. The figure shows the grid cells as green dots for AUV r_i given r_{dist}.

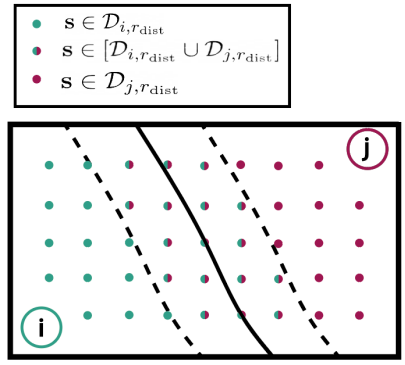

(b) Illustration of the shared grid cells between r_i and r_j (seen as dots with two colors). Only this area is shared and updated when the vehicles surface.

Figure 8.2: Illustration of the operation boundaries and communication range of two AUVs.

8.1.2 Communication

Communication between multiple vehicles is essential, so that they are able to share model data and repartition their regions to obtain an even sampling workload. In practice, there are two methods of communication between AUVs [34].

1. The AUVs come to the surface and share information e.g. using radio communication.
2. The AUVs attempt to share information using acoustic underwater communications.

Acoustic communication requires a short range between the communicating AUVs and can incur quite a bit of loss. Because information is more easily shared and with larger bandwidth at the surface using radio communication, our method only uses acoustic communication to trigger surfacing events. Information sharing

and repartitioning is executed at the surface where the robots can communicate via radio. A surface event is triggered when two or more AUVs are within a predefined communication range C. Denoting the positions of the vehicles at time t as $\boldsymbol{s}_t^{r_1}, \ldots, \boldsymbol{s}_t^{r_{n_{AUV}}}$, the vehicles are within communication range when $|\boldsymbol{s}_t^{r_i} - \boldsymbol{s}_t^{r_j}| < C$, that is when the Euclidian distance between two vehicles r_i and r_j is smaller than the communication range parameter C. When a surfacing event has been triggered because two or more AUVs are within communication range, information is shared between them.

8.1.3 Sharing

In the communications, AUVs can share data or models (mean and covariance). In what follows we focus on sharing the models of the AUVs.

Such sharing is done between two neighbouring AUVs r_i and r_j. Before sharing, AUV r_i has a Gaussian model with probability density $\pi(\boldsymbol{x}_t|\boldsymbol{Z}_t^i)$ while AUV r_j has model $\pi(\boldsymbol{x}_t|\boldsymbol{Z}_t^j)$. They share and update only the parts of the onboard models that are common for both AUVs (see Figure 8.2b.) That is, the part of the models that represent the grid cells in the union $\mathcal{D}_{i,r_{\text{dist}}} \bigcup \mathcal{D}_{j,r_{\text{dist}}}$. Hence, our goal is to find the distribution of $\boldsymbol{X}_t$, given both $\boldsymbol{Z}_t^i$ and $\boldsymbol{Z}_t^j$, with probability density function denoted by $\pi\left(\boldsymbol{x}_t|\boldsymbol{Z}_t^i, \boldsymbol{Z}_t^j\right)$. If there are limitations in the communication capacity, AUVs can share only a subset part of the new partition (See simulation study in Section 8.3).

To simplify the notation, we derive the sharing equations for an r_{dist} much larger than the dimensions of the survey area. In this case, the onboard model on every AUV represent all the grid cells in the survey area $\mathcal{D}_{i,r_{\text{dist}}} = \mathcal{D}_{j,r_{\text{dist}}}$, and we want to find the probability density $\pi(\boldsymbol{x}_t|\boldsymbol{Z}_t^i, \boldsymbol{Z}_t^j)$. We write the (before sharing) conditional mean and covariance for AUV r_i by $\boldsymbol{\mu}_{t|t}^i$ and $\boldsymbol{\Sigma}_{t|t}^i$, and similarly with j superscript for AUV r_j. When ignoring the normalizing constant, the sought density can be found by the following expression:

$$\pi(\boldsymbol{x}_t|\boldsymbol{Z}_t^i, \boldsymbol{Z}_t^j) \propto \pi(\boldsymbol{Z}_t^j|\boldsymbol{x}_t, \boldsymbol{Z}_t^i)\pi(\boldsymbol{x}_t|\boldsymbol{Z}_t^j). \tag{8.2}$$

We now assume that the data $\boldsymbol{Z}_t^j$ is conditionally independent of $\boldsymbol{Z}_t^i$, given $\boldsymbol{x}_t$. This means that $\pi(\boldsymbol{Z}_t^j|\boldsymbol{x}_t, \boldsymbol{Z}_t^i) = \pi(\boldsymbol{Z}_t^j|\boldsymbol{x}_t)$. By using Bayes´ theorem, we then obtain

$$\begin{aligned}
\pi(\boldsymbol{x}_t|\boldsymbol{Z}_t^i, \boldsymbol{Z}_t^j) &= \frac{\pi(\boldsymbol{x}_t|\boldsymbol{Z}_t^i)\pi(\boldsymbol{Z}_t^j|\boldsymbol{x}_t)}{\pi(\boldsymbol{Z}_t^j|\boldsymbol{Z}_t^i)} \\
&\propto \pi(\boldsymbol{x}_t|\boldsymbol{Z}_t^i)\pi(\boldsymbol{Z}_t^j|\boldsymbol{x}_t) \\
&\propto \pi(\boldsymbol{x}_t|\boldsymbol{Z}_t^i)\frac{\pi(\boldsymbol{x}_t|\boldsymbol{Z}_t^j)}{\pi(\boldsymbol{x}_t)},
\end{aligned} \tag{8.3}$$

where we have used that $\pi(\boldsymbol{x}_t|\boldsymbol{Z}_t^j)\pi(\boldsymbol{Z}_t^j) = \pi(\boldsymbol{x}_t)\pi(\boldsymbol{Z}_t^j|\boldsymbol{x}_t)$. All densities in expression (8.3) are Gaussian, so if $\boldsymbol{X}_t \sim N_n(\boldsymbol{\mu}_t, \boldsymbol{\Sigma}_t)$, it takes on the form

$$\pi(\boldsymbol{x}_t) = \frac{1}{(2\pi)^{\frac{n}{2}}|\boldsymbol{\Sigma}_t|^{\frac{1}{2}}} \exp\left(-\frac{1}{2}(\boldsymbol{x}-\boldsymbol{\mu}_t)^T\boldsymbol{\Sigma}_t^{-1}(\boldsymbol{x}-\boldsymbol{\mu}_t)\right)$$
$$\propto \exp\left(-\frac{1}{2}\boldsymbol{x}^T\boldsymbol{\Sigma}_t^{-1}\boldsymbol{x} + \boldsymbol{x}^T\boldsymbol{\Sigma}_t^{-1}\boldsymbol{\mu}_t\right), \tag{8.4}$$

where the last expression represent the canonical form of a Gaussian density with a quadratic part in $\boldsymbol{x}$ and a linear part in $\boldsymbol{x}$.

Now, taking the logarithm and again ignoring the normalizing constant, expression (8.3) becomes

$$\begin{aligned}
&\log(\pi(\boldsymbol{x}_t|\boldsymbol{Z}_t^i, \boldsymbol{Z}_t^j)) \\
&\propto -\frac{1}{2}(\boldsymbol{x}_t - \boldsymbol{\mu}_{t|t}^i)^T[\boldsymbol{\Sigma}_{t|t}^i]^{-1}(\boldsymbol{x}_t - \boldsymbol{\mu}_{t|t}^i) - \frac{1}{2}(\boldsymbol{x}_t - \boldsymbol{\mu}_{t|t}^j)^T[\boldsymbol{\Sigma}_{t|t}^j]^{-1}(\boldsymbol{x}_t - \boldsymbol{\mu}_{t|t}^j)\dots \\
&\quad \cdots + \frac{1}{2}(\boldsymbol{x}_t - \boldsymbol{\mu}_t)^T\boldsymbol{\Sigma}_t^{-1}(\boldsymbol{x}_t - \boldsymbol{\mu}_t) \\
&\propto -\frac{1}{2}\boldsymbol{x}_t^T\left([\boldsymbol{\Sigma}_{t|t}^i]^{-1} + [\boldsymbol{\Sigma}_{t|t}^j]^{-1} - \boldsymbol{\Sigma}_t^{-1}\right)\boldsymbol{x}_t + \boldsymbol{x}_t^T\left([\boldsymbol{\Sigma}_{t|t}^i]^{-1}\boldsymbol{\mu}_{t|t}^i + [\boldsymbol{\Sigma}_{t|t}^j]^{-1}\boldsymbol{\mu}_{t|t}^j - \boldsymbol{\Sigma}_t^{-1}\boldsymbol{\mu}_t\right) \\
&= -\frac{1}{2}\boldsymbol{x}_t^T[\boldsymbol{\Sigma}_{t|t}^{i,j}]^{-1}\boldsymbol{x}_t + \boldsymbol{x}_t^T[\boldsymbol{\Sigma}_{t|t}^{i,j}]^{-1}\boldsymbol{\mu}_{t|t}^{i,j}.
\end{aligned} \tag{8.5}$$

Here, the last expressions are again using the canonical form of the Gaussian density, and equating the quadratic and linear parts of $\boldsymbol{x}_t$ to extract the mean and covariance matrix. From the last transition in equation (8.5) we then see that the probability density of the shared field; $\pi(\boldsymbol{x}_t|\boldsymbol{Z}_t^i, \boldsymbol{Z}_t^j)$, is defined by mean and covariance:

$$\begin{aligned}
\boldsymbol{\Sigma}_{t|t}^{i,j} &= \left([\boldsymbol{\Sigma}_{t|t}^i]^{-1} + [\boldsymbol{\Sigma}_{t|t}^j]^{-1} - \boldsymbol{\Sigma}_t^{-1}\right)^{-1} \\
\boldsymbol{\mu}_{t|t}^{i,j} &= \boldsymbol{\Sigma}_{t|t}^{i,j}\left([\boldsymbol{\Sigma}_{t|t}^i]^{-1}\boldsymbol{\mu}_{t|t}^i + [\boldsymbol{\Sigma}_{t|t}^j]^{-1}\boldsymbol{\mu}_{t|t}^j - \boldsymbol{\Sigma}_t^{-1}\boldsymbol{\mu}_t\right).
\end{aligned} \tag{8.6}$$

8.1.4 Repartitioning

Since the initial regions are decided by the starting positions of the AUVs, it may happen that the sampling workload of the vehicles is unbalanced, that is, some regions may be more information-rich than others. This may also change during the mission because new information is added and because the estimated field is dynamic. The objective function gives us an indication of which sites are more interesting than others at any time t. If the sum of the objective values in a region is high, it means that there is a lot to explore in that area, and there are possibly benefits to gain by sharing some of this workload with an AUV which detects less interesting elements in its subdomain.

We define the sampling workload of AUV r_i at time t, as the objective function summed over all grid cells in the region $\mathcal{D}_i$;

$$O_t^i = \sum_{s\in\mathcal{D}_i} f_t(s). \tag{8.7}$$

If the relative difference between the sampling workloads for two or more neighbouring AUVs is larger than some threshold $\text{Obj}_{\text{thres}}$, i.e.

$$\frac{O_t^i - O_t^j}{O_t^i + O_t^j} > \text{Obj}_{\text{thres}}, \tag{8.8}$$

then the united area between the AUVs r^i and r^j is repartitioned. To find the seeds of the new Voronoi partitions, the center of mass (COM) with regard to the objective function is computed. We denote this as $\boldsymbol{s}_C^i = (s_{C_{\text{east}}}, s_{C_{\text{north}}})$, and it is given by

$$\begin{aligned} s_{C_{\text{east}}}^i &= \frac{\sum_{s \in \mathcal{D}_i} f_t(s) s_e}{\sum_{s \in \mathcal{D}_\setminus} f_t(s)} \\ s_{C_{\text{north}}}^i &= \frac{\sum_{s \in \mathcal{D}_i} f_t(s) s_n}{\sum_{s \in \mathcal{D}_\setminus} f_t(s)}. \end{aligned} \tag{8.9}$$

The repartitioning is done according to Algorithm 2. The repartitioning is done repeatedly until the objective differences are all below the objective threshold or until a maximum number of repartitions is reached.

Algorithm 2 Repartitioning

```
Compute the objective difference (8.8)
while Objective difference >Obj_thres or max iterations is reached do
    for All AUVs at the surface do
        Compute center of mass s_C^i (8.9)
    end for
    Find new Voronoi diagrams using s_C as the new seeds
    Compute objective difference (8.8) given the new regions
end while
```

8.2 Summary of the suggested approach and Algorithm

We provide an overview of the method via pseudocode as in Algorithm 3. At the beginning of a deployment, all k AUVs are positioned in starting locations which are known for all AUVs and the survey area is divided into regions as described in Section 8.1.

The sampling method outlined in Chapter 6 is executed onboard each AUV. This starts out either with the initial Gaussian model or with the latest updated Gaussian model. Then each AUV performs adaptive sampling in its individual domain defined by the previous Voronoi partition. Waypoints are selected repeatedly, in an adaptive manner, and the onboard model of the AUV is updated with new information gathered by that AUV. The updating is done when the waypoint is reached using data from observation taken every 25th meter of the AUV transect.

If two or more AUVs are within communication range and the time since these vehicles previously shared information is longer than a specified time threshold,

a surface event is triggered. The vehicles within communication range will then surface and share information as described in Section 8.1. After information is shared, the AUVs check if the sampling workload is uneven. If this is the case, they repartition their unified area as detailed in Section 8.1.4.

Algorithm 3 Multi-Robot Adaptive Sampling method

```
Initialize GP model
while running do
    For each of the AUVs
    Select new waypoint using (6.1)
    Travel to new waypoint and collect observations
    if waypoint is reached then
        Update GP model with observations according to (4.22)
        if vehicles are within communication range then
            if time since previous surface event > time threshold then
                For communicating subset of the AUVs
                Go to surface
                Share information and update onboard field predictions according
to (8.6)
                Compute workload (8.7)
                if Workload is unbalanced (8.8) then
                    Repartition according to Algorithm 2
                end if
            end if
        end if
    end if
end while
```

8.3 Simulation study

To simulate the particle fields in a coastal area, we define test scenarios using a spatial $1000 \times 750\text{m}^2$ grid with 25 meters spacing. We use two test scenarios to evaluate the performance of the method. The first scenario is static, so no dynamical models (ocean currents) are included. The second case includes dynamical elements with a particle field evolving in the spatial domain over a 5-hour period.

For each of the scenarios, we run 50 replicates using randomized starting positions for the AUVs. We perform the study with the number of AUVs ranging from 1 to 5. For each case of scenario, replicate starting position and number of AUVs, and compare 4 different strategies. Each case is run for the same amount of time and a surfacing event is set to last for 2.5 minutes.

An overview of the strategies can be seen in Table 8.1. The Voronoi-constant strategy does not perform any repartitioning or sharing. The other three strategies perform sharing and repartitioning during the mission, but the size of the onboard model and the size of the shared model data varies. Voronoi-full includes the entire model onboard every AUV, and full model sharing is performed. Voronoi-100 and

Table 8.1: Overview of the different strategies tested in the simulation study.

Strategy	Regions	Model	Sharing
Voronoi-constant	Constant	Full	Full model
Voronoi-full	Repartitioned	Full	Full model
Voronoi-100	Repartitioned	$r_{\text{dist}} = 100$ m	$r_{\text{dist}} = 100$ m
Voronoi-200	Repartitioned	$r_{\text{dist}} = 200$ m	$r_{\text{dist}} = 200$ m

Voronoi-200 run local onboard models with an addition of 100 and 200 metres boundary ($r_{\text{dist}} = 100$ m and $r_{\text{dist}} = 200$ m).

8.3.1 Static scenario

The true static field can be seen in Figure 8.3. In this scenario, the AUVs start the mission with no prior knowledge. The prior model of particles distribution has mean $\mu_0 = 5$ log (ppb), standard deviation $\sigma_0 = 1.7$ and a Matern (3/2) correlation kernel decay parameter $\phi = 0.02$.

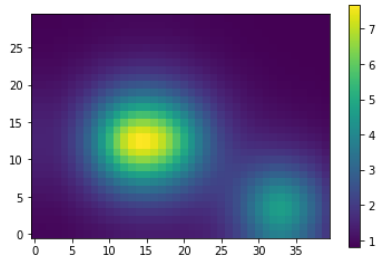

Figure 8.3: Test case 1: True stationary particle field.

8.3.2 Dynamic scenario

The dynamical situation is characterized by the particle field evolving over 5 hours. The field is initiated with the stationary field from the static scenario. Here, the dynamical model parameters are trained from ocean current data available from the ocean model SINMOD [74]. This means that some of the model parameters are trained, and in doing so we get input to the temporal onboard proxy model. Further, atmospheric forcing for daily forecast simulations were obtained from NOAA's Global Forecast System with 0.5 degree resolution (for large scale model domains) and from the Norwegian Meteorological Institute's MetCoOp Ensemble Prediction System with 2.5 km resolution (for local model domains).

Figure 8.4 shows the true field in the dynamical case. The advection vector varies with time; first flowing towards south-east (0-2 hours), then flowing mainly

towards north(2-4 hours), and lastly towards west (4-5 hours). There is clearly diffusion which is damping the high concentration levels. After 4 hours there are a large concentration of particles coming from outside the eastern part of the survey area. This is modeled using Dirichlet boundary condition on the eastern boundary. The Dirichlet boundary values are given as a priori knowledge in the models.

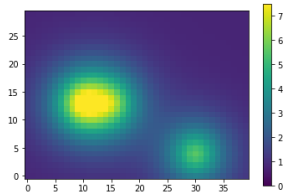

(a) Distribution after 0 hours.

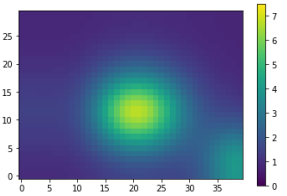

(b) Distribution after 1 hours.

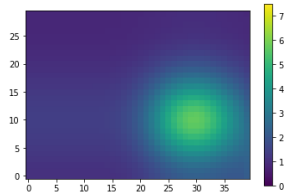

(c) Distribution after 2 hours.

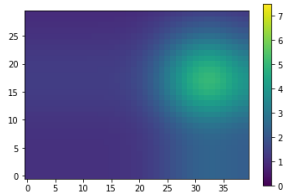

(d) Distribution after 3 hours.

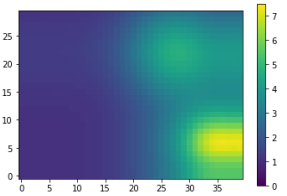

(e) Distribution after 4 hours.

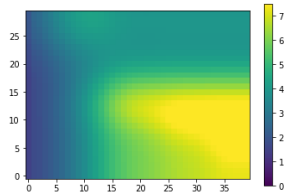

(f) Distribution after 5 hours.

Figure 8.4: Test case 2: True dynamic particle field evolving over a time period of 10 hours.

8.3.3 Results

In this section, we present the results obtained by our proposed strategies for the two test scenarios. The section is divided into four parts, each discussing the results for one performance measure.

Root mean square error (RMSE) is a standard metric to evaluate the performance of regression models. In our cases, the value indicates how well our method predicts the underlying field. We compute the RMSE at the end-time of each run, and the results for both test cases can be seen in Figure 8.5.

Mean standard Deviation (MSD) is computed as the mean standard deviation in the GP models over all the grid cells at the end-time of the mission. Results can be seen in Figure 8.6.

Mean objective (MO) is the averaged objective value (6.1) over all grid cells at the end of the mission. Results at the end-time of the mission are shown in Figure 8.7

Number of surface events is a measure on how many times the vehicles surface and share model data during one hour of the mission. Every time a surfacing event is triggered, this value increases by one. The histogram in Figure 8.8 shows the number of surfacing events during the second hour of the mission for the 50 replicate runs.

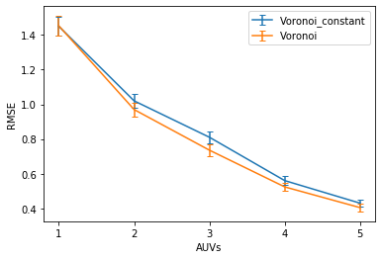

(a) Static scenario.

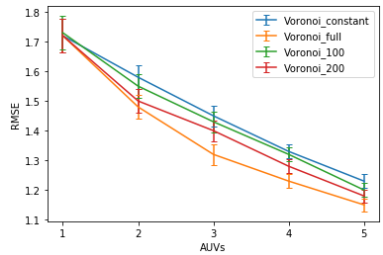

(b) Dynamic scenario.

Figure 8.5: RMSE for both test scenarios with error bars showing one standard error among the 50 replicate runs.

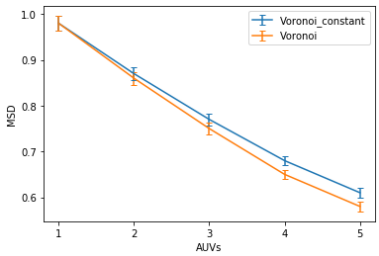

(a) Static scenario.

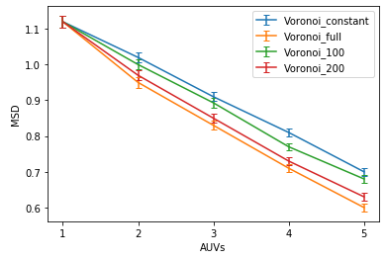

(b) Dynamic scenario.

Figure 8.6: MSD for both test scenario with error bars showing one standard error among the 50 replicate runs.

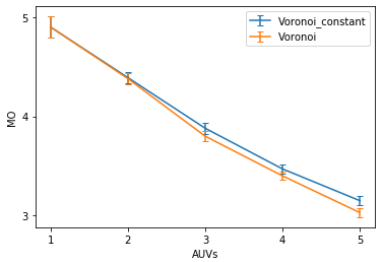

(a) Static scenario.

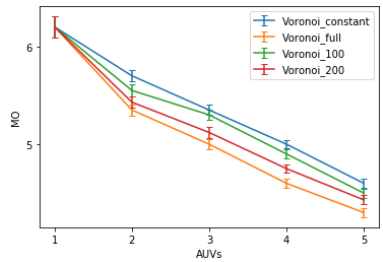

(b) Dynamic scenario.

Figure 8.7: MO for both test scenarios with error bars showing one standard error among the 50 replicate runs.

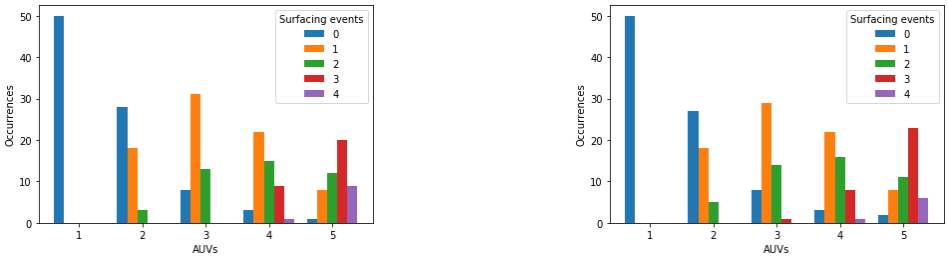

(a) Static scenario.

(b) Dynamic scenario.

Figure 8.8: Number of surfacing events during one hour for the 50 replicate runs.

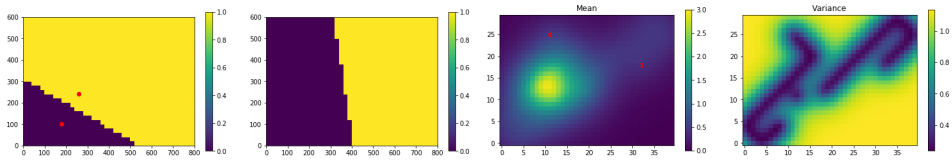

(a) The initial partitions and initial start positions.

(b) The partitions at the end of the mission.

(c) The estimated field at the end of the mission.

(d) The variance at the end of the mission.

Figure 8.9: Example mission from the static scenario with two vehicles.

Finally, we consider the *computation time* for the different strategies. Table 8.2 shows the computation time of simulating one single AUV when running a mission including 4 AUVs in total. We show the mean computation time for one hour of simulation for the 50 replicate runs. This time includes updating of the model, data sharing and repartitioning. A MacBook Pro 2017 laptop with i5 core was used in the simulation.

Table 8.2: Computation time of simulation one single AUV for the different strategies when running a mission including 4 AUVs. The computation time shown is the time taken to simulate 1 hour of the different strategies.

Strategy	Computation time (s)
Voronoi-constant	56
Voronoi-full	188
Voronoi-100	75
Voronoi-200	87

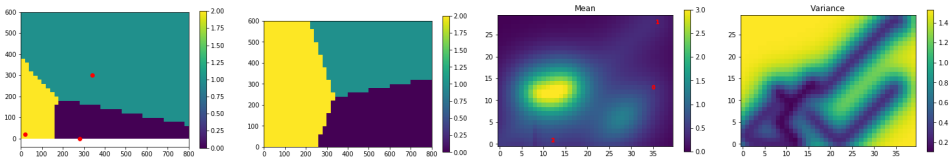

(a) The initial partitions and initial start positions.
(b) The partitions at the end of the mission.
(c) The estimated field at the end of the mission.
(d) The variance at the end of the mission.

Figure 8.10: Example mission from the static scenario with three vehicles.

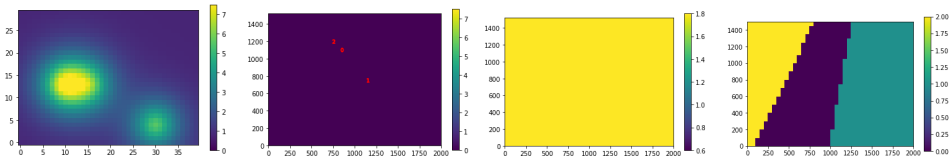

(a) The initial true field.
(b) Initial predicted field $\boldsymbol{\mu}_0$
(c) The initial standard deviation.
(d) The initial regions.

Figure 8.11: Initial distribution for the dynamic example.

Figure 8.9 and 8.10 show selected results of the field estimation for the static scenario using two and three AUVs. The initial Voronoi partitions are plotted in displays a) and the partitions at the end of the missions are plotted in b). In displays c) and d) we show the field mean and variance, respectively.

In Figure 8.12 selected steps from the first hours of the dynamic scenario are presented, for a mission with three AUVs. The initial starting distribution and regions can be seen in Figure 8.11.

8.4 Discussion

We share some of the key insights from the example cases.

From Figure 8.5 we see that having more vehicles reduce the error. For the static scenario, the reduction in error seems to decay after 3 AUVs. This is due to the size of the survey area. Both 4 and 5 AUVs seem to cover much of the area. On the other hand, we do not observe the same effect for the dynamic case, where the field changes with time. For this scenario, the error reduction is quite large also when adding a 4th and 5th AUV. From this RMSE-figure, we further see that repartitioning gives a better field estimate than having no repartitioning. This is the case for both scenarios; we see that all the Voronoi methods using repartitioning give significantly smaller errors than "Voronoi-constant". Having a larger model (larger value of r_{dist}), clearly improve the results for the dynamic scenario.

Considering the MSD in Figure 8.6 it can again be seen that the number of AUVs has a decreasing effect on the standard deviation. This is as expected since more vehicles leads to more samples and hence lower variance. The Voronoi repartitioning methods substantially reduce the MSD, and the full model sharing gives the best

Sampling and sharing after 22 minutes.

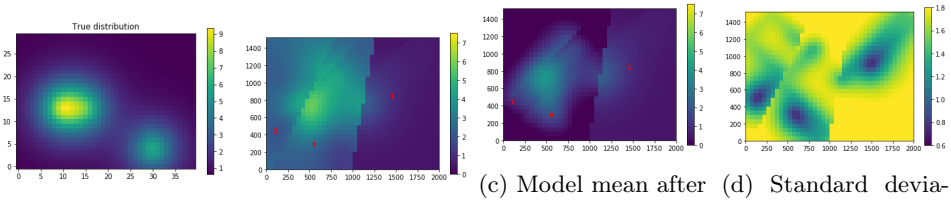

(a) True field. (b) Model mean. (c) Model mean after sharing. (d) Standard deviation.

Repartitioning after 22 minutes.

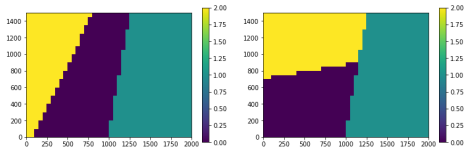

(e) Regions before repartitioning. (f) Regions after repartitioning.

Sampling and sharing after 1 hour and 13 minutes.

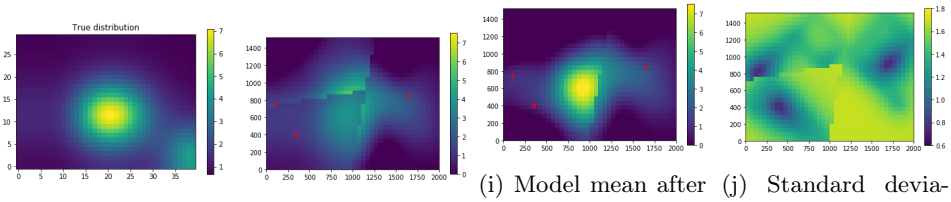

(g) True field. (h) Model mean. (i) Model mean after sharing. (j) Standard deviation.

Repartitioning after 1 hour and 13 minutes.

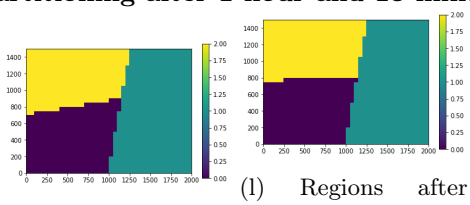

(k) Regions before. (l) Regions after repartitioning.

Sampling and sharing after 2 hours and 2 minutes.

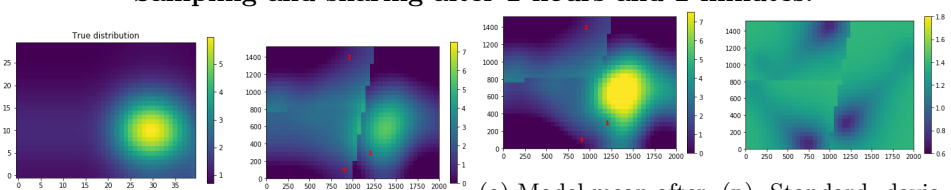

(m) True field. (n) Model mean. (o) Model mean after sharing. (p) Standard deviation.

Repartitioning after 2 hours and 2 minutes.

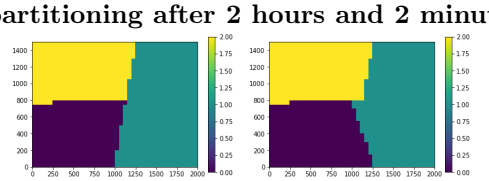

(q) Regions before. (r) Regions after.

Figure 8.12: Example mission from the dynamic scenario using three vehicles.

results. The MO metric, which is a linear combination of MSD and the predicted mean, show similar behavior to the MSD and RMSE, which is as expected.

Figure 8.8 shows that the number of surfacing events increases with the number of AUVs in the mission. Because the same communication range (C = 200 meters) is used for all numbers of AUVs, they are more likely to be within communication range with other vehicles when more vehicle are in the survey area. The difference between the static and the dynamic case when it comes to surfacing events seem to be negligible.

The running time of the onboard model and the sharing and repartitioning are presented in Table 8.2. The running time of the onboard model increases when a temporal model is included. This can be seen in the difference between the static and the dynamic scenario. Also, using larger individual onboard models (larger values of r_{dist}) increase the running time significantly. We observe that the Voronoi-100 and Voronoi-200 use less time than Voronoi-full. Thus, the balance between performance and running time must be evaluated and r_{dist} should be selected wisely depending on the desired performance, the size of the total area and the computer resources onboard.

Figure 8.12 shows results at selected time steps for a dynamic scenario using three vehicles and the Voronoi-full strategy. This example illustrates the steps of the adaptive sampling method. The initial distribution before sampling starts is in Figure 8.11. After 22 minutes we obtain communication range between two vehicles. First mode data is shared, and then the regions are repartitioned. This is repeated after 1 hour and 13 minutes, and we obtain a slight adjustment of the regions. After 2 hours and 2 minutes two vehicles are again within communication range. The standard deviation plots show decreasing values, and the values are especially low close to the AUVs' positions at the current time. Each repartitioning seems to even out the area between the AUVs, and when sharing is done, we observe that the field estimate becomes much smoother at the border between the sharing vehicles.

Note that the methods are using the same current field, both for building the dynamic scenario and in the simulation study. In reality the ocean current estimates will be uncertain and this is a source of error that has not been considered in this work.

8.5 Closing remarks

In this chapter, adaptive sampling using multiple AUVs has been explored. Weighted Voronoi partitions are used to find suitable regions for each AUV, with the goal of obtaining an even sampling workload between the vehicles. Results from simulations have shown that adding extra vehicles and performing control coordination and sharing between them gives an improved prediction of the underlying field. By repeatedly repartitioning the sampling regions we obtain a better result compared to using static regions.

Part III

Field Experiments

Chapter 9

Experimental AUV and implementation

In this third part of the thesis, the focus is on the field experiments in Frænfjorden. This chapter introduces the robotic platform used during the AUV missions. Technical details of the robotic platform are presented, and a description of the implementation of the adaptive sampling framework are given.

9.1 L-AUV Harald

The robotic platform in our experiments consisted of a Light AUV from OceanScan (see Figure 9.1). Some technical specifications are summarized in Table 9.1. The L-AUV has various physical and environmental sensors (see Table 9.2). This L-AUV is typically used to collect information for oceanographers, biologists, and others interested in the physical and chemical properties of the water column. Real-time information is transmitted through a wireless ethernet network when on the surface through the Manta modem. Underwater the Manta communicates through an Evologics USBL communication system.

During the field experiments, the robot often operated without bottom-track.

Specification	
Vehicle length	240 cm
Weight in air	32.1 kg
Max operational depth	100 m
Speed	0.5 - 2 m/s

Table 9.1: Technical specifications of L-AUV Harald.

Figure 9.1: The light AUV (Harald) produced by OceanScan was used in the field experiments.

Sensors	Type
Main CPU	AMD Geode LX 800 CPU
IMU	Microstrain 3DM-GX4-25
CTD	SeaBird SBE 49 FastCAT
Dissolved Oxygen	Aanderaa Optode 4831F
FLuorometer	WetLabs EcoPuck Triplet

Table 9.2: Description of the sensors onboard L-AUV Harald.

This impacts the accuracy of its navigation precision; hence, frequent surfacing was implemented in the mission procedures.

The L-AUV is equipped with a Wetlabs EcoPuck sensor measuring total suspended matter (TSM), a measure of optical back-scattering in the form of an attenuation coefficient. The measured sensor values of total suspended matter (TSM) are an indication of turbidity, and this observation value was used for the assimilation and updating of the GP model. It was converted to a measure of (log) concentration to adjust the value to our onboard model. This conversion is not straightforward. Before every mission, a small test run was executed, mapping the corners of the survey area. During this test run the conversion from the measured TSM value was decided, by comparing the measured sensors values to the predicted DREAM concentrations at the time. We also need to determine the uncertainty τ. The Wetlabs EcoPuck sensor user manual suggests an attenuation error of about 4% at attenuation coefficient 1 m^{-1}. With concentrations varying between approximately 3 and 8 log(ppb), assuming measurement standard deviation of 4% gives τ between 0.12 and 0.32 log(ppb). However, both navigation errors and vehicle drift can lead to uncertainty in the sampling location. Hence, we set $\tau = 0.5$ log(ppb)

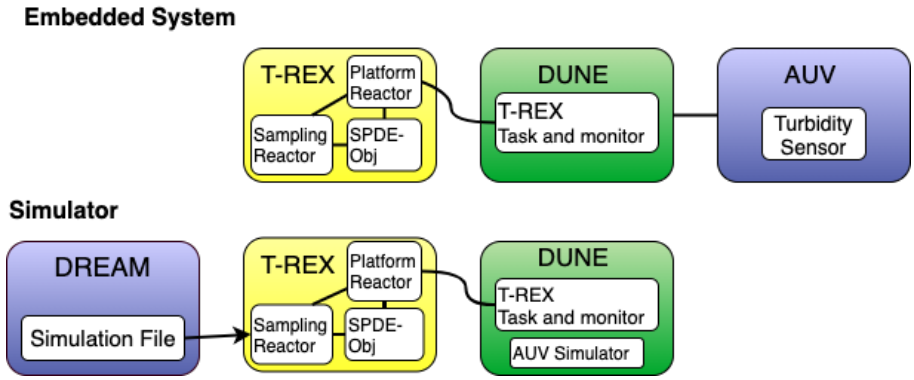

Figure 9.2: The architecture of the embedded system and the simulator. The Unified Navigation Environment (DUNE) runs onboard the AUV, and the agent architecture T-REX sits on top of this, allowing the embedding of multiple decision processes such as planning.

for the experiments.

9.2 Implementation

Figure 9.2 shows the layout of the agent architecture used in the experimental survey. The Unified Navigation Environment (DUNE) [60] runs onboard the AUV and is used for control, navigation, vehicle supervision, communication, and interaction with actuators. On top of this sits the agent architecture T-REX (Teleo-Reactive EXecutive) [64], which enables an adaptive mission. T-REX allows the embedding of multiple complex decision processes (including planning). The communication between DUNE and T-REX was handled by the LSTS toolchain [61], which provides the back-seat driver API to DUNE. This allows external controllers, such as T-REX, to provide desired tasks for our platform while also receiving progress updates on the current state. The various sampling algorithms described in the previous chapters were written as python scripts and were implemented as a reactor in the T-REX framework. A reactor is a component of T-REX acting as an internal control loop and is capable of producing goals that the planner integrates into a series of actions (e.g., Goto and Arrive_at). The set of all those actions forms a plan which was built while ensuring operational constraints of the mission (e.g., the vehicle should never dive deeper than a certain depth or leave a defined area.) The plan is then sent to DUNE, which handles low-level control and execution.

Before deploying the AUV, the integration on the L-AUV was tested in a simulated environment as similar as possible to our embedded system. In simulations, sensor readings from the AUV were replaced with data from SINMOD and DREAM, and an AUV simulator in DUNE was used to simulate the behavior of the AUV. The layout of the simulator is shown in Figure 9.2.

Chapter 10

Field Experiments

> Anything that can go wrong will go wrong.
>
> *Murphy*

New challenges will arise when stepping from simulation studies to the actual field. Murphy's law states: "Anything that can go wrong will go wrong." In our case, things working in theory and simulation may not always function well in real-life. Hence, field experiments are essential and will provide helpful insight into how well the adaptive sampling methods perform in real-life.

In this chapter, results from three field experiments are presented. All of the experiments are executed near the seafill in Frænfjorden. The first field experiment was conducted in October 2018, and a static case similar to the static simulation study in Chapter 6 was tested. Two field expeditions were done during 2020, where the full spatio-temporal model was used with two different sampling strategies (the objective function from Chapter 6 and the sampling strategy detecting excursion sets as described in Chapter 7). Table 10.1 gives an overview of the fieldwork dates, which method was tested, and from which paper the results are.

10.1 Static case

The static experiment was carried out on October 19th, 2018, in Frænfjorden, Norway. Figure 10.1 shows the chosen operational area together with the executed

Method	Date	Model	Sampling strategy	Paper
Static	October 19th 2018	Spatial	Objective	Paper B
Dynamic	December 17th 2020	Spatio-temporal	Objective	Paper C
Excursion sets	September 17th 2020	Spatio-temporal	Excursion	Paper D

Table 10.1: Overview of the fieldwork presented in this thesis, showing the dates, which sampling strategy was used, and from which paper the results are collected.

adaptive AUV path. The location of the outlet and a stationary buoy equipped with a CTD sensor and a turbidity sensor is also marked in the figure.

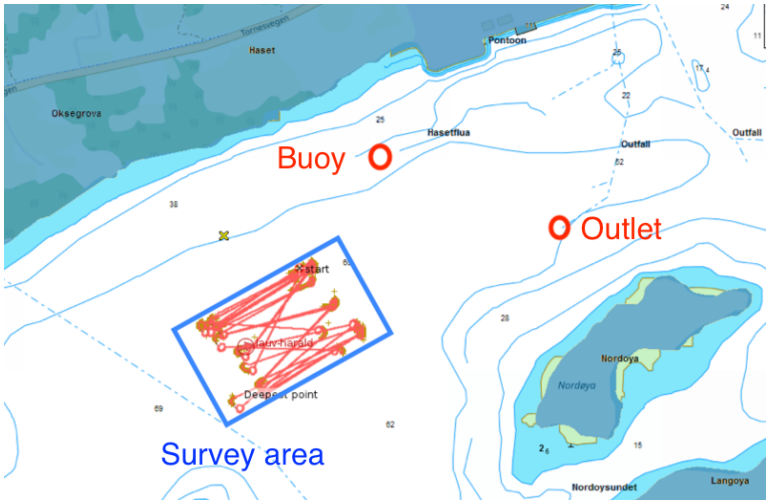

Figure 10.1: Map of the chosen operational area. The location of the stationary buoy and the outlet is marked in red in the figure. The path of the AUV is drawn as a red line inside the survey area which is marked as a blue rectangle.

10.1.1 Experimental setup

Frænfjorden is a fjord with shallow water, fishing nets, and boat traffic and is, therefore, a risky place for an AUV mission. This led to limitations when choosing the operational area. Considering the risk and assuring that the survey area was fairly close to the outlet of particles, we ended up with a fairly small area (550 m $\times$ 250 m) shown in Figure 10.1. The waypoint grid was chosen inside this area so that the AUV would not operate outside. A drifting margin of 50 m was allowed. The grid cell size was set to 32 $\times$ 32 meters, and the parameters constraining the travel length of the AUV (see equation (6.1)) was set to $d_{\min} = 250$ m and $d_{\max} = 400$ m.

The depth layer used in the mission (approximately 22-27 meters depth) was chosen as the layer with the most variation in the simulation data from DREAM. A mission was run for 110 minutes, starting at 8 am on October 19th, 2018.

In order to avoid vehicle drift outside of the safe operation area, the AUV surfaced every time it reached a waypoint. When diving, the AUV followed a Yoyo path which can be seen in Figure 10.2 showing the path in depth direction for the first 20 minutes of the mission. The sensor value used in the algorithm was chosen as the maximum TSM value in a span of 10 seconds near the waypoint.

10.1.2 Results and evaluation

This section presents the results related to the proposed adaptive sampling method. Figure 10.3 shows the prior mean, the prior standard deviation, and the prior

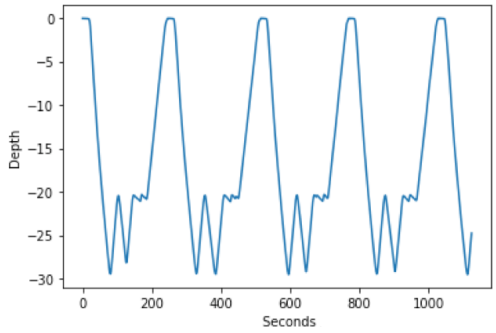

Figure 10.2: Plot showing the yoyo path in the depth direction of the AUV for the first 20 minutes of the survey.

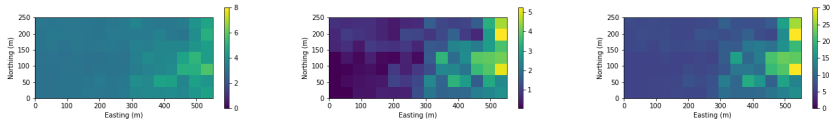

(a) Prior mean. (b) Prior standard deviation. (c) Prior objective

Figure 10.3: The initial state for the survey area. Showing the prior mean $\boldsymbol{\mu}_0$, the prior standard deviation $\boldsymbol{\sigma}_0$ and the prior objective values in each grid cell.

objective function. This was found using the empirical mean and variance from the DREAM data in the area, as explained in chapter 5.

Figure 10.4 shows the updated state at selected time steps during the mission. The estimated mean, the model variance, and the objective function is plotted together with a red line showing the path of the AUV for the last five waypoints. The sampling locations are shown as red dots, where the largest disk represents the most recent sampling location.

It can be seen that the AUV chooses sampling locations according to the objective function but also takes into account the travel length criteria. The western region of the survey area is never explored due to its low objective value. This region is far from the outlet of particles, and the model data from DREAM shows both low variance and low concentrations in this area. Thus, this is, by our model, considered a less interesting area to sample. However, since our model increases the variance with time in unsampled sites, there is reason to believe that this area would have been explored if the mission had run longer.

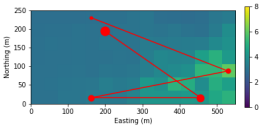

(a) Estimated mean at t = 30 min.

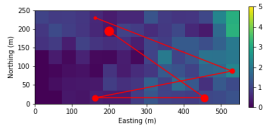

(b) Standard deviation at t = 30 min.

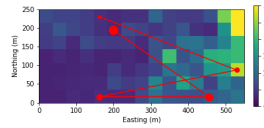

(c) Objective function at t=30 min.

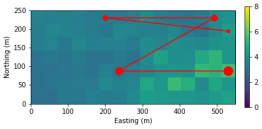

(d) Estimated mean at t = 50 min.

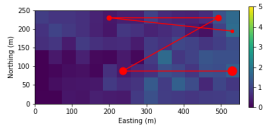

(e) Standard deviation at t = 50 min.

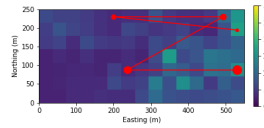

(f) Objective function at t = 50 min.

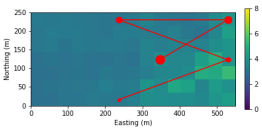

(g) Estimated mean at t = 70 min.

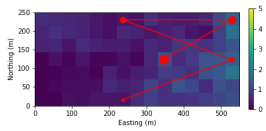

(h) Standard deviation at t = 70 min.

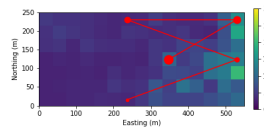

(i) Objective function at t=70 min.

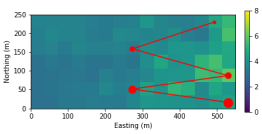

(j) Estimated mean at t = 90 min.

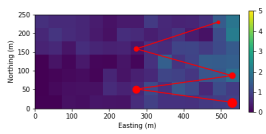

(k) Standard deviation at t = 90 min.

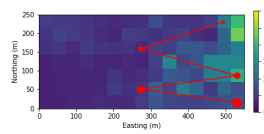

(l) Objective function at t=90 min.

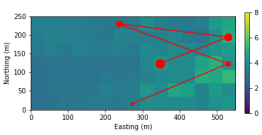

(m) Estimated mean at t = 110 min.

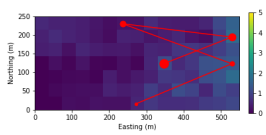

(n) Standard deviation at t = 110 min.

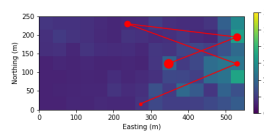

(o) Objective function at t = 110 min.

Figure 10.4: Updated state at selected time steps during the mission. The estimated mean, the model standard deviation, and the objective function is plotted together with a red line showing the path of the AUV for the last five waypoints.

At the end of the mission, the variance in our GP model is highly reduced compared to the prior variance. This indicates that the sampling algorithm works according to the model. The predicted mean particle concentration is generally higher near the outlet of particles, which is what we expected from theory and our numerical model DREAM.

10.1.3 Buoy data and tidal effects

To better understand the area and the ground truth at the time of the experiment, data from other marine platforms are considered. The fjord also has a moored buoy equipped with a turbidity sensor. The buoy is located about 200 m from the survey area (see Figure 10.1). Data from the buoy is presented in Figure 10.5b, which shows the turbidity data for the whole day of the mission. A plot of the tidal effects of the same day is included in Figure 10.5a. Comparing the turbidity data with the tidal effects, it can be seen that the turbidity measurements seem to be the highest close to a tidal low. During a tidal low, the water flows westward, out of the fjord. Because the outlet lies to the east of the buoy, this is when the highest concentration of particles is transported towards the buoy. The differences between the measured turbidity values are quite significant depending on where in the tidal cycle we are, indicating that the tidal effect highly affects the transportation of particles in the fjord. Thus, adding this effect to our onboard model would likely lead to an improvement. This is the motivation for the field experiment presented in the next section.

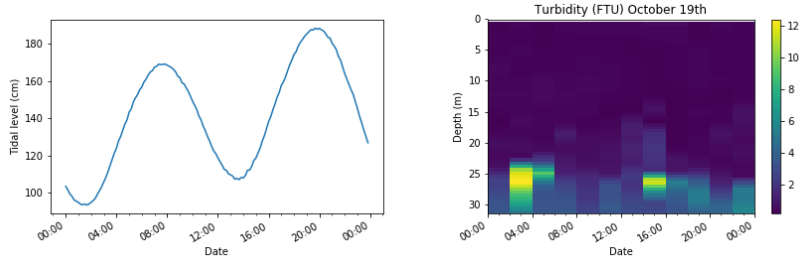

(a) Tidal levels on the day of the survey. (b) Turbidity measurements from the day of the survey.

Figure 10.5: Tidal levels and turbidity measurements from the moored buoy on the day of the experiments.

To sum up, the field trial from the static scenario shows that the variance in the model is reduced and that the locations are chosen according to the objective function. The sampling seems to cover the area such that more samples are collected near the outlet than further away from the outlet. Verification of the predicted particle distribution is hard since there is no easy way to know the ground truth. Still, the trends are as expected from common sense and from the numerical ocean and particle transportation models.

10.2 Dynamic scenario

The field experiments testing the dynamic scenario was in December 2020. Two missions were carried out on two consecutive days, December 17th and 18th, 2020, testing the dynamic scenario (as in 6.4). The operational discharge outlet at the time of the experiments is marked as 2.1 in Figure 10.6, and a rectangular operational area of size 1150 m × 250 m (also marked in the figure) was used. Again, we focus on the depth layer at around 22-25 meters since this is a layer with a lot of variation and a layer where we, according to the DREAM and SINMOD models, will find a lot of mine tailings. This is verified by our sensor data as well. Figure 10.7 shows one transect (waypoint-to-waypoint) for the AUV including sensor data values. It is clear from the figure that a layer with increased turbidity is reached.

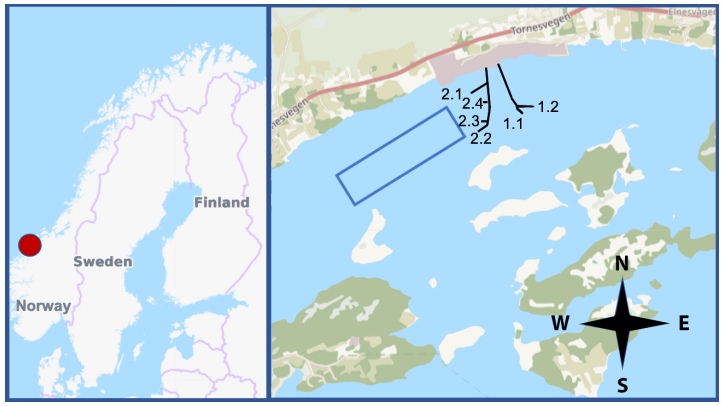

Figure 10.6: The location of Frænfjorden and the factory Omya Hustadmarmor AS. The black lines represent the pipes where mine tailings are let out, and the numbers represent possible outlets. The factory is marked in pink in the figure. The survey area of size 1150 m × 250 m is marked as a blue rectangle and is located on the south-west of the outlets.

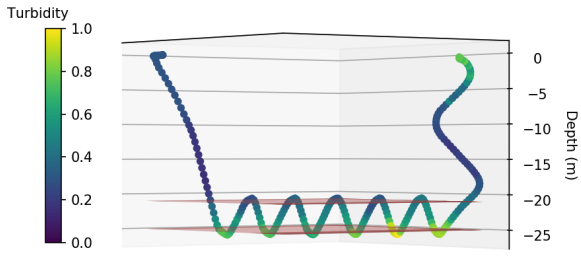

Figure 10.7: Showing the AUV transect from waypoint to waypoint. The color of the transect indicates normalized mine tailings concentration values, and the two red surfaces show the depth layer (22-25 meters) where samples are collected.

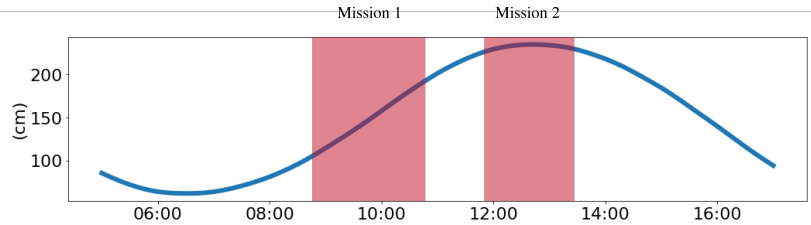

Figure 10.8: The blue line shows the tidal cycle on December 17th. The red boxes indicate the time intervals for the two missions.

10.2.1 AUV path

Inside the operational area, a 2-dimensional grid of size 57×12 was defined, giving $N = 684$. The distance between each node was approximately 20 m in both grid directions, and each grid point was a possible waypoint for the AUV. The AUV was set to surface whenever reaching a new waypoint to reduce the uncertainty caused by navigation errors and vehicle drift and for safety reasons. The AUV did a yoyo maneuver between 20 and 26 meters between each waypoint. Figure 10.7 shows one transect (waypoint-to-waypoint) from our survey, starting with a dive until reaching the selected depth layer, doing the yoyo maneuver, and then surfacing in a corkscrew maneuver. The corkscrew maneuver was chosen to obtain a sampling value as close as possible to the waypoint. The sensor reading used for updating the model was chosen as the maximum value in the layer 22-25 meters (the layer marked with red surfaces) for each of the separate yoyos. For the transect in Figure 10.7, this would result in 6 updating values. Because the transect length could vary for different waypoints, the number of yoyos was not fixed but mostly alternated between 5 or 6 yoyos per transect, giving 5 or 6 updating values per transect.

10.2.2 Results

The survey area is located near the coast in a fjord arm, so the currents are highly influenced by the tidal cycle. To get a better insight into how the ocean currents behave at the time of the missions, we consider the tidal cycle at the time in Figure 10.8. Our temporal model considers the tides' variations, and we choose to focus on two missions occurring at different intervals in the tidal cycle. The first mission is before a tidal high, and the second is when the tides turn at the top. The period of the two missions is marked in red in the figure. Hourly predicted ocean currents between 09:00 and 13:00 from the SINMOD model could be seen in Figure 10.9. As expected, the currents are highly influenced by the tides showing an inward flow (eastward) before the tidal high (09:00-11:00) and weaker ocean currents during the tidal high (11:00-13:00). These predictions are used as input to our onboard model as the forcing in the SPDE model.

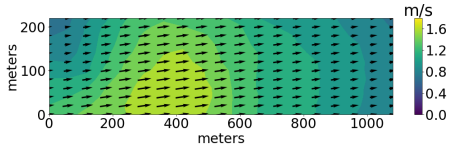

(a) Current data from SINMOD for 09:00.

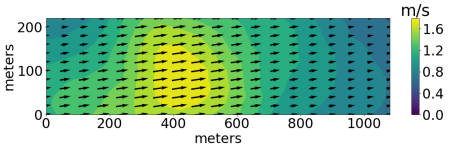

(b) Current data from SINMOD for 10:00.

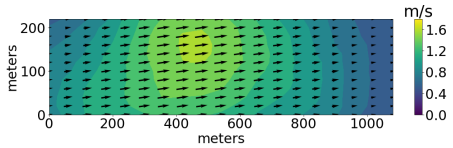

(c) Current data from SINMOD for 11:00.

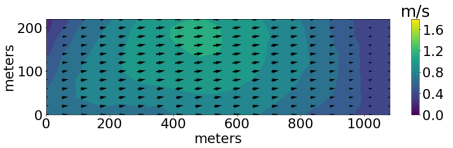

(d) Current data from SINMOD for 12:00.

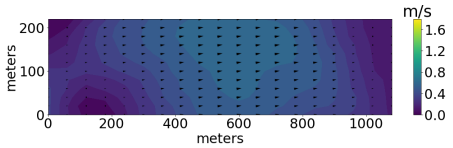

(e) Current data from SINMOD for 13:00.

Figure 10.9: Hourly ocean current predictions from SINMOD between 09:00 and 13.00. The currents are highly influenced by the tides showing an inward flow (eastward) before the tidal high (09:00-11:00) and weaker ocean currents during the tidal high (11:00-13:00).

Mission 1: 08:53 - 10:44

The first mission was conducted between 08:53 and 10:44 on December 17th, before a tidal high. The estimated current from the SINMOD model can be seen in Figures 10.9a, 10.9b, 10.9c. Figure 10.10 presents the onboard model results. The left column shows the updated mean of the onboard model, representing the mine tailings log(concentration) for selected time steps. The right column shows the onboard model standard deviation at selected time steps and the AUV path up until the given time. The red line represents the AUV path, and the red dots are the waypoints selected by our sampling strategy. The results show increased tailing concentration in the eastern area, especially at the beginning of the mission (see Figure 10.10a,10.10c and 10.10e). We observe a decay in the concentration in this area after 1.5 hours (see Figure 10.10g). This is when the ocean currents get weaker due to the tidal cycle. In the beginning, the chosen sampling strategy seems to focus on exploring the area, covering large parts of the whole rectangle. After the exploration, the focus switches to the eastern area, where high mine tailing concentrations have been observed.

Mission 2: 11:52 - 13:24

The second mission was conducted during a tidal high. Figure 10.11 shows results from this survey. The predicted SINMOD ocean currents are much weaker than for

mission 1 (see Figure 10.9d and 10.9e). Figure 10.11 presents the onboard model results. The left column shows the updated mean of the onboard model, and the right column shows the standard deviation together with the selected AUV path. This mission does not contain areas of clearly increased tailings concentration, and we see that the AUV chooses a different sampling strategy. Since no area shows increased concentration, there is no extra focus on any special area. Instead, the waypoints are chosen to cover as much as possible of the whole survey area during the whole mission.

10.2.3 Discussion

The chosen sampling paths (see second column of Figure 10.10 and 10.11) follow two different strategies. In the beginning, they are quite similar, focusing on exploring the area, but after the exploration, we see differences in waypoint selection. The sampling path in mission 1 (Figure 10.10) focuses on the eastern area where increased concentration is observed, while the sampling path in mission 2, where there are no areas with increased tailings concentration, continues to cover the whole region also after the initial exploration. For both surveys, the standard deviation is clearly reduced at the end of the mission, indicating that the method manages to explore the area. The selection of different strategies shows that the method is adaptive and will change depending on prior data and observations and that the sampling is focused on areas with high tailings concentration. The AUV data are undoubtedly useful for refining the DREAM results.

It is hard to rate the field experiments' performance since there is no ground truth for this case. Still, the model mean concentration (first column of Figure 10.10 and 10.11 coincide well with our assumptions on how the tailings concentration behave. Since the outlet is located on the east side of our area, we assume elevated concentration in the east. It is also reasonable to assume that the concentration of mine tailings in the survey area will be higher when the currents flow westward, as is the case for mission 1. We have also compared the results with data from the ocean model DREAM and have observed the same tendencies. However, this is not an accurate comparison since the proxy model is trained with data from this model.

Since there is no easy way to obtain a ground truth for field experiments, it is difficult to determine how well the method performs in the field. Still, our results agree well with our assumptions of the mine tailings distribution at the time, and the selection of different sampling strategies for two missions illustrates the method's adaptivity.

10.3 Excursion sets

We present results where the AUV was used in the field to detect ESs containing a high concentration of mine tailings particles. The experiment was carried out on September 17th, 2020. The operational discharge at the time of the experiments is marked as 2.4 in Figure 10.6, and an operational area on the west side of the outlet of size 1140 m $\times$ 240 m was used. The predicted drift field at 20 m depth at the

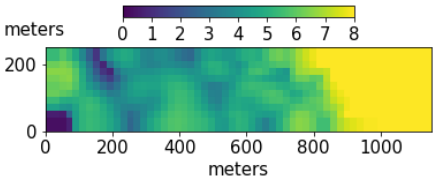

(a) Updated mean concentration at 09:00.

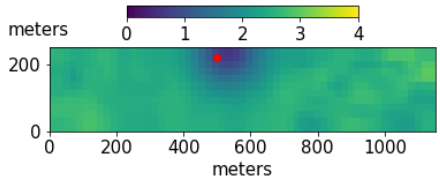

(b) Standard deviation at 09:00.

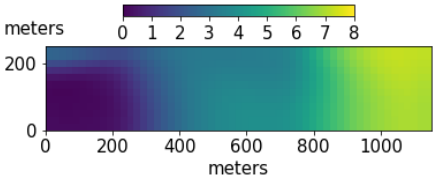

(c) Updated mean concentration at 09:30.

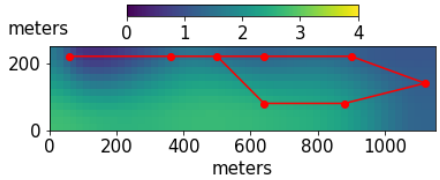

(d) Standard deviation at 09:30.

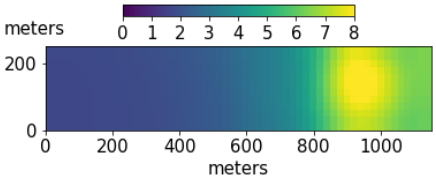

(e) Updated mean concentration at 10:00.

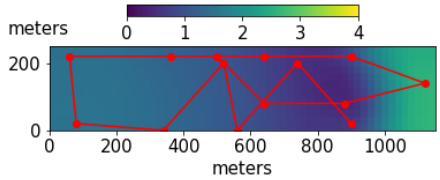

(f) Standard deviation at 10:00.

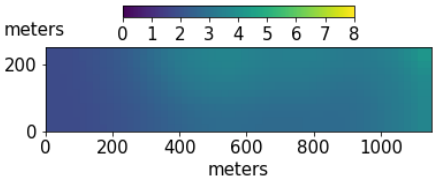

(g) Updated mean concentration at 10:44.

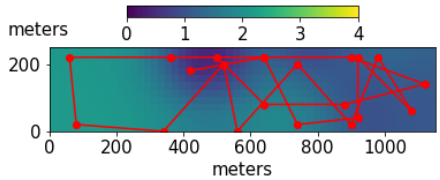

(h) Standard deviation at 10:44.

Figure 10.10: Results from mission 1. The left column shows the updated mean of the onboard model, representing the mine tailings log(concentration) for selected time steps. The right column shows the onboard model standard deviation at selected time steps and the AUV path up until the given time. The red line represents the AUV path, and the red dots are the waypoints selected by our sampling strategy.

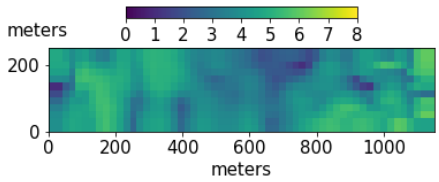

(a) Updated mean concentration at 12:00.

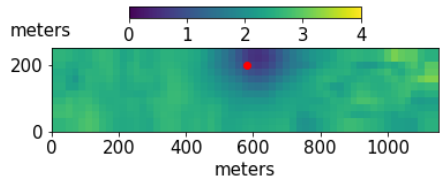

(b) Standard deviation at 12:00.

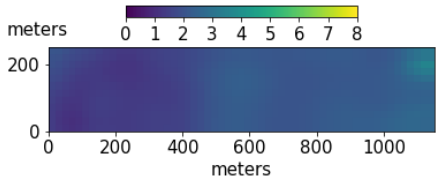

(c) Updated mean concentration at 12:45.

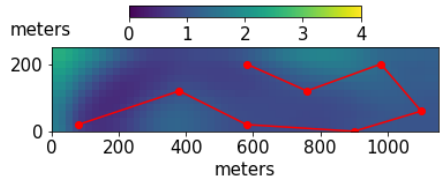

(d) Standard deviation at 12:45.

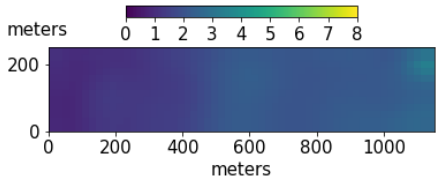

(e) Updated mean concentration at 13:20.

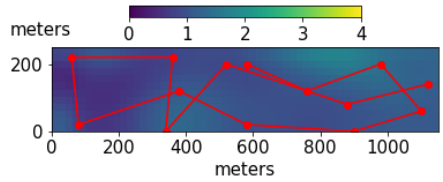

(f) Standard deviation at 13:20.

Figure 10.11: Results from mission 2. The left column shows the updated mean of the onboard model, representing the mine tailings log(concentration) for selected time steps. The right column shows the onboard model standard deviation at selected time steps and the AUV path up until the given time. The red line represents the AUV path, and the red dots are the waypoints selected by our sampling strategy.

time of the experiment is shown in Figure 10.12 (from SINMOD). As seen in the display, the currents mainly flowed outwards of the fjord (towards the south-west) at the time.

10.3.1 Experimental setup

The size 57×12 regular 2-dimensional grid inside the operational area means that $N = 684$. The distance between each node was approximately 20 m in both grid directions. In order to reduce risk and avoid too much vehicle drift, the AUV was set to move in a yoyo motion between the surface and the target near 20 m depth. By doing so, the distance between each new chosen neighboring waypoint was between 270 m and 290 m, and considering the AUV speed (about 1.2 m/s), the travel time between each waypoint was around 4 minutes.

The SPDE parameters in the field experiments were specified as explained in

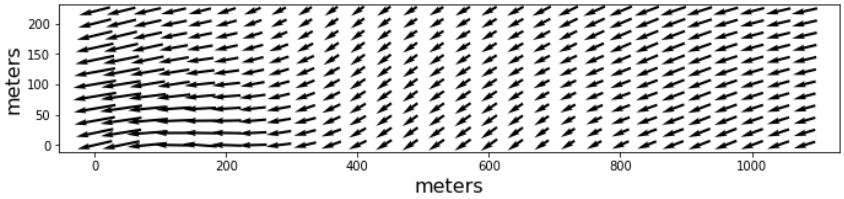

Figure 10.12: The drift field at 30 meters depth used in the field experiments. The currents flow towards the south-west (out of the fjord).

Chapter 5 using predictions from DREAM and SINMOD for the time of the mission.

10.3.2 Results

We used the {SPDE: EMMP_{t_n}} strategy to choose the next waypoint in the field experiments. This strategy was run for a total of $t_n = 12$ time steps, and a critical limit $l = 4.5$ log(ppb) was used. Figure 10.13 summarizes the mine tailings concentration distribution at selected time steps of this procedure. The displays indicate updated mean (left), standard deviation (right), and EPs (middle). The resulting AUV path is plotted as a red line and the waypoints as dots.

Since there exists no ground truth for this case, the evaluation of the results is complex. Still, we can see that the method behaves as we expect. At the beginning of the mission, the AUV traverses from the west to the east side close to the outlet. Then it heads back west and focuses on the area of the predicted boundary of the ES. Comparing the standard deviations at the beginning of the mission with the standard deviations at the end of the mission, we see that the uncertainty in the model is clearly reduced. The results are clearly refined from that of SINMOD and DREAM data alone (top) when AUV data are assimilated into the model (bottom rows). Also, the EPs show that the mine tailings concentrations tend to move further to the left in the lower part of the grid. This appears natural from the physics induced by the advection field in Figure 10.12 but is far from apparent based on the initial model (top).

Figure 10.14 shows the EMMP_t over all the grid nodes at each time step. The EMMP_t decreases over time, indicating that our method chooses informative waypoints. The exception is at time $t = 4$, where there is a slight increase. By taking a closer look at the data, this occurs because of a surprisingly small concentration (4.21 log(ppb)) in a location quite close to the source (lower, right corner in Figure 10.13d). Since the model expected a higher concentration at this location, and because the in-situ value is quite close to the critical limit $l = 4.5$ log(ppb), the update at $t = 4$ led to an increase in the EMMP.

In field results, the adaptive sampling procedure gives reasonable results in the sense that the vehicle focuses on the expected boundary regions of high and low concentration, and at the end of the operation, the excursion probabilities are close to 0 or 1. The results further indicate that the excursion sets obtained from the autonomous surveying can be interpreted from the physical conditions of the ocean

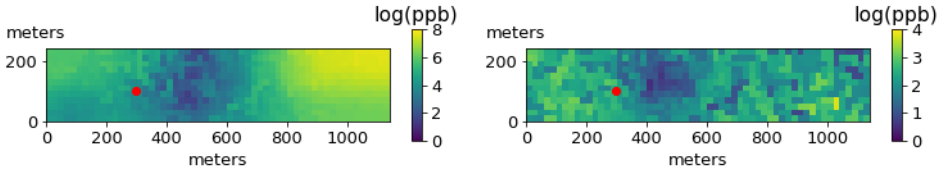

(a) Updated mean $\boldsymbol{\mu}_1$.

(b) Standard deviation $\boldsymbol{\sigma}_1$.

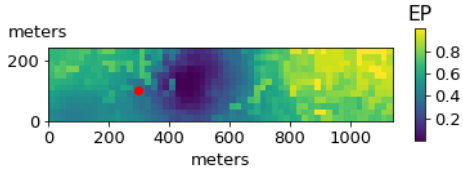

(c) Excursion probability EP_1.

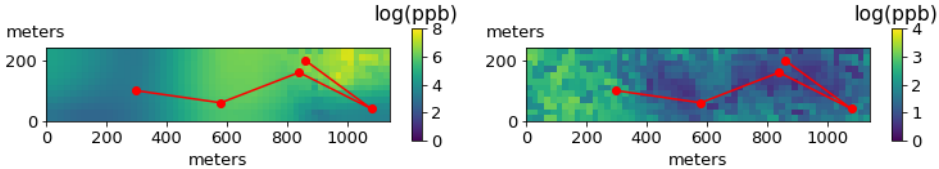

(d) Updated mean $\boldsymbol{\mu}_5$.

(e) Standard deviation $\boldsymbol{\sigma}_5$.

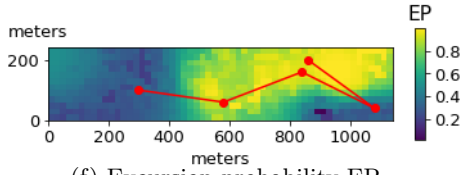

(f) Excursion probability EP_5.

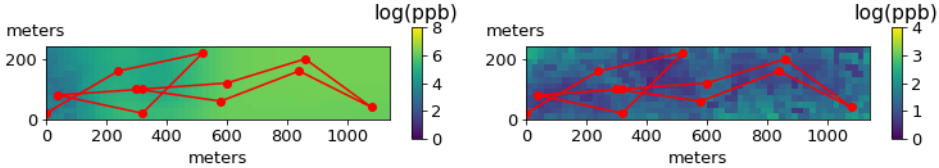

(g) Updated mean $\boldsymbol{\mu}_{12}$.

(h) Standard deviation $\boldsymbol{\sigma}_{12}$.

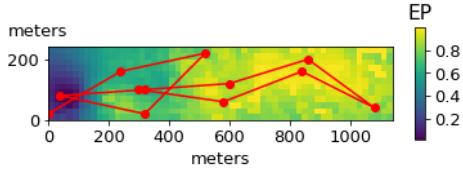

(i) Excursion probability EP_{12}.

Figure 10.13: Predicted state at selected time steps. The selected waypoints are plotted as a red dot, and the red line shows the AUV path up until the given time.

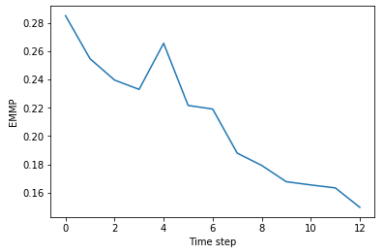

Figure 10.14: EMMP_t computed at each time step t of the operation. The EMMP_t decreases over time, indicating that our method chooses informative waypoints. An exception can be seen at time $t = 4$, where there is a slight increase.

currents and the mining deposit site, and more so than from the ocean model data alone.

10.4 Closing remarks

There is currently an enormous development in sensor technologies and autonomous robotic systems that can deploy these new tools in harsh environments such as the oceans. Their use can benefit from realistic statistical modeling and design methods, for instance, in the context of where and when to sample an environmental phenomenon, as we demonstrate in this work. The field experiments work as a proof-of-concept; we show that the suggested models are able to run onboard an AUV with limited computing resources and the AUV is able to select waypoints based on onboard computations using the framework described in Chapter 9.

Exploring the accuracy of the field estimation is hard due to the difficulty of obtaining a ground truth. However, the results coincide well with our assumptions on how the tailings concentration behave in the area. Comparison with the particle transport model DREAM also show the same tendencies.

Part IV

Conclusion

Chapter 11

Conclusion and future work

In this thesis, methods for adaptive sampling with AUVs in coastal regions have been explored. Chapter 2 presents numerical ocean models. Data from these models are used to create an onboard spatio-temporal GP model expressing the state of a 2-dimensional particle concentration field. The spatio-temporal model are presented in chapters 3 and 4, and chapter 5 shows how the parameters of the onboard model are specified from the ocean model data. An objective function for waypoint selecting is described in chapter 6. The performance of adaptive approaches using this function is tested in simulation studies and compared to simpler strategies, and the studies show that the adaptive approach performs better than the simpler approach (e.g., lawnmower surveys). It is also seen that the sampling strategy behaves in desired ways as it reduces model variance and explores hotspots efficiently. In chapter 7, another sampling strategy based on reducing the mis-classification probabilities of the excursions sets of high and low concentration levels was explored. Simulation results show that a hybrid strategy using a myopic approach combined with a random detour is performing better than naive strategies. Also, the careful spatio-temporal modeling provides more accurate results than simpler spatial or autoregressive models. The inclusion of multiple vehicles is explored in chapter 8, where the survey area is partitioned and shared between the vehicles using weighted Voronoi diagrams. Adaptive sampling is executed in each region using the previously suggested objective function-strategy. It is shown that an area can be more efficiently explored using multiple vehicles, as the estimation error decreases with the number of added vehicles. Finally, results from field experiments are shown in chapter 10. Although there is no ground truth, the results show expected behavior and can serve as a proof-of-concept of the suggested sampling methods.

Now, the research questions from the introduction (Chapter 1) are highlighted and based on the presented work, answers to these questions are given.

Research questions and answers

- **How can prior information be utilized?** Prior information from numerical ocean models has been incorporated into an onboard model through the specification of parameters in a spatio-temporal GP model. Spatial dependencies are expressed through the GP kernel (correlation function), and knowledge of ocean currents and diffusion of particles are incorporated in a SPDE process model.
- **How can we create an ocean dynamics model that is computationally efficient, easy to update, and able to run onboard an AUV?** The onboard spatio-temporal GP model can efficiently be used for adaptive sampling. This is shown both through extensive simulation studies and during multiple field experiments.
- **What is the optimal way of taking samples using one or multiple AUVs?** Two sampling strategies are presented in this thesis. The objective function has proven to be useful, and the balance between exploration and exploitation can easily be adjusted by choosing different weightings in the function. This way of selecting waypoints is efficient for field estimation. Another approach for estimation of excursion sets has also been explored.

11.1 Future research directions

In this thesis, methods for underwater adaptive sampling with an AUV are discussed. This section mentions future directions for research where some of the directions are follow-ups on the current research and others are side-steps not investigated due to the limited scope of the thesis. The future directions are listed below:

- **Sparse GP techniques:** AUVs have limited computer powers, and as discussed in chapter 3, expanding the size of the estimated field greatly increases the computer resources needed. Sparse GP techniques could possibly reduce the computational time in such cases and should be further investigated.
- **Multi-robot field testing:** The field experiments are only run for a single AUV, and the multiple robot approach is only tested in simulation. Validating the simulation results in the field would be interesting. We have tried to adhere to constraints of fielded systems, for example, in the use of acoustic communication range and throughput, to provide confidence that these systems can be put to use in the field without needing significant modifications.
- **Localization uncertainty:** Underwater vehicles accumulate localization uncertainty when traveling underwater. This is especially observed when the AUV operates without bottom-track. In this thesis, an assumption has been made that localization accuracy is suitable for this work. In addition, the AUV is set to surface relatively often to avoid too much drifting errors. Future work should, however, consider the localization uncertainty in the adaptive sampling approaches.

- **Onboard current measurement:** In the spatio-temporal model, current data from the ocean model SINMOD is used to model the advection field, but as stated, there are uncertainties in the ocean model data. With improved technology and sensors, in-situ current measurements can be used to determine ocean currents.
- **Expanding to 3D:** Further work includes three-dimensional modeling, which would extend the current work only by looking at 20 m depth. This is, of course, more demanding from a computational viewpoint, but it would make the data assimilation much more realistic and avoid two-dimensional projection approximations in the AUV waypoint planning.
- **Uncertainty in the advection field:** It would also be interesting to include uncertainty in the advection field. A full-fledged stochastic model for this current field would likely not be possible to embed on the onboard computing resources, but a mixture SPDE model over a few scenarios of current fields might work.

References

[1] J. M. Angulo and A. E. Madrid. Structural analysis of spatio-temporal threshold exceedances. *Environmetrics*, 21:415–438, 2010.

[2] J. F. Artiola, M. L. Brusseau, and I. L. Pepper. *Environmental monitoring and characterization*. Academic Press, 2004.

[3] B. Bayat, N. Crasta, A. Crespi, A. Pascoal, and A. Ijspeert. Environmental monitoring using autonomous vehicles: a survey of recent searching techniques. *Current Opinion in Biotechnology*, 45:76–84, 06 2017. doi: 10.1016/j.copbio.2017.01.009.

[4] G. E. Berget, T. Fossum, T. A. Johansen, J. Eidsvik, and K. Rajan. Adaptive sampling of ocean processes using an AUV with a Gaussian proxy model. *IFAC-PapersOnLine*, 51:238–243, 01 2018. doi: 10.1016/j.ifacol.2018.09.509.

[5] G. E. Berget, J. Eidsvik, M. Alver, F. Py, E. I. Grøtli, and T. A. Johansen. Adaptive underwater robotic sampling of dispersal dynamics in the coastal ocean. *Proceedings of the International Symposium on Robotics Research*, accepted, 2019.

[6] D. Bhattacharjya, J. Eidsvik, and T. Mukerji. The value of information in portfolio problems with dependent projects. *Decision Analysis*, 10(4):341–351, 2013.

[7] D. Bolin and F. Lindgren. Excursion and contour uncertainty regions for latent Gaussian models. *Journal of the Royal Statistical Society: Series B*, 77 (1):85–106, 2015.

[8] D. Bolin and F. Lindgren. Calculating probabilistic excursion sets and related quantities using excursions. *Journal of Statistical Software*, 86(5):1–20, 2018.

[9] G. H. Born, J. A. Dunne, and D. B. Lame. Seasat mission overview. *Science*, 204(4400):1405–1406, 1979. doi: 10.1126/science.204.4400.1405. URL https://www.science.org/doi/abs/10.1126/science.204.4400.1405.

[10] G. Box. Robustness in the strategy of scientific model building. In R. L. Launer and G. N. Wilkinson, editors, *Robustness in Statistics*, pages 201–236. Academic Press, 1979. ISBN 978-0-12-438150-6. doi: https://doi.org/10.1016/B978-0-12-438150-6.50018-2. URL https://www.sciencedirect.com/science/article/pii/B9780124381506500182.

[11] C. Chevalier, J. Bect, D. Ginsbourger, E. Vazquez, V. Picheny, and Y. Richet. Fast parallel kriging-based stepwise uncertainty reduction with application to the identification of an excursion set. *Technometrics*, 56(4):455–465, 2013.

[12] N. Cressie and C. Wikle. *Statistics for Spatio-Temporal Data*. CourseSmart Series. Wiley, 2011. ISBN 9780471692744.

[13] J. Das, F. Py, J. B. Harvey, J. P. Ryan, A. Gellene, R. Graham, D. A. Caron, K. Rajan, and G. S. Sukhatme. Data-driven robotic sampling for marine ecosystem monitoring. *The International Journal of Robotics Research*, 34 (12):1435–1452, 2015. doi: 10.1177/0278364915587723.

[14] R. A. Davis. Gaussian process. *Encyclopedia of Environmetrics*, 2006.

[15] D. Dee, S. M. Uppala, A. J. Simmons, P. Berrisford, P. Poli, S. Kobayashi, U. Andrae, M. Balmaseda, G. Balsamo, P. Bauer, P. Bechtold, A. Beljaars, L. van de Berg, J. Bidlot, N. Bormann, C. Delsol, R. Dragani, M. Fuentes, and F. Vitart. The ERA-Interim reanalysis: Configuration and performance of the data assimilation system. *Quarterly Journal of the Royal Meteorological Society*, 137:553–597, 04 2011. doi: 10.1002/qj.828.

[16] A. Dutta, A. Bhattacharya, O. Kreidl, A. Ghosh, and R. Dasgupta. Multi-robot informative path planning in unknown environments through continuous region partitioning. *International Journal of Advanced Robotic Systems*, pages 1–18, 11 2020. doi: 10.1177/1729881420970461.

[17] J. Eidsvik, T. Mukerji, and D. Bhattacharjya. *Value of information in the earth sciences : integrating spatial modeling and decision analysis*. Cambridge University Press, Cambridge, 2015. ISBN 9781107040267.

[18] K. Foss, G. Berget, and J. Eidsvik. Using an autonomous underwater vehicle with onboard stochastic advection-diffusion models to map excursion sets of environmental variables. *Environmetrics*, e2702, 08 2021. doi: 10.1002/env.2702.

[19] K. H. Foss. Spatio-temporal Gaussian processes and excursion sets for adaptive environmental sensing using underwater robotics. Master's thesis, NTNU, 2019.

[20] T. Fossum, J. Eidsvik, I. Ellingsen, M. Alver, G. Fragoso, G. Johnsen, R. Mendes, M. Ludvigsen, and K. Rajan. Information-driven robotic sampling in the coastal ocean. *Journal of Field Robotics*, 35:1101–1121, 07 2018. doi: 10.1002/rob.21805.

[21] T. O. Fossum. *Adaptive Sampling for Marine Robotics*. PhD thesis, Norwegian University of Science and Technology, 2019.

[22] T. O. Fossum, C. Travelletti, J. Eidsvik, D. Ginsbourger, and K. Rajan. Learning excursion sets of vector-valued Gaussian random fields for autonomous ocean sampling. *Annals of Applied Statistics*, 2021.

[23] B. Fox-Kemper, A. Adcroft, C. Böning, E. Chassignet, E. Curchitser, G. Danabasoglu, C. Eden, M. England, R. Gerdes, R. Greatbatch, S. Griffies, R. Hallberg, E. Hanert, P. Heimbach, H. Hewitt, C. Hill, Y. Komuro, S. Legg, J. Sommer, and S. Yeager. Challenges and prospects in ocean circulation models. *Frontiers in Marine Science*, 6, 02 2019. doi: 10.3389/fmars.2019.00065.

[24] J. P. French and S. R. Sain. Spatio-temporal exceedance locations and confidence regions. *The Annals of Applied Probability*, 7(3):1421–1449, 2013.

[25] R. B. Gramacy. *Surrogates: Gaussian process modeling, design, and optimization for the applied sciences*. Chapman and Hall/CRC, 2020.

[26] S. M. Griffies, C. Böning, F. O. Bryan, E. P. Chassignet, R. Gerdes, H. Hasumi, A. Hirst, A.-M. Treguier, and D. Webb. Developments in ocean climate modelling. *Ocean Modelling*, 2:123–192, 2000. doi: 10.1016/S1463-5003(00)00014-7.

[27] C. Guestrin, A. Krause, and A. Singh. Near-optimal sensor placements in Gaussian processes. pages 265–272, 01 2005. doi: 10.1145/1102351.1102385.

[28] O. K. Hagen, K. B. Ånonsen, and T. O. Sæbø. Toward autonomous mapping with AUVs-line-to-line terrain navigation. In *OCEANS 2015 - MTS/IEEE Washington*, pages 1–8, 2015. doi: 10.23919/OCEANS.2015.7404387.

[29] K. Heaney, G. Gawarkiewicz, T. Duda, and P. Lermusiaux. Nonlinear optimization of autonomous undersea vehicle sampling strategies for oceanographic data-assimilation. *Journal of Field Robotics*, 24:437–448, 06 2007. doi: 10.1002/rob.20183.

[30] P. Holgate. Lognormal distributions: Theory and applications. *Journal of The Royal Statistical Society Series A-statistics in Society*, 152:256–256, 1989.

[31] J. W. Hyun, Y. Li, C. Huang, M. Styner, W. Lin, and H. Zhu. Stgp: Spatio-temporal Gaussian process models for longitudinal neuroimaging data. *NeuroImage*, 134:550 – 562, 2016. ISSN 1053-8119. doi: https://doi.org/10.1016/j.neuroimage.2016.04.023. URL http://www.sciencedirect.com/science/article/pii/S105381191630057X.

[32] C. Jennison and B. W. Turnbull. *Group sequential methods with applications to clinical trials*. CRC Press, 1999.

[33] M. Jun and M. L. Stein. Nonstationary covariance models for global data. *The Annals of Applied Statistics*, 2(4):1271–1289, 2008.

[34] S. Kemna, D. A. Caron, and G. S. Sukhatme. Adaptive informative sampling with autonomous underwater vehicles: Acoustic versus surface communications. In *OCEANS 2016 MTS/IEEE Monterey*, pages 1–8, 2016. doi: 10.1109/OCEANS.2016.7761128.

[35] S. Kemna, J. G. Rogers, C. Nieto-Granda, S. Young, and G. S. Sukhatme. Multi-robot coordination through dynamic Voronoi partitioning for informative adaptive sampling in communication-constrained environments. In *2017 IEEE International Conference on Robotics and Automation (ICRA)*, pages 2124–2130, 2017. doi: 10.1109/ICRA.2017.7989245.

[36] A. Khoshrou, A. P. Aguiar, and F. Pereira. Adaptive sampling using an unsupervised learning of GMMs applied to a fleet of AUVs with CTD measurements. In *Robot 2015: Second Iberian Robotics Conference; Germany*, pages 321–332, 2016. ISBN 978-3-319-27145-3. doi: 10.1007/978-3-319-27146-0_25.

[37] A. Krause, C. Guestrin, A. Gupta, and J. Kleinberg. Near-optimal sensor placements: Maximizing information while minimizing communication cost. volume 2006, pages 2–10, 01 2006. doi: 10.1109/IPSN.2006.244031.

[38] A. Krause, A. Singh, and C. Guestrin. Near-optimal sensor placements in Gaussian processes: Theory, efficient algorithms and empirical studies. *J. Mach. Learn. Res.*, 9:235–284, June 2008. ISSN 1532-4435.

[39] A. Kvassnes and E. Iversen. Waste sites from mines in norwegian fjords. *Mineralproduksjon.*, 3:A27–A38, 01 2013.

[40] F. Lindgren, H. Rue, and J. Lindström. An explicit link between Gaussian fields and Gaussian Markov random fields: the stochastic partial differential equation approach. *Journal of the Royal Statistical Society: Series B (Statistical Methodology)*, 73(4):423–498, 2011.

[41] G. M. Lovett, D. A. Burns, C. T. Driscoll, J. C. Jenkins, M. J. Mitchell, L. Rustad, J. B. Shanley, G. E. Likens, and R. Haeuber. Who needs environmental monitoring? *Frontiers in Ecology and the Environment*, 5(5):253–260, 2007.

[42] K. H. Low, J. Dolan, and P. Khosla. Adaptive multirobot wide-area exploration and mapping. volume 1, pages 23–30, 01 2008. doi: 10.1145/1402383.1402392.

[43] W. Luo and K. Sycara. Adaptive sampling and online learning in multi-robot sensor coverage with mixture of Gaussian processes. In *2018 IEEE International Conference on Robotics and Automation (ICRA)*, pages 6359–6364, May 2018. doi: 10.1109/ICRA.2018.8460473.

[44] P. Lågstad, P. E. Hagen, and P. Kartvedt. The HUGIN AUV in international military operations. *UDT Europe 2004*, 06 2004.

[45] K.-C. Ma, L. Liu, H. Heidarsson, and G. Sukhatme. Data-driven learning and planning for environmental sampling. *Journal of Field Robotics*, 35(5):643–661, 02 2018. doi: 10.1002/rob.21767.

[46] J. Martin, J. Wang, and B. Englot. Sparse Gaussian process temporal difference learning for marine robot navigation. In A. Billard, A. Dragan, J. Peters,

and J. Morimoto, editors, *Proceedings of The 2nd Conference on Robot Learning*, volume 87 of *Proceedings of Machine Learning Research*, pages 179–189. PMLR, 29–31 Oct 2018. URL https://proceedings.mlr.press/v87/martin18a.html.

[47] B. Matérn. Spatial variation. *Meddelanden från Statens Skogsforskningsinstitut*, 36(5):1–144, 2013.

[48] G. Matheron. Principles of geostatistics. *Economic Geology*, 58(8):1246–1266, 12 1963. ISSN 0361-0128. doi: 10.2113/gsecongeo.58.8.1246. URL https://doi.org/10.2113/gsecongeo.58.8.1246.

[49] T. Mo-Bjørkelund, P. Norgren, and M. Ludvigsen. Simulation and forecasting of ice drift as a tool for autonomous under ice operations. In *2020 IEEE/OES Autonomous Underwater Vehicles Symposium (AUV)*, pages 1–6, 2020. doi: 10.1109/AUV50043.2020.9267921.

[50] E. Morello, M. Haywood, D. Brewer, S. Apte, G. Asmund, Y. Kwong, and D. Dennis. *The Ecological Impacts of Submarine Tailings Placement*, pages 315–366. 12 2016. ISBN 978-1-4987-4798-1. doi: 10.1201/9781315368597-7.

[51] W. Munk. The evolution of physical oceanography in the last hundred years. *Oceanography*, 15, 01 2002. doi: 10.5670/oceanog.2002.45.

[52] M. Mysorewala, L. Cheded, and D. Popa. A distributed multi-robot adaptive sampling scheme for the estimation of the spatial distribution in widespread fields. *EURASIP Journal on Wireless Communications and Networking*, 2012: 223, 07 2012. doi: 10.1186/1687-1499-2012-223.

[53] F. Nansen. *Farthest North, Volumes I and II.* London: Archibald Constable Co., 1897.

[54] R. Nepstad, M. Liste, M. O. Alver, T. Nordam, E. Davies, and T. Glette. High-resolution numerical modelling of a marine mine tailings discharge in western norway. *Regional Studies in Marine Science*, 39:101404, 2020. ISSN 2352-4855. doi: https://doi.org/10.1016/j.rsma.2020.101404.

[55] H. Niu, S. Adams, K. Lee, T. Husain, and N. Bose. Applications of autonomous underwater vehicles in offshore petroleum industry environmental effects monitoring. volume 48, pages 12–16, 06 2007. doi: 10.2118/2007-116.

[56] NOAA. How much of the ocean have we explored? https://oceanservice.noaa.gov/facts/exploration.html. 2021-02-26.

[57] S. I. of Oceanography. NORPAC hydrographic data report of the Scripps Institution of Oceanography, University of California, and the South Pacific Fishery Investigations, U. S. fish and wildlife service, for the NORPAC cruise of august-september 1955. *University of California*, 1956.

[58] A. Pereira, J. Binney, G. Hollinger, and G. Sukhatme. Risk-aware path planning for autonomous underwater vehicles using predictive ocean models. *Journal of Field Robotics*, 30(5):741–762, 09 2013. doi: 10.1002/rob.21472.

[59] S. Petillo and H. Schmidt. Exploiting adaptive and collaborative AUV autonomy for detection and characterization of internal waves. *IEEE Journal of Oceanic Engineering*, 39(1):150–164, 2014. doi: 10.1109/JOE.2013.2243251.

[60] J. Pinto, P. Calado, J. Braga, P. Dias, R. Martins, E. Marques, and J. Sousa. Implementation of a control architecture for networked vehicle systems. *IFAC Proceedings Volumes*, 45(5):100–105, 2012.

[61] J. Pinto, P. Dias, R. Martins, J. Fortuna, E. Marques, and J. Sousa. The LSTS toolchain for networked vehicle systems. In *OCEANS 2013 MTS/IEEE Bergen: The Challenges of the Northern Dimension*, 06 2013. doi: 10.1109/OCEANS-Bergen.2013.6608148.

[62] S. V. Prants, M. Y. Uleysky, and M. V. Budyansky. *Lagrangian oceanography: large-scale transport and mixing in the ocean.* Springer, 2017.

[63] R Core Team. *R: A Language and Environment for Statistical Computing.* R Foundation for Statistical Computing, Vienna, Austria, 2017. URL https://www.R-project.org/.

[64] K. Rajan and F. Py. T-REX: partitioned inference for AUV mission control. *Further advances in unmanned marine vehicles*, pages 171–199, 2012.

[65] E. Ramirez-Llodra, H. Trannum, A. Evenset, L. Levin, M. Andersson, T. Finne, A. Hilário, B. Flem, G. Christensen, M. Schaanning, and A. Vanreusel. Submarine and deep-sea mine tailing placements: A review of current practices, environmental issues, natural analogs and knowledge gaps in Norway and internationally. *Marine Pollution Bulletin*, 97, 06 2015. doi: 10.1016/j.marpolbul.2015.05.062.

[66] C. E. Rasmussen and C. K. I. Williams. *Gaussian Processes for Machine Learning (Adaptive Computation and Machine Learning).* The MIT Press, 2005. ISBN 026218253X.

[67] T. Rice. The "challenger" expedition: the end of an era or a new beginning? In M. Deacon, T. Rice, and C. Summerhayes, editors, *Understanding the oceans: a century of ocean exploration.*, pages 27–48. London, Uk, UCL Presss, 2001.

[68] R. A. Richardson. Sparsity in nonlinear dynamic spatiotemporal models using implied advection. *Environmetrics*, 28(6):e2456, 2017.

[69] H. Rye, M. Reed, and N. Ekrol. The partrack model for calculation of the spreading and deposition of drilling mud, chemicals and drill cuttings. *Environmental Modelling Software*, 13(5):431 – 441, 1998. ISSN 1364-8152. doi: https://doi.org/10.1016/S1364-8152(98)00048-6.

[70] H. Rye, M. Reed, T. Frost, M. Smit, I. Durgut, O. Johansen, and M. Ditlevsen. Development of a numerical model for calculating exposure to toxic and non-toxic stressors in the water column and sediment from drilling discharges. *Integrated environmental assessment and management*, 4:194–203, 05 2008.

[71] M. Schwager, M. P. Vitus, S. Powers, D. Rus, and C. J. Tomlin. Robust adaptive coverage control for robotic sensor networks. *IEEE Transactions on Control of Network Systems*, 4(3):462–476, 2017. doi: 10.1109/TCNS.2015.2512326.

[72] R. Service. Rock chemistry traces ancient traders. *Science*, 274(5295):2012–2013, 1996.

[73] F. Sigrist, H. Künsch, and W. Stahel. Stochastic partial differential equation based modeling of large space-time data sets. *Journal of the Royal Statistical Society: Series B (Statistical Methodology)*, 77:3–33, 1 2015. doi: 10.1111/rssb.12061.

[74] D. Slagstad and T. McClimans. Modeling the ecosystem dynamics of the Barents Sea including the marginal ice zone: I. Physical and chemical oceanography. 58:1–18, 10 2005.

[75] M. Sommerfeld, S. Sain, and A. Schwartzman. Confidence regions for spatial excursion sets from repeated random field observations, with an application to climate. *Journal of the American Statistical Association*, 113(523):1327–1340, 2018.

[76] R. H. Stewart. *Introduction To Physical Oceanography*. Texas A & M University, 01 2008. ISBN 0132381559. doi: 10.1119/1.18716.

[77] L. Tartar. *An introduction to Navier-Stokes equation and oceanography*, volume 1. Springer, 2006.

[78] W. R. Tobler. A computer movie simulating urban growth in the detroit region. *Economic Geography*, 46:234–240, 1970. ISSN 00130095, 19448287. URL http://www.jstor.org/stable/143141.

[79] R. van der Merwe, T. K. Leen, Z. Lu, S. Frolov, and A. M. Baptista. Fast neural network surrogates for very high dimensional physics-based models in computational oceanography. *Neural Networks*, 20(4):462–478, 2007. ISSN 0893-6080. doi: https://doi.org/10.1016/j.neunet.2007.04.023. URL https://www.sciencedirect.com/science/article/pii/S0893608007000494. Computational Intelligence in Earth and Environmental Sciences.

[80] J. Vanhatalo, V. Pietiläinen, and A. Vehtari. Approximate inference for disease mapping with sparse Gaussian processes. *Statistics in medicine*, 29:1580–607, 07 2010. doi: 10.1002/sim.3895.

[81] G. Voronoi. Nouvelles applications des paramètres continus à la théorie des formes quadratiques. deuxième mémoire. recherches sur les parallélloèdres primitifs. *Journal für die reine und angewandte Mathematik (Crelles Journal)*, 1908(134):198–287, 1908. doi: doi:10.1515/crll.1908.134.198. URL https://doi.org/10.1515/crll.1908.134.198.

[82] H. Widditsch. SPURV-The First Decade. Technical report., 1973.

[83] N. K. Yilmaz, C. Evangelinos, P. F. J. Lermusiaux, and N. M. Patrikalakis. Path planning of autonomous underwater vehicles for adaptive sampling using mixed integer linear programming. *IEEE Journal of Oceanic Engineering*, 33 (4):522–537, Oct 2008. ISSN 0364-9059. doi: 10.1109/JOE.2008.2002105.

[84] Y. Zhang, M. A. Godin, J. G. Bellingham, and J. P. Ryan. Using an autonomous underwater vehicle to track a coastal upwelling front. *IEEE Journal of Oceanic Engineering*, 37(3):338–347, July 2012. ISSN 0364-9059. doi: 10.1109/JOE.2012.2197272.